Sapphire Fiber-based Distributed High-temperature Sensing System

Bo Liu

Dissertation submitted to the Faculty of
Virginia Polytechnic Institute and State University
In partial fulfillment of the requirements for the degree of

Doctor of Philosophy
in
Electrical Engineering

Anbo Wang, Chairman
Gary Pickrell
Ting Chung Poon
Yong Xu
Yizheng Zhu

August 30th, 2016
Blacksburg, Virginia

Keywords: fiber-optic sensor, temperature sensor, Raman scattering, distributed temperature sensing, sapphire fiber

ABSTRACT

Dissertation title: Sapphire Fiber-based Distributed High-temperature Sensing System

Bo Liu

From the monitoring of deep ocean conditions to the imaging and exploration of the vast universe, optical sensors are playing a unique, critical role in all areas of scientific research. Optical fiber sensors, in particular, are not only widely used in daily life such as for medical inspection, structural health monitoring, and environmental surveillance, but also in high-tech, high-security applications such as missile guidance or monitoring of aircraft engines and structures. Measurements of physical parameters are required in harsh environments including high pressure, high temperature, highly electromagnetically-active and corrosive conditions. A typical example is fossil fuel-based power plants. Unfortunately, current optical fiber sensors for high-temperature monitoring can work only for single point measurement, as traditional fully-distributed temperature sensing techniques are restricted for temperatures below 800ºC due to the limitation of the fragile character of silica fiber under high temperature.

In this research, a first-of-its-kind technology was developed which pushed the limits of fully distributed temperature sensing (DTS) in harsh environments by exploring the feasibility of DTS in optical sapphire waveguides. An all sapphire fiber-based Raman DTS system was demonstrated in a 3-meters long sapphire fiber up to a temperature of 1400ºC with a spatial resolution of 16.4cm and a standard deviation of a few degrees Celsius.

In this dissertation, the design, fabrication, and testing of the sapphire fiber-based Raman DTS system are discussed in detail. The plan and direction for future work are also suggested with an aim for commercialization.

Abstract for a General Audience

Bo Liu

(bol@vt.edu)

Electrical and Computer Engineering, Blacksburg VA 24061, USA

August 30, 2016

This project studied the temperature dependence of Raman scattering characteristics in the single-crystal sapphire fiber. Based on these results, we designed and implemented a sapphire fiber-based fully distributed temperature sensing system using a high-power pulsed-laser. Our preliminary results show excellent and consistent temperature resolution from room temperature up to 1400 ºC. To our best knowledge, this is the first demonstration of a sapphire fiber-based distributed temperature sensing of any kind. These sensors are suitable for coal gasifiers in which the environment is corrosive, for aerospace engines and turbines requiring compact sensing elements and boilers with high-pressure environments.

ACKNOWLEDGEMENTS

First and foremost, I would like to deeply thank Dr. Anbo Wang for providing me the opportunity to engage my Ph.D. study and the top research in the world. Dr. Anbo Wang, the first rate scientist and academic expert, is usually the first arriving the lab in the morning, always aims to attain the first place in scientific research and devotion in actual applications. He has had and will continue to have a great influence on my career and personal life as an excellent role model through his strict attitude, profound knowledge, productive thought, and charming personality. This entire research could not be accomplished without his constant support, wonderful tutelage, illuminating discussion, and encouragement. I would like to express my sincere appreciation to him for all his mentoring, and trust.

It is a great fortune and honor to have my second mentor, Dr. Yong Xu, whose strong theory foundation attracts and inspires me. His step-by-step guidance on my research is one I shall never forget. He provides each student sufficient freedom to pursue their own interests and new directions. I would not forget the first day I arrived in Blacksburg and met Dr. Gary Pickrell in Evan Lally's celebration. His warm smile always reminds me of the attitude of life. I would like to thank Dr. Gary Pickrell for offering me a career-changing opportunity, and also for his great leadership, excellent insights and general supervision in my project. I am also grateful to my committee members Dr. Ting-Chung Poon and Dr. Yizheng Zhu for their unreserved help on the course study and research.

Sincerely thanks are due to my managers: firstly, Dr. Daniel Homa, whose consistent encouragement saved me from depression and inspired me to success, and whose suggestions for my academic research and personal life has been proven invaluable. Many thanks to Dr. Bo Dong for his hand-in-hand teaching and assistance which built practical engineering skills and confidence and was proven invaluable again. And last, but not least, Dr. Zhihao Yu and Dr. James Gong, whose demonstration of excellent leadership in my project are greatly appreciated.

It has been a greatly pleasant and valuable experience to work with elites at Virginia Tech. Dr. Cheng Ma is the one I admire the most and will stand as an example to strive for. I would like to thank my best friends, Zhipeng tian, Dr. Dorothy Wang, Di Hu, Li Yu, Dr. Peng Lu, and Chaofan Wang for their cherished friendship. I am sincerely grateful to my dearest friends, Dr. Phuong Bui,

Cari Ulfers for their understanding and making my life colorful. In particular, I am grateful to Dr. Cary Hill, Peter Gartland and Yujie Cheng for their technique help and blessed friendship. My gratitude also goes to my friend and colleagues, Dr. Lingmei Ma, Amiya Behera, Ruohui Wang, Crystal, Nan Wu, Scott Zhang, Dr. Michael Fraser, Aram Lee, Mohammad Al-Mamun, Dr. Kathy Wang, Dr. Baigang Zhang, Dr. Jihaeng Yi, Tyler Shillig, Georgi Ivanov, Keith Depew, Guo Yu, Dr. Islam Ashry, Dr. Ishac Kandas, Chennan Hu, Brennan Thews, Shuo Yang, Jiaji He, and Dr. Xiangyu Wei.

I am especially indebted to Dr. Desheng Jiang, who provided me the most important recommendation for my Ph.D. study. A special thanks go to Dr. Minghong Yang for his unlimited support in my life and professional suggestions on the academic research.

Thanks to my sponsors, Department of Energy(DOE) for their support on my research and Chinese Scholarship Council(CSC) on part of my scholarship. I hope that my accomplishment could well reflect their generous contribution.

Finally, I would like to express my deepest gratitude to my parents. Their endless love and unwavering support have helped me to go through all difficulties. And the biggest love and thanks to my wife for her constant love, understanding and accompany. This work could not be finished without her support and there are no words that could convey my gratitude and love to all she has endured for our family.

TABLE OF CONTENTS

TABLE OF CONTENTS

1 INTRODUCTION

1.1 Motivation

The struggle for high-efficiency technology, clean energy, and reduced emissions has driven human society in the 21st century. A secure and efficient source of energy is critical to the stability and prosperity of the whole world. Many novel technologies have been developed daily to fulfill this goal. From optical tools for deep ocean monitoring and research[1] to the imaging and spectrometry systems in Voyager 1[2] for vast universe exploration, optical sensors are playing critical roles in scientific research and each individual's life. In many industry applications, optical fiber sensors have unique advantages over traditional technologies due to their miniature size, long-term stability, corrosion resistance and immunity to electromagnetic interference.

From 2000 to 2014, the United States produced more than a billion short tons of coal each year, and more than 90% of this coal was used by power plants to generate approximately 40% of the country's electricity[3]. And it is realized that the emission of greenhouse gases (GHGs) threatens all humans' health and welfare due to the long-lasting changes in the climate. The fossil fuel-fired electric generating units (EGUs) are thought to be the primary emitters of GHGs, in the form of CO_2. As a result, the Energy Policy Act of 2005 and the Clean Power Plan of 2015 commit to regulate power generation and promote research and development of novel clean technologies. As an effect of these policies, the electricity demand growth predicts that the share of coal in electricity generation will not drop but keep constant at 32% for the next 25 years. Thus there is a strong desire to improve heating rates at coal-fired steam EGUs. New sensors and technologies are needed to contribute to the goal of developing "seamless, integrated, automated, optimized, intelligent" coal-derived power plants. Technologies such as the unique integrated gasification combined cycle (IGCC) configuration of turbines and the Ultra Super Critical (USC) steam cycle designs have contributed to this purpose by improving efficiencies and reducing CO_2 emissions. Real-time, accurate and reliable monitoring of ultra-high temperatures at various locations in the gasifier can allow the operator to optimize the performance of IGCC and USC plants. Operating conditions must be continuously monitored and modified to avoid catastrophic events. Furthermore, real-time monitoring of spatial and temporal distributions of temperatures in power plants will help operators

to better understand the whole system health condition, improve the working efficiency, minimize the waste, and decrease the cost.

In 2013, nuclear power was the third largest energy resource, providing about 19% of the total electricity in the United States[3]. Nuclear reactor vessels demand high-temperature and high-pressure capabilities, as they are exposed to temperatures up to 375 °C, pressures up to 15.2 MPa and intense radiation fields[4]. The Fukushima Daiichi nuclear disaster emphasizes the need for new reliable monitoring technologies[5]. Furthermore, aircraft structure and engine temperature monitoring require miniature and reliable sensors.

Mature fiber optic sensing technologies are attractive options for these applications. Many successful technologies are widely used in industry, such as F-P interferometry[6] and FBG based sensors[7]. However, F-P interferometers are point sensors, and multiplexed FBG based sensors are a quasi-distributed sensing technique. Mature technology for fully-distributed temperature sensing primarily relies on Rayleigh scattering[8, 9], Brillion scattering[10, 11], or Raman scattering[12-14]. Both Rayleigh and Brillion scattering are temperature and strain/pressure dependent leading to signal demodulation difficulty and potential errors due to the temperature-pressure crosstalk. Raman scattering is pressure insensitive[15], making it a promising method in hash environments. Although Raman scattering is much weaker than Rayleigh scattering, the signal to noise ratio (SNR) can be easily enhanced by employing a high power laser and sensitive photodetectors. Furthermore, the Raman scattering is a self-calibrating technology which makes the method more reliable.

Raman scattering in graded-index multimode fiber has long been recognized as a mature method of distributed temperature sensing [16-18]. This technique is also demonstrated in single mode fiber both theoretically and experimentally [19, 20]. However, fused silica is not able to withstand temperatures in excess of 800 ºC, prohibiting its use in critical temperature monitoring for applications such as power production and coal gasification. Sapphire fiber has attracted more interest in the Raman sensing field in recent years due to its broad spectral transmission range, high melting point (~2053 ºC) and corrosion resistance. The high-temperature stability and chemical corrosion resistance of sapphire fiber has made it the only choice in highly corrosive, high-temperature sensing applications above 1200 ºC. The temperature dependence of Raman

active mode frequency, width[21] and pressure[15] in bulk sapphire has been reported. When the sapphire fiber is contaminated, it is difficult to extract the intensity change required for temperature sensing using Raman Stokes peak analysis due to fiber loss. Perhaps more significantly, the Stokes peaks are less sensitive than the Anti-Stokes peaks. However, few have reported observations about the Raman Anti-Stokes peaks because they require much higher laser power to observe and such power is very close to the damage threshold of the sapphire fiber.

The objective of this research is to design and develop a sapphire fiber-based Raman distributed ultra-high temperature sensing technique using the combination of the Anti-Stokes and Stokes technique. This is a first-of-its-kind technology that operates reliably at an ultra-high temperature up to 1400 ºC and is capable of monitoring the space and time varying thermal properties of power plant components such as gas turbines, gasifiers, and boiler furnaces.

1.2 Scope of the research

In this research, Raman Anti-Stokes scattering in sapphire fiber was reported for the first time. The temperature dependence of the Raman peak intensity, frequency and width was studied. Based on this new discovery, for the first time to our knowledge, we present a sapphire fiber-based Raman distributed temperature sensing system from room temperature up to 1400ºC. These sensors are suitable for coal gasifiers in which the environment is corrosive, for aerospace engines and turbines requiring compact sensing elements and boilers with high-pressure environments.

The efforts devoted to this innovative sensing technique focus mainly on the following issues.

1) The study of the general Raman techniques in silica fiber;
2) The comprehensive design of sapphire fiber-based Raman DTS system;
3) The temperature dependence of sapphire Raman characteristics;
4) The results of sapphire fiber-based Raman DTS system;

The principle of traditional Raman DTS is presented in Chapter 2, including Raman Optical Time-Domain Reflectometry (OTDR) and Raman Optical Frequency-Domain Reflectometry (OFDR).

This chapter introduces the general principles in Raman DTS system design and serves as a guidance for commercialization and research regarding the Raman DTS system. The system design is introduced in Chapter 3. The estimation of system spatial resolution and relative temperature resolution is presented. The characteristics of blackbody radiation, fluorescence, attenuation and the numerical aperture of sapphire fiber are analyzed and tested. A critical lens for optical coupling is discussed in details. Chapter 4 is dedicated to the system sensor fabrication and experimental results of Raman DTS in sapphire fibers. Chapter 5 summarizes the research work and proposes future research directions and suggestions for improvements.

2 TRADITIONAL DISTRIBUTED TEMPERATURE SENSING SYSTEM

Simultaneous collection of temperature information from many different positions is one of the common problems in daily life. Fully distributed temperature sensing (DTS) systems constitute one major category in optical fiber sensors. Other DTS systems have been proposed, some of which suggest using acoustically-induced long period gratings[22, 23]. Many others employed optical scattering in silica fiber, including Rayleigh, Brillouin, and Raman scattering. According to the measurement domain, the DTS system can be divided into two categories: Optical Time-Domain Reflectometry (OTDR) and Optical Frequency-Domain Reflectometry (OFDR). In most cases, the position information is deduced from the fly-time from the scattering point to the photodetector. In this chapter, we present the brief introduction of three popular DTS systems in Section 2.1. The basic theory of Raman OTDR in silica fiber and sapphire fiber is discussed in Sections 0. The basic theory of Raman OFDR is introduced in Section 2.3. The requirements of sapphire fiber-based Raman OFDR technique are discussed.

2.1 Introduction of distributed temperature sensing method

The distributed temperature sensing system measures the temperature by means of optical fiber. When photons are emitted into a transparent or opaque material, the interaction of the photons with the material's molecules releases scattered photons. Through this consequence, Rayleigh, Brillouin, and Raman scattering can be measured for distributed temperature sensing purposes. The discovery of these three scattering mechanisms has already generated two Nobel Prizes in Physics and served our daily life.

The first one, Rayleigh scattering, was discovered by British physicist Lord Rayleigh (John William Strutt)[24] who found out that a portion of the scattered photons (at the order of 10^{-4} to 10^{-5} of the laser photons) had the same frequencies from the excitation frequency. This scattering is dominantly elastic scattering by the particles much smaller than the wavelength. In general, the intensity of the scattering light is inversely proportional to the fourth order of the particle size. This scattering was named after Lord Rayleigh who was awarded the Nobel prize in 1904. The

application based on Rayleigh scattering has been demonstrated on single mode fiber with one-centimeter resolution and temperature up to 850ºC[25].

Leonid Mandelstam[26] and Léon Brillouin[27] discovered the second scattering mechanism in which intensity is about two orders smaller than Rayleigh scattering with shifted frequencies from the excitation light. Higher frequency components are called Anti-Stokes while the lower frequency components are named Stokes. This inelastic scattering is mediated by the refractive index dependence of the light-induced deformation and distension. This discovery is named "Brillouin-Mandelstam light scattering(BMS)" to honor their contribution *(Mandelstam recognized this possibility of scattering as early as 1918 but only published it 1926 while Brillouin published his discovery in 1922[28])* and usually is shortened to "Brillouin scattering". BMS has been widely used in temperature sensing and strain sensing since the 1990s. One is called Brillouin Optical Time Domain Analysis (BOTDA) and the other is "Brillouin Optical Frequency Domain Analysis (BOFDA)". Bao[29] developed simultaneous temperature and strain measurement using a Brillouin grating technique with a spatial resolution of 20 cm and a temperature accuracy and strain accuracy of 0.4 ºC and 9 με in a Panda fiber. The spatial resolution based on BODTA technique is 0.5 m in a 50-km single mode fiber. The maximum sensing length can be extended to 100-km with a spatial resolution of 2 m. The drawbacks of the DTS system based on Rayleigh scattering and Brillouin scattering are the crosstalk of temperature dependence and strain dependence. To calibrate this crosstalk, it usually requires two optical fibers in parallel or other expensive and complex configurations. For example, the bonded fiber is used for strain measurement and another free fiber is used for temperature measurement to compensate for the temperature effect on the bonded fiber[30].

C. V. Raman[31] and his student K. S. Krishnan[32] carried out the ground-breaking work at light scattering in which the resulting discovery was named "Raman scattering". C. V. Raman has rewarded the Nobel Prize in Physics in the 1930s. Raman scattering is another inelastic scattering occurrence due to the interaction of light with the vibration and rotation of the material molecules. Similar to Brillouin Stokes and Anti-Stokes, the Raman scattering light at a longer wavelength (lower frequency) is called Raman Stokes and the one at a shorter wavelength (higher frequency) is called Raman Anti-Stokes. The Raman scattering intensity depends on the material type,

concentration, and temperature. Because each molecule/material has its unique vibration and rotation modes, this fingerprint character is widely used in material identification, biological and medical applications. Temperature sensing is only one of its applications. Comparing with BMLS in silica fiber, Raman scattering components are much "further" away from excitation laser. For example, the Brillouin Stokes signal of a silica fiber is about 80 pm away from the laser light at 1550 nm while the Raman Stokes signal is about 113.4 nm from the laser light. The gain of Raman scattering is about 1 to 2 orders lower than Brillouin scattering. Applications in the 1980s with lower-powered lasers required 10^6 measurements to achieve sufficient signal to noise ratio. As high- powered lasers and highly sensitive photodetectors became available, this requirement no longer impeded the development of Raman DTS. Figure 2-1 illustrates the relationship of incident light, Rayleigh scattering, Brillouin scattering and Raman scattering.

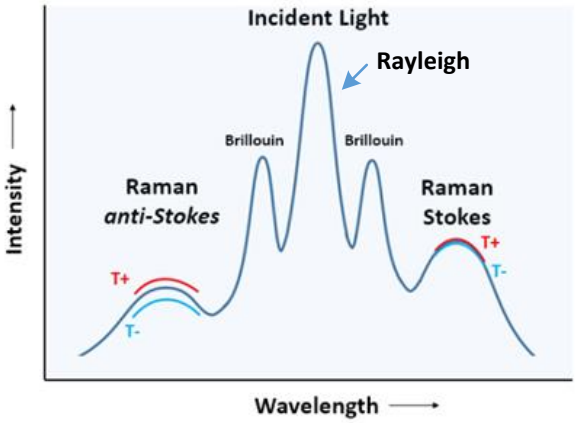

Figure 2-1. Illustration of optical scattering mechanisms

However, there are some other differences between the three scattering mechanisms which are summarized in Table 2-1. In particular, the Raman-based DTS can only work at spontaneous scattering conditions. The Stimulated Raman intensity and frequency highly depends on the laser power[33] and is thus not reliable for temperature sensing. This conclusion is drawn based on general applications. for example, the Raman scattering is only sensitive to temperature, but in some extreme conditions, the Raman frequency of sapphire fiber may shift tens of cm^{-1} under the pressure of 10 kBar[15].

Table 2-1. Comparison of Rayleigh, Brillouin and Raman scattering in DTS system

	Sensing condition	Fiber	Intensity	Collision type	Sensing parameters	Direction in fiber
Rayleigh scattering	Stimulated & Spontaneous	SMF & MMF	High	Elastic	Pressure & Temperature	Forward & backward
Brillouin scattering	Stimulated & Spontaneous[34]	SMF & MMF[35]	Middle	Inelastic	Pressure & Temperature	Backward
Raman scattering	Spontaneous	SMF & MMF	Low	Inelastic	Temperature	Forward & backward

Both Rayleigh and Brillouin scattering are sensitive to local refractive index, so they are used for simultaneous temperature[25] and strain sensing[36, 37]. However, the cross-talk between temperature and other sensitive parameters requires careful calibration which increases the complexity of the whole system. On the contrary, Raman scattering is only sensitive to temperature. Such a characteristic makes it intrinsically promising for harsh environment sensing. Nowadays, Raman distributed temperature sensing (RDTS) systems have been one of the most successful and practical technologies and is widely used for oil downhole, pipe-line leak monitoring, tunnel fire alarm, and structure health monitoring.

From a quantum-mechanical viewpoint, the incident laser photon first excites the electron from the ground state to a virtual state. When the electron goes back to a vibrational state, certain Raman modes will generate low-frequency Stokes photons, and when the electron is excited from a vibrational state to the virtual state and then back to the ground state, higher (Anti-Stokes) photon energy is released. Since the Anti-Stokes requires the presence of vibrational states, the Anti-Stokes are usually much weaker than Stokes[38]. However, the Raman Anti-Stokes signals are more sensitive than Stokes signals but they undergo the same laser fluctuation and fiber attenuation. Thus, the ratio of Anti-Stokes over Stokes is useful for temperature demodulation and calibration.

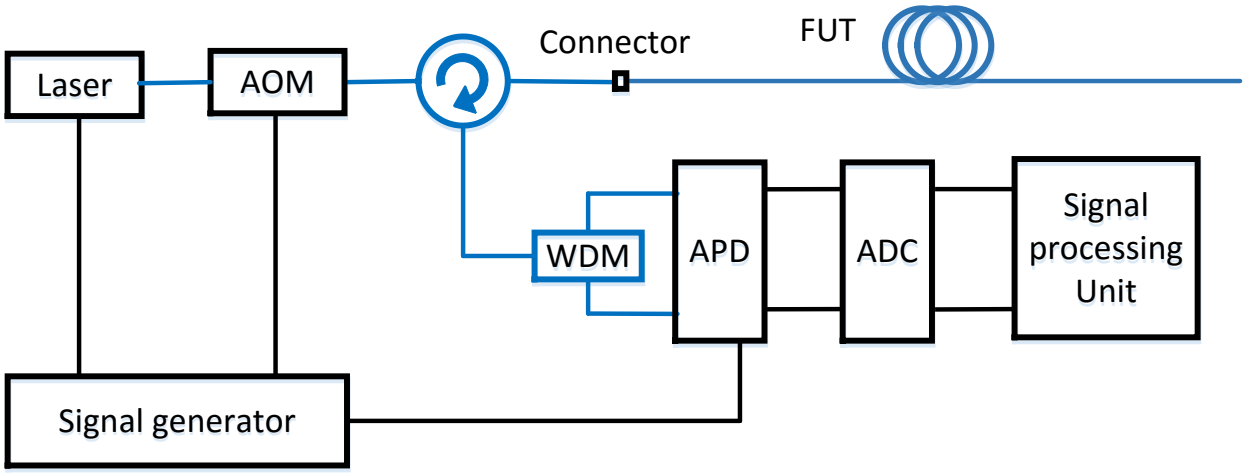

Figure 2-2. Typical silica-fiber-based Raman DTS system

Raman DTS systems have been widely used since the 1980s[39] for industrial applications including fire alarm systems, subway temperature monitoring, and oil pipeline leakage detection. Figure 2-2 illustrates a typical silica-fiber-based Raman DTS system. The light source is composed of a pulsed laser or a Continue-Wave (CW) diode laser with Acoustic-Optical-Modulator (AOM). This technique was first demonstrated in graded index multimode fiber. After high sensitivity detectors were invented, single mode fiber replaced multimode fiber and has great advantages in long distance sensing due to its low attenuation. The backward Raman scattering light was separated by Wavelength-Division Multiplexing (WDM) into Stokes and Anti-Stokes. The photodetector is usually a high-speed Avalanche photodetector, or Photomultiplier tube (PMT). Single photon avalanche detectors are used for centimeter-resolution DTS systems. In some cases, a transimpedance amplifier (TIA) will further amplify the weak signals. The signals are converted by the Analog-digital converter and analyzed by the signal processing unit which is usually a computer. A brief review of the Raman DTS development history is shown in Table 2-2. It indicates that the optical wavelength shifted from visible light to C-band attributable to the lower cost of components at the C-band. The spatial resolution is determined by the bandwidth of the photodetector and the pulse duration time of the laser. So far, the best spatial resolution on the order of 1 cm was obtained with a femtosecond laser and superconducting nanowire single-photon detectors[13]. The spatial resolution of a commercial Raman DTS system is about 1 meter with

several tens kilometers sensing length and the temperature resolution is usually on the order of 1 ºC[14].

Table 2-2. Developing history of Raman DTS system

Year	Wavelength	Type	Fiber	Amplifier	FWHM	Pulse width	Resolution
1985 [40]	514nm	PMT	MMF	-	-	15 ns	3 m
1995 [41]	850nm	SPAD	MMF	-	-	500 ps	0.4m
1999 [42]	647nm	PMT	PMF	TIA	3.5 ns	35 ps	-
2006 [43]	1550nm	APD	SMF	TIA	-	-	17 m
2007 [44]	1064nm	-	MMF	-	-	6.25 ns	1 m
2007 [45]	1550nm	APD	MMF	TIA	3 MHz	-	17 m
2011 [13]	1550nm	SNSPD	SMF	-	85 ps	-	0.012 m
2011 [14]	1550nm	APD	SMF	TIA	10 ns	-	1 m

2.2 Raman Optical Time-Domain Reflectometry

Raman frequency shifts are the distance from the Raman Stokes wavelength to the excitation wavelength, which is usually reported in units of wavenumbers, as the Stokes and Anti-Stokes peaks are symmetric to the excitation peak in the wavenumber spectrum. The Raman shifts are determined by[46]

$$\Delta\omega(\mathrm{cm}^{-1}) = \left(\frac{1}{\lambda_0(\mathrm{nm})} - \frac{1}{\lambda_S\,(nm)} \right) \times \frac{(10^7\,nm)}{(cm)} \qquad \textbf{(2-1)}$$

$$\Delta\omega(\mathrm{cm}^{-1}) = \left(\frac{1}{\lambda_{AS}\,(nm)} - \frac{1}{\lambda_0(\mathrm{nm})} \right) \times \frac{(10^7\,nm)}{(cm)} \qquad \textbf{(2-2)}$$

where $\Delta\omega$ is the Raman shifts expressed in wavenumber, λ_0 is the excitation wavelength in units of nanometers, λ_S and λ_{AS} denotes the Raman Stokes wavelength and Raman Anti-Stokes wavelength, respectively.

Silica fiber has a broad-band Raman frequency shift with its peak at 440 cm^{-1} while sapphire Raman spectrum is represented by 7 peaks located at 379, 418, 431, 450, 578, 645 and 750 cm^{-1}, in which 418, 578 and 750 cm^{-1} are the major peaks. The Raman spectrum position is determined by the excitation wavelength. Figure 2-3 shows part of the sapphire Raman peaks' position and range which span from the minimum wavelength of the Anti-Stokes peak to the maximum wavelength of the Stokes peak. It indicates that the Raman peaks will spread in a wider range at a longer laser wavelength. For example, the range is 365.6 nm when the laser wavelength is 1550nm while the range becomes only 42.6 nm at a laser wavelength of 532 nm.

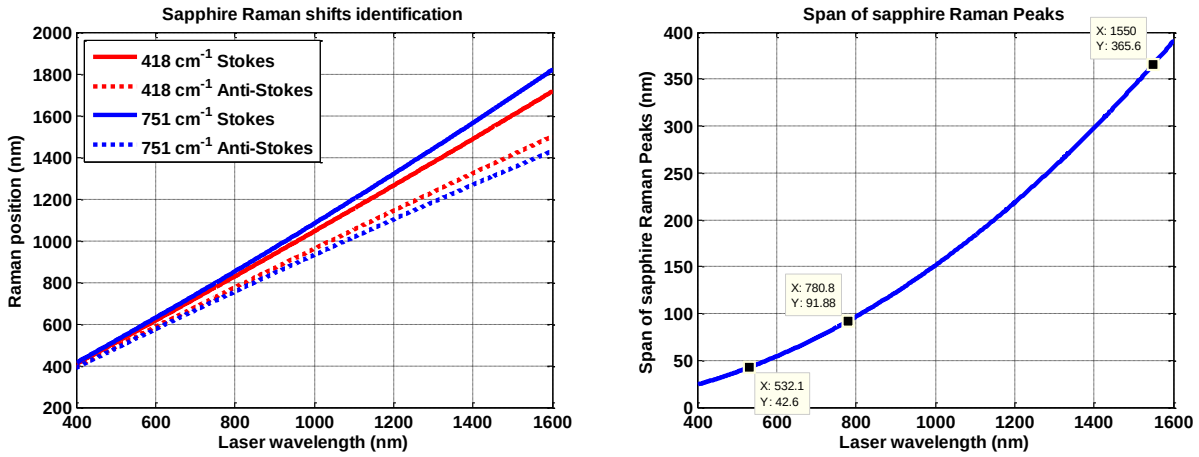

Figure 2-3. Sapphire Raman Spectrum position (left) and range (right)

The Raman intensities of the Anti-Stokes and Stokes components are proportional to their differential cross sections given by[41]

$$\left.\frac{d\sigma_{AS}}{d\Omega}\right|_x \cong \frac{1}{\lambda_{AS}^{\ 4}} \frac{1}{\exp\left[\frac{hc\Delta\upsilon}{K_B T(x)}\right]-1} \qquad \textbf{(2-3)}$$

$$\left.\frac{d\sigma_{S}}{d\Omega}\right|_x \cong \frac{1}{\lambda_{S}^{\ 4}} \frac{1}{1-\exp\left[-\frac{hc\Delta\upsilon}{K_B T(x)}\right]} \qquad \textbf{(2-4)}$$

where h is Plank's constant, c is the velocity of light in vacuum, K_B is Boltzmann's constant, λ is the wavelength of Stokes or Anti-Stokes, $\Delta\upsilon$ is the Raman frequency shift, and T is the absolute temperature at locale position x.

The relationship between Raman intensity and temperature for a Raman frequency shift of 440 cm^{-1} is shown in Figure 2-4. The equations predict that the Anti-Stokes components are more sensitive to temperature variation than Stokes components. For this reason, Stokes components are usually used for calibration purpose.

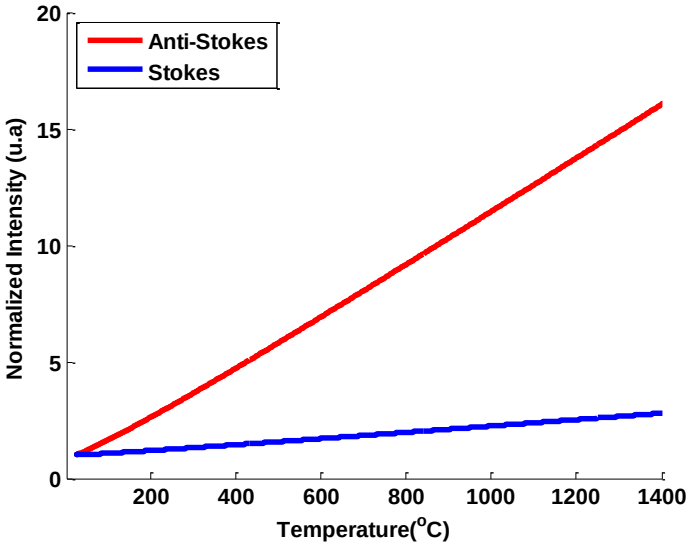

Figure 2-4. Theoretical simulation of Raman Anti-Stokes and Stokes signal response at a frequency shift of 440 cm^{-1}

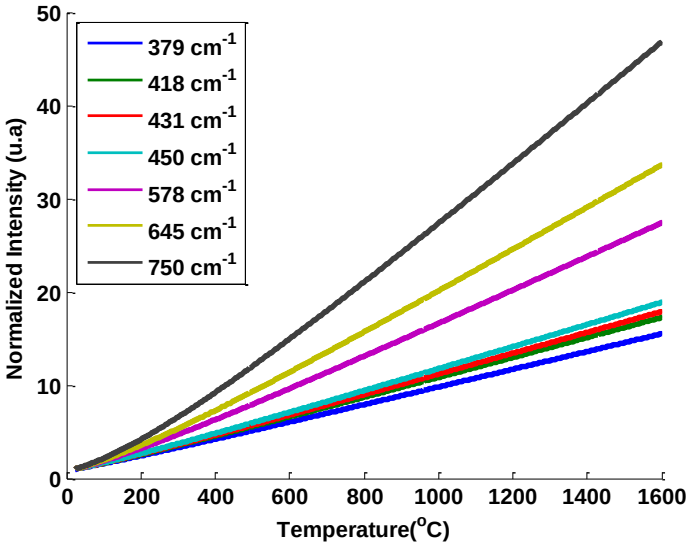

Figure 2-5. Simulation of sapphire fiber Anti-Stokes signal response at different temperatures

The theoretical temperature responses of all 7 peaks in sapphire fiber are shown in Figure 2-5. Since the temperature responses of these peaks are not linear, an accurate calibration process would require at least 7 points because the final signal intensities also depend on the initial intensity amplitude of these 7 peaks.

2.3 Raman Optical Frequency-Domain Reflectometry

Optical Frequency-Domain Reflectometry (OFDR) was demonstrated based on Rayleigh[47], Brillouin[29] and Raman scattering[48]. OFDR may refer to the modulation of the laser frequency[49] or the modulation frequency of the laser intensity[50]. Based on the type of light source, OFDR can be categorized into Coherent OFDR (COFDR) and Incoherent OFDR (IOFDR). COFDR depends on the frequency modulation (~281 GHz) of the coherent light source wavelength in silica fiber at C-band. It can achieve spatial resolution in the order of light wavelength (~50 μm[51]) but limited by the coherent length of the laser(several hundred meters). ICOFDR, on the other hand, modulates the frequency of the laser intensity. Its spatial resolution is determined by the maximum modulating frequency (~200 MHz). Its spatial resolution can reach 1 m[52]. IOFDR was first invented by Ghafoori-Shiraz[53] in 1986 for fault detection in

the graded-index multimode fiber using Rayleigh scattering. Soon, this method was adapted for Raman IOFDR for temperature measurement. The temperature information was obtained by the inverse Fourier transform of the measured data. IOFDR uses an affordable diode laser so this system is low cost and very competitive. In this section, the theoretical analysis of IOFDR is introduced.

Assume that an initial laser intensity I_0 is sinusoidal, modulated by a frequency f_m and modulation depth m. The laser power arrived at a position z can be expressed by[52]

$$I_p\left(z,t,\omega_m\right) = I_0 \cdot e^{-\alpha_p z}\left\{1-m+m\Re e\left[e^{i\omega_m t - iK_p z}\right]\right\} \quad \textbf{(2-5)}$$

where α_p is the attenuation coefficient of the pump laser, ω_m is the angular frequency defined by $\omega_m = 2\pi f_m$ and K_p is defined by

$$K_p = \frac{2\pi n_p f_m}{c} \quad \textbf{(2-6)}$$

where n_p is the refractive index of the pump laser and c is the speed of light in vacuum.

The Raman power at the photodetector corresponding to position z then is affected by the temperature and different attenuation due to the different wavelengths (Stokes or Anti-Stokes):

$$I_R\left(z,t,\omega_m\right) = I_0 \cdot \chi_R\left(T(\mathrm{z})\right) \cdot e^{-(\alpha_p+\alpha_R)\mathrm{z}}\left[1-m+m\cdot e^{i\omega_m t - i(K_p+\mathrm{K}_R)\mathrm{z}}\right] \quad \textbf{(2-7)}$$

where α_R is the attenuation coefficient of the Raman wavelength. $\chi_R\left(T(\mathrm{z})\right)$ is proportional to the differential cross section equation given in Equation (2-3) and (2-4). For a given refractive index of n_R at Raman wavelength, K_R is given

$$K_p = \frac{2\pi n_R f_m}{c} \qquad \textbf{(2-8)}$$

The optical power at time *t* arriving at the photodetector will be the integration of all Raman power along the fiber,

$$I_{R,d}(t,\omega_m) = I_0 \cdot \left\{ (1-\mathrm{m}) \int_0^L \chi_R(T(\mathrm{z})) \cdot e^{-(\alpha_p+\alpha_R)\mathrm{z}} dz + m \cdot e^{i\omega_m t} \cdot \int_0^L \chi_R(T(\mathrm{z})) e^{-(\alpha_p+\alpha_R)\mathrm{z} - i(K_p+K_R)z}\, \mathrm{dz} \right\}, \qquad \textbf{(2-9)}$$

where L is the length of the fiber.

Figure 2-6 shows simulation results of power received at the photodetector. The power is composed of a DC component and an AC component.

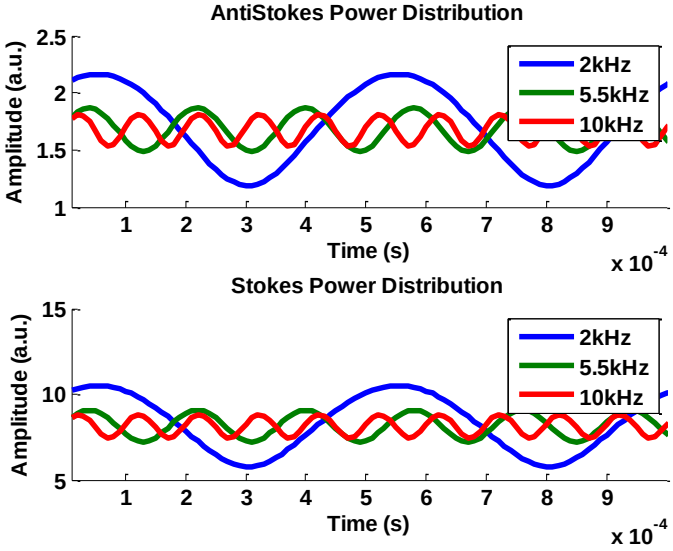

Figure 2-6. Simulation of power received at a photodetector as a function of time

If we use a short term "*DC*" to represents all the DC components in previous equation, it becomes

$$\tilde{I}_{R,d}\left(t,\omega_m\right)=DC+mI_0e^{i\omega_m t}\int_0^L S_R\left(z\right)\cdot e^{-iK_{PR}z}dz \qquad \textbf{(2-10)}$$

$$K_{pR}=K_p+K_R=\frac{2\pi f_m}{c}\left(n_p+n_R\right) \qquad \textbf{(2-11)}$$

$$S_R(\mathrm{Z})=\chi_R\left(T(\mathrm{z})\right)\cdot e^{-\left(\alpha_p+\alpha_R\right)z} \qquad \textbf{(2-12)}$$

After inverse Fourier transform to Equation (2-10), we are able to get $S_R(\mathrm{Z})$ for Raman Anti-Stokes and Stokes and then deduce the temperature information of T from Equation (2-3) and (2-4).

The limitation of this method is that the resolution is determined by the highest modulation frequency given by

$$\Delta z=\frac{c}{2nf_m} \qquad \textbf{(2-13)}$$

The power limit at a given frequency can be estimated from the AC component from Equation (2-10) and was given by Emir Karamehmedović[52],

$$\tilde{I}_R\left(\omega_m\right)=I_0\cdot\frac{\chi_R}{-\left(\alpha_p+\alpha_R\right)+iK_{PR}}\left\{\exp\left[-\left(\alpha_p+\alpha_R+iK_{PR}\right)L\right]-1\right\} \qquad \textbf{(2-14)}$$

Figure 2-7 shows the relationship between the spatial resolution and modulation frequency in an IOFDR system and the power limit is shown in Figure 2-8. It indicates that the modulation frequency has to be higher than 500MHz to reach 20 cm spatial resolution. However, when the modulation frequency is very high, the optical power limit is very low which is shown is Figure 2-8. Since the power at high frequencies is very weak and the lock-in amplifiers at higher frequencies are very expensive, this method is not suitable for short length temperature sensing, such as in sapphire fiber.

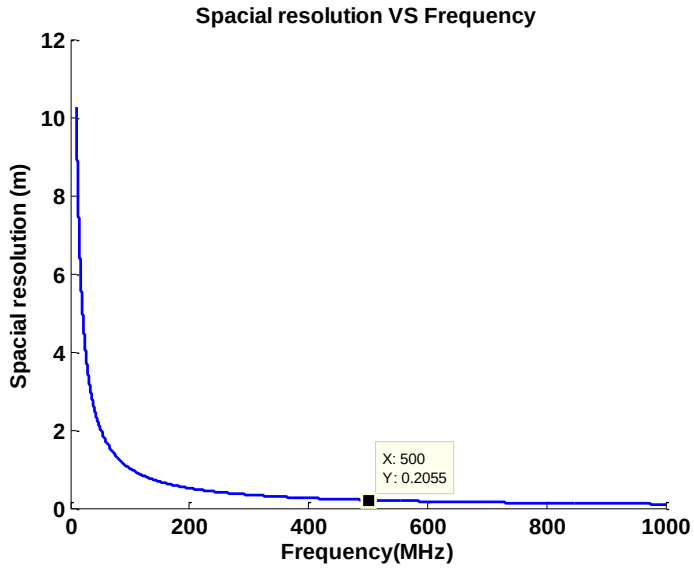

Figure 2-7. Spatial resolution as a function of modulation frequency in IOFDR system

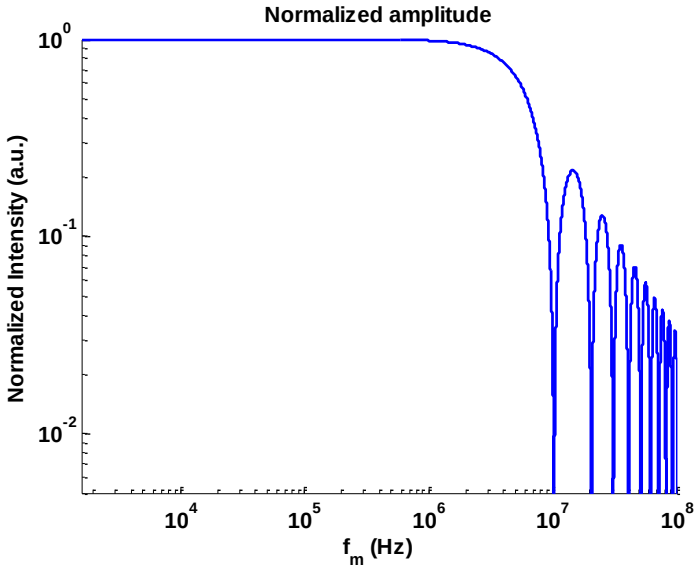

Figure 2-8. Normalized power limit for 10 meters long silica fiber

3 DESIGN OF SAPPHIRE FIBER-BASED RAMAN DTS SYSTEM

Traditional distributed temperature sensing techniques usually work below 800ºC due to the weak mechanical strength of silica fiber waveguides at high temperature. Sapphire fiber has been proven to be able to operate reliably at temperatures well above 1000ºC. In the proposed sapphire fiber-based Raman distributed ultra-high temperature sensing (DTS) system, the major challenges are strong blackbody radiation induced at high temperature, the use of sapphire fiber instead of silica fiber, and significantly higher spatial resolution requirements due to the short length of the sapphire fiber.

This chapter introduces the design of sapphire fiber-based DTS system. This chapter is organized as follows. Section 3.1 introduces the overview of the system design. It includes the schematic of the system and the relationships between devices and performance. The estimation of the system performance is introduced in section 3.2. The method for estimation of the spatial resolution and temperature resolution is presented. Some key parameters are introduced in the following sections. Since Raman scattering is the weakest scattering compared with Rayleigh and Brillouin, a higher laser power is required. However, the laser power cannot be infinitely high due to the threshold of Stimulated Brillouin Scattering (SBS) and Stimulated Raman Scattering (SRS). Section 3.3 gives guidance for the handling of this power limit in the system design. The Blackbody radiation background may saturate the photodetector in high-temperature applications. It may also mask the weak Raman signals. Section 3.4 presents a strategy to avoid the strong blackbody radiation. Section 3.5 introduces the experimental measurement of sapphire fiber fluorescence at different temperatures due to the impurity of Cr^{3+}. The attenuation of sapphire fiber is measured with different methods at 532 nm and 355 nm which are given in section 3.5.2. The numerical aperture measurement of sapphire fiber is presented in section 3.5.3. The coupling and alignment are discussed in section 3.6.

3.1 Overview of the system design

The Raman DHTS system requires a comprehensive and systematic design as all components and performance are interrelated. We first propose the whole system design and then analyze some key

parts. These analyses not only are required for this sapphire fiber-based Raman DTS system, but also help guide all related research regarding sapphire fiber in high-temperature measurement.

The proposed design of the sapphire fiber-based Raman DTS system is shown in Figure 3-1. A sub-nanosecond pulsed laser is required in this system because the spatial resolution mainly depends on the laser pulse duration and modal dispersion of the waveguide. The laser light is split by a beam splitter into two paths; one needs further attenuation before its coupling into the high-speed photodetector in which the corresponding signal will be used as a trigger signal. The other path will be coupled into the sapphire fiber for temperature demodulation. The backward scattering signal from the sapphire fiber will be partially reflected by the same beam splitter, then separated into Stokes and Anti-Stokes by a dichroic mirror and band pass filters and detected by the high-speed avalanche photodetectors (APDs). The data can be processed by a high-speed oscilloscope or a field programmable gate array (FPGA) based multi-channel analyzer and lock-in amplifier system.

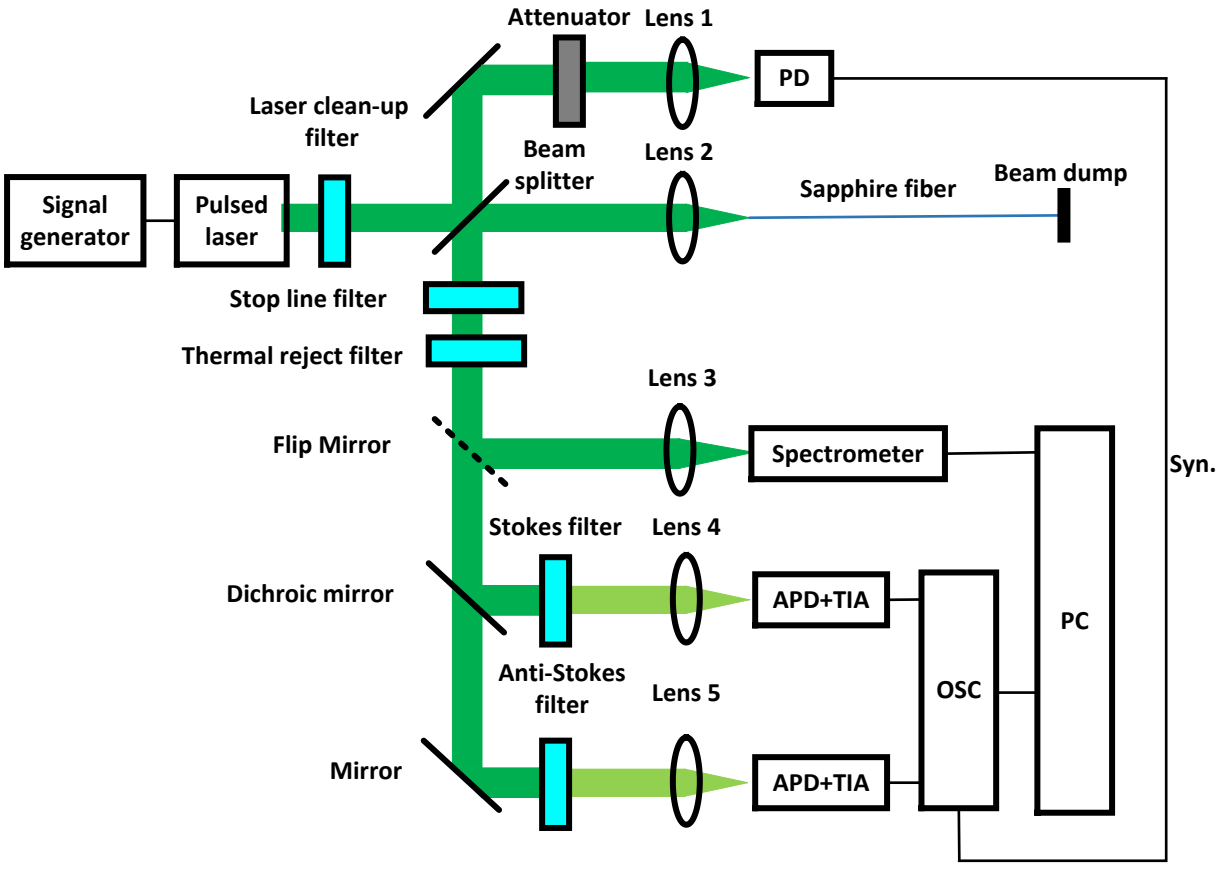

Figure 3-1. Overview of sapphire fiber-based Raman DTS system design

It is a systematic work to design the Raman DTS system. The key devices in this system include the laser, detector, waveguide and filters. The performance including the temperature resolution and spatial resolution can be estimated by the cross related parameters of the devices. The interrelated relationship is shown Figure 3-2. The laser wavelength, as the key parameter in Raman DTS system, will determine the parameters included in the green rectangle, including the intensity of blackbody radiation, fluorescence intensity, and attenuation of the waveguide, Raman gain and the responsivity of the detector. It shows that it is necessary to cautiously choose each device and check the estimated performance by the given device.

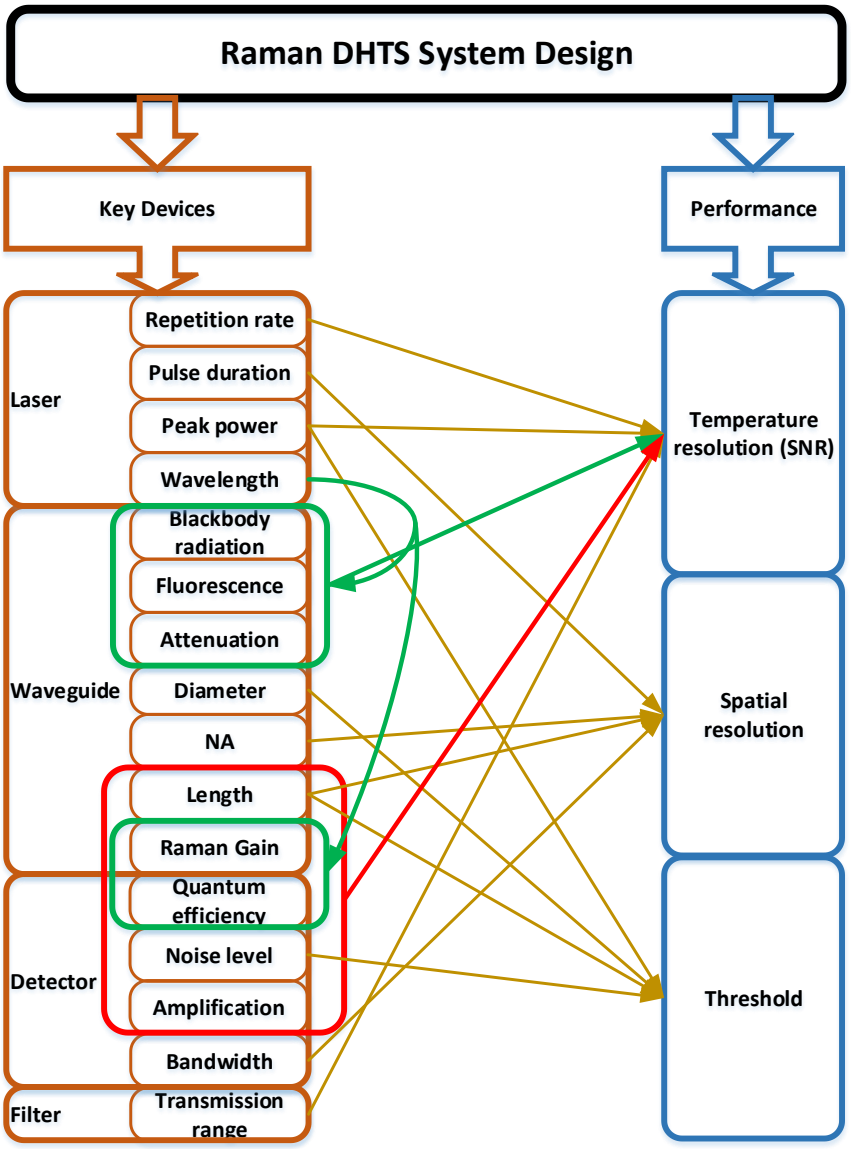

Figure 3-2. Schematic relationship of Raman DTS system design in sapphire fiber

In all parameters, choosing the right wavelength is the milestone and key in the system design. Shifting the wavelength may lead to the change of laser, detector, filter and also many parameters of the waveguides. For example, if the wavelength is too long, the Raman intensity will be small and buried by an intensive and noisy blackbody radiation. On the other hand, a too short wavelength may result in too little detecting efficiency from the photodetectors. The availability and cost of the laser and the filters are also concerns in the determination of the working wavelength.

3.2 Estimation of the system performance

3.2.1 Estimation of spatial resolution

The spatial resolution of a DTS system is usually defined by 10%-90% response distance to a temperature step or the full-width-at-half-maximum (FWHM) to an infinite short temperature pulse. It is well known that the modal dispersion of a multimode fiber is not negligible. The modal dispersion is due to the signal being carried by different modes which take different amounts of time to reach the fiber end. The time difference in silica fiber is given as[54]:

$$(\Delta t)_{\mathrm{mod}\,al} = \begin{cases} \dfrac{nL\Delta}{c}, Step-index \\ \dfrac{nL\Delta^2}{2c}, Graded-index \\ 0, Single-\mathrm{mod}\,e \end{cases} \quad \textbf{(3-1)}$$

where n is the refractive index of the fiber core, L is the fiber length, c is the speed of light in a vacuum, NA is the numerical aperture, and $\Delta = \frac{NA^2}{2n^2}$ (Assuming Δ<<1). The spatial resolution δL is defined by

$$\delta L = (\Delta t + t)\frac{c}{2n} \quad \textbf{(3-2)}$$

where t is the laser's original pulse duration time.

Since the traditional Raman DTS utilizes single mode fiber or graded-index multimode fiber, the spatial resolution is mainly determined by the laser pulse temporal duration. The theoretical spatial resolution of a graded-index MMF at 800nm is shown in Figure 3-3. It is seen that a diode laser with 2 ns pulse duration corresponds to 20 cm spatial resolution.

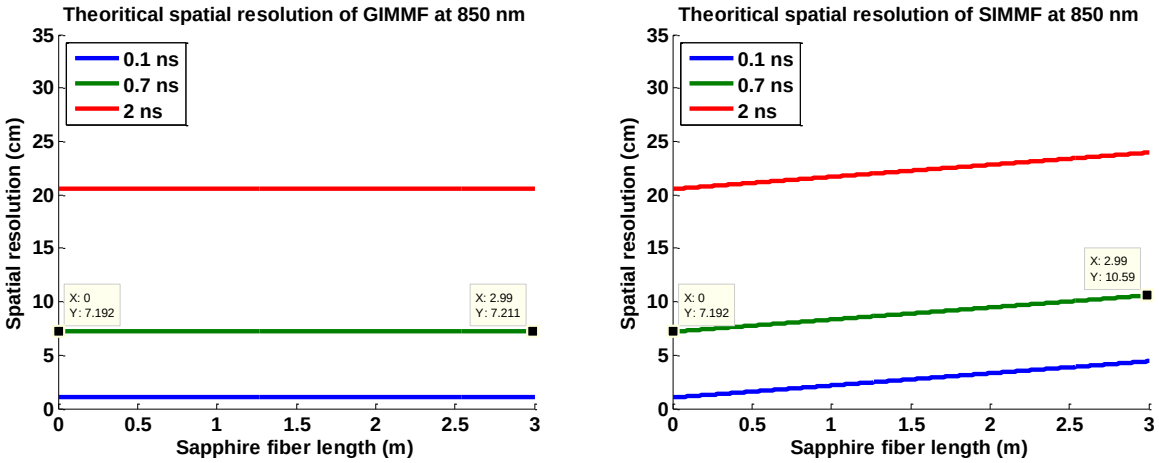

Figure 3-3. Spatial resolution simulation in graded-index silica MMF (left) and step-index silica MMF

However, Equation (3-1) holds only under the assumption of $\Delta \ll 1$. This assumption does not hold for unclad sapphire fiber. Figure 3-4 shows the principle of modal dispersion in a step-index multimode fiber.

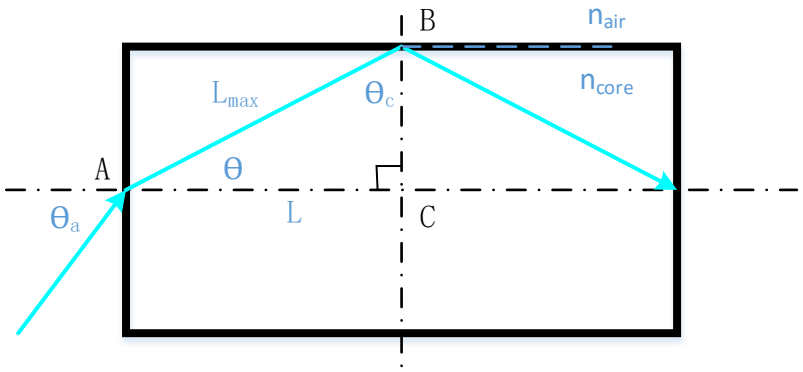

Figure 3-4. Illustration of modal dispersion in step-index multimode silica fiber

The model dispersion can be predicted by comparing the longest route which is determined by the critical angle of total reflection and the path parallel to the fiber axis.

In Figure 3-4, Θ_a is the acceptance angle and Θ_c is the critical angle in most step-index multimode fiber. We assume that in the triangle ΔABC, the hypotenuse is L_{max} while the lower one is L, so it is obvious that

$$\Delta L = L_{\max} - L = L/\cos\theta - L \qquad \textbf{(3-3)}$$

$$\frac{\Delta L}{L} = \frac{L/\cos\theta - L}{L} = \frac{1}{\cos\theta} - 1 = \frac{1}{\sqrt{1-\sin^2\theta}} - 1 \qquad \textbf{(3-4)}$$

Based on Snell's law, we obtain

$$n_{core} \cdot \sin\theta = n_{air} \cdot \sin\theta_a \qquad \textbf{(3-5)}$$

Putting Equations (3-4) into (3-5), we have

$$\frac{\Delta L}{L} = \frac{1}{\sqrt{1-\left(\frac{n_{air}\cdot\sin\theta_a}{n_{core}}\right)^2}} - 1 \qquad \textbf{(3-6)}$$

Usually, we define NA= $n_{air} \cdot \sin\theta_a$, so we obtain

$$\frac{\Delta L}{L} = \frac{1}{\sqrt{1-\left(\frac{NA}{n_{core}}\right)^2}} - 1 \qquad \textbf{(3-7)}$$

The final spatial resolution is

$$\delta L_{SF} = L\left(\frac{1}{\sqrt{1-\left(\frac{NA}{n_{core}}\right)^2}} - 1\right) + \frac{c}{2n}t \qquad \textbf{(3-8)}$$

It is clear that the spatial resolution of the system is composed of two components. The first term is related to the pulse width of the excitation laser, which is constant at all positions along the fiber. The second term reflects the pulse broadening effect introduced by modal dispersion, which gradually increases along the fiber. For example, for a sapphire fiber with measured NA value of 0.147 and the refractive index of 1.774 at 532 nm, for a given pulse width, the theoretical spatial resolution limit is shown in Figure 3-5.

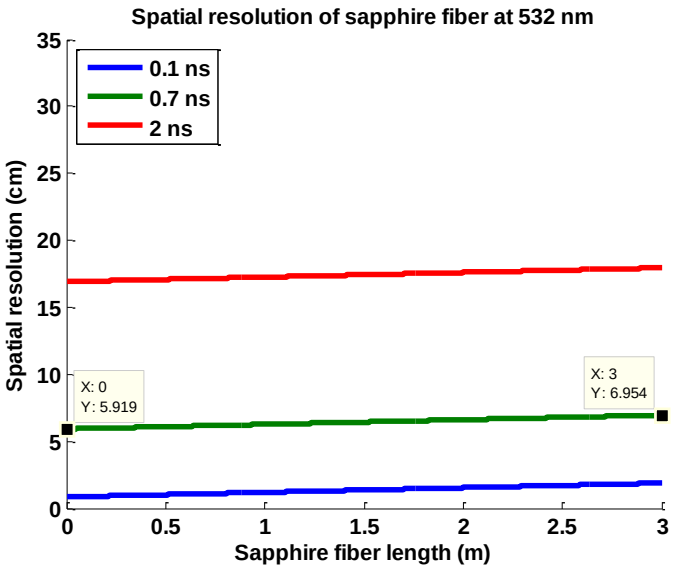

Figure 3-5. Spatial resolution simulation in sapphire fiber

Equation (3-8) also predicts that the spatial resolution can be improved by reducing the numerical aperture (NA). Assuming that the sapphire fiber is 1 meter long and the refractive index at 532 nm is 1.774, the theoretical spatial resolution is shown in Figure 3-6. A small NA can improve the spatial resolution of the system. A variety of methods were proposed to reduce the sapphire fiber model volume and numerical aperture, some of which include designing the sapphire fiber structure as star shape[55] or windmill shape[56]. In particular, etching the sapphire fiber with sulfuric/phosphoric acid solution had been demonstrated as a simple and practical way [57]. Since the etching process can be well controlled and consistent, the etched fiber diameter can be very accurate.

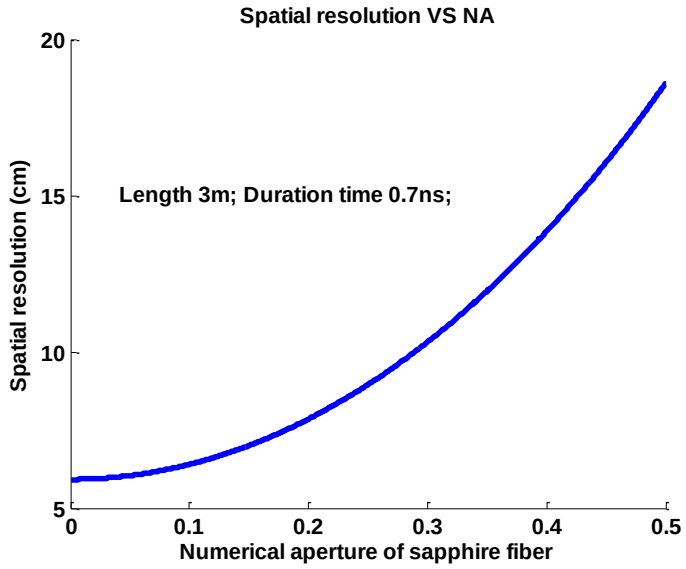

Figure 3-6. The spatial resolution of sapphire fiber as a function of NA

When the signal detection bandwidth of the system is not wide enough, the spatial resolution ΔL will be determined by the bandwidth as follows,

$$\Delta L = \frac{0.35}{f_{Limit}} \cdot \frac{c}{2n} \qquad \textbf{(3-9)}$$

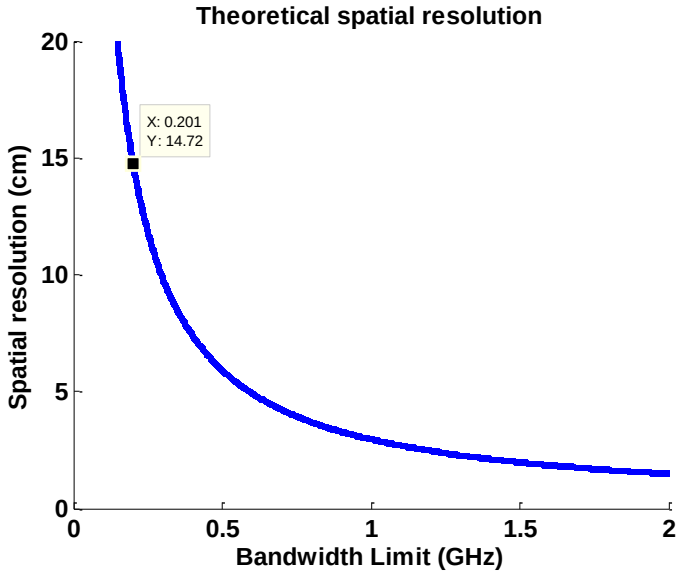

Figure 3-7. Theoretical spatial resolution limit

3.2.2 Estimation of temperature resolution

The estimation of temperature resolution is usually not accurate. But we are able to derive the temperature resolution by comparing all parameters with a known system and its temperature resolution. The temperature resolution is proportional to the following empirical formula,

$$\Delta T \propto \frac{e^{-\alpha L} \cdot \lambda^4 \cdot N}{A \cdot P \cdot \Delta t \cdot R} \sqrt{\frac{B}{f \cdot T}} \qquad \textbf{(3-10)}$$

where A is a coefficient depending on the fiber type. For graded-index MMF, $A = 1$ and for sapphire fiber $A \sim 0.01$; N is the noise equivalent power of the APD or noise level of the oscilloscope; P is the peak power of the laser; Δt is the laser pulse duration time; R is the responsivity of the photodetector; f is the laser repetition rate; T is the average time; α is the attenuation of the waveguide; L is the waveguide length; λ is the wavelength; B is the bandwidth limit of the system.

3.3 Laser selection and power limit

Since Raman scattering is one of the weakest scatterings, a high peak power laser is required. However, the laser peak is limited to the stimulated Raman scattering (SRS)[58] and Brillouin scattering (SBS) thresholds.

The pump light creates an acoustic wave in the transmission medium through “Electrostriction”. This acoustic wave induces spatially periodic local compressions and expansions which in turn cause local increases and decreases of the refractive index. This phenomenon is called the “Photoelastic Effect”. The modulation of the refractive index reflects the pump light in a backward direction. Thus, Brillouin scattering only exists in the backward direction. When the input power is sufficiently high, essentially 100% of the input power can be reflected back in a 1-cm path as a result of the SBS process[59]. The standard threshold of SBS is given by Smith[58]:

$$\frac{g_B P_B^{cr} L_{eff}}{A_{eff}} \approx 21 \qquad \textbf{(3-11)}$$

where g_B ~1×10^{-11}m/W, at 1 um wavelength, P_B^{cr} is the threshold power, A_{eff} is the effective area, L_{eff} is the effective length of the fiber defined by

$$L_{eff} = \left[1 - \exp(-\alpha_p \, \mathrm{L})\right] / \alpha_p \qquad \textbf{(1)}$$

where α_p is the fiber loss at pump frequency.

In silica fiber, this threshold is only 17 W for a 10 m single mode fiber. This threshold set the lowest critical power when the laser is working in single longitudinal mode and has a very fine width. However, when the pump light is multimode, SBS is not so important. For a broadband light source, the SRS plays the key role in the power limit.

When the laser power exceeds the SRS threshold, the Stokes components will grow rapidly. SRS Stokes cannot accurately predict temperature information because both the Raman Stokes spectrum and Raman gain change above the SRS threshold[60]. Furthermore, part of the laser power will convert into Stokes power and cause additional problems. The approximation of the SRS threshold is given by Smith[33]:

$$\frac{g_R P_R^{cr} L_{eff}}{A_{eff}} \approx C \qquad \textbf{(2)}$$

where g_R ~1×10^{-13}m/W, at 1 um wavelength, P_R^{cr} is the threshold power, A_{eff} is the effective area, C=16 at the forward direction, C = 20 at the backward direction, C = 40 at the backward direction and unpolarized case.

Although the SRS threshold is lower in silica fiber than in sapphire fiber, we use the SRS threshold in silica fiber as our power limit so that silica fiber can be used as the leading fiber. Figure 3-8 shows that a larger core fiber has a higher SRS threshold. The threshold will approach a constant number as the fiber length increases due to the fiber attenuation. For instance, the SRS threshold is 6.2kW and 132W for a 100 meter 62.5/125μm multimode fiber and single-mode fiber (SMF), respectively.

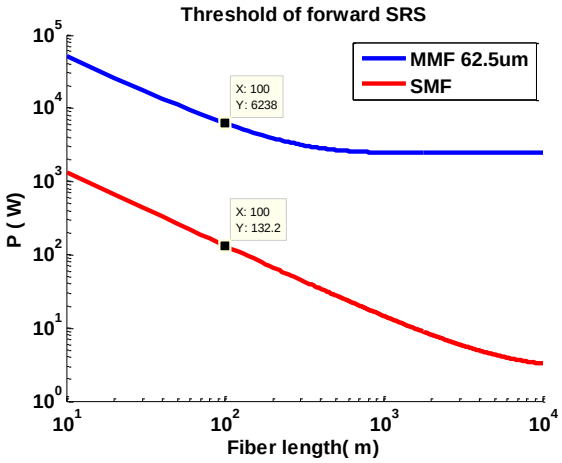

Figure 3-8. SRS threshold of silica fiber reduces at longer fiber length

3.4 Blackbody radiation

In the proposed system scheme, the first major challenge which will affect the detection of Raman signal is the background from blackbody radiation. The intense blackbody radiation at high temperature may mask the weak Raman signal. As an intrinsic radiation of all materials, the blackbody radiation is a special emission that is independent of any physical properties of the material itself. According to Planck's law[61], the radiation can be calculated as followed:

$$B(T) = \frac{2hc^2}{\lambda^5} \frac{1}{e^{\frac{hc}{\lambda k_B T}} - 1} \tag{1}$$

where B denotes spectral radiance, T is absolute temperature, k_B is the Boltzmann constant, h is Planck constant, λ is the wavelength, and c the speed of light in vacuum.

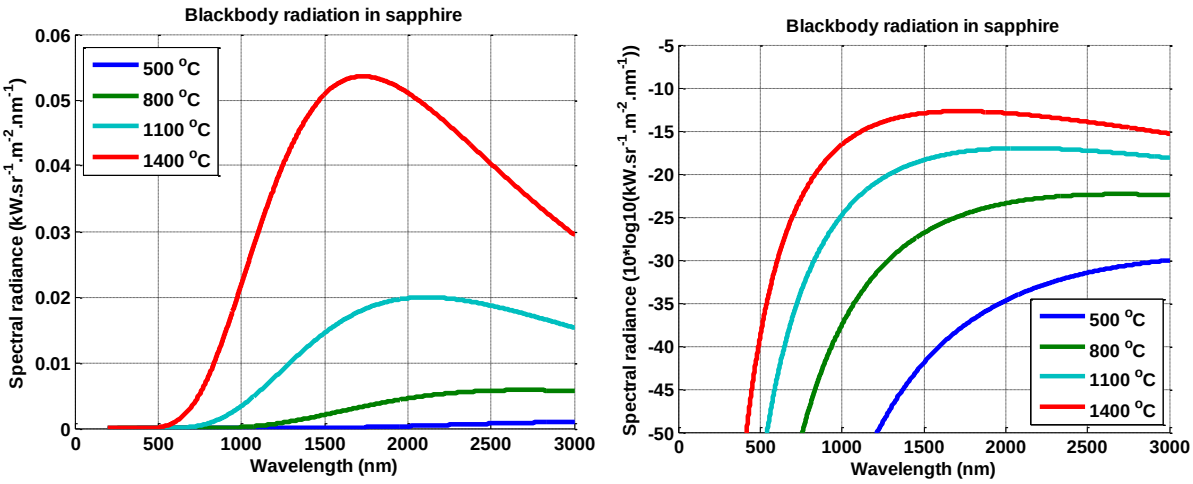

Figure 3-9. Simulation result of blackbody radiation in linear scale (left) and log scale (right).

The blackbody radiation usually described as spectral radiance. The theoretical result is plotted in Figure 3-9. It indicates that the peak of the blackbody radiation curve moves to lower intensities and longer wavelengths at a higher temperature. At 1400 °C, the peak of the blackbody radiation is around 1.7 μm. Compared with the wavelength of 1550 nm in telecom C-band, a shorter wavelength laser could efficiently avoid the blackbody radiation background[62-64] because the blackbody radiation intensity increases rapidly with respect to the wavelength less than 2 μm while Raman intensity is inversely proportional to the fourth power of the wavelength[38].

3.5 Character of sapphire fiber

3.5.1 Fluorescence of sapphire fiber

The analysis of blackbody radiation shows that a shorter laser wavelength is preferred in the Raman DTS system. However, some short wavelengths are not suitable due to the fluorescence of sapphire fiber. Fluorescence is a form of luminescence by a substance that has absorbed light. The emitted light usually has a longer wavelength which may have crosstalk with Raman signal. Strong fluorescence absorption at 694.3 nm in sapphire fiber was found due to Cr^{3+} ion impurities with a broad background when the laser light is intense [65-67]. Figure 3-10 shows the sapphire fiber fluorescence signal at room temperature. The center wavelength is at 694.3 nm with long tails

extending to relative broad wavelength range. It indicates that any Raman signal located from 550 nm to 694.3 nm will have crosstalk with fluorescence signal so it is recommended that the laser wavelength is lower than 550 nm or longer than 694.3 nm. For this reason, a laser wavelength of 532 nm and 355 nm avoids the strong background from thermal radiation as well as most of the fluorescence.

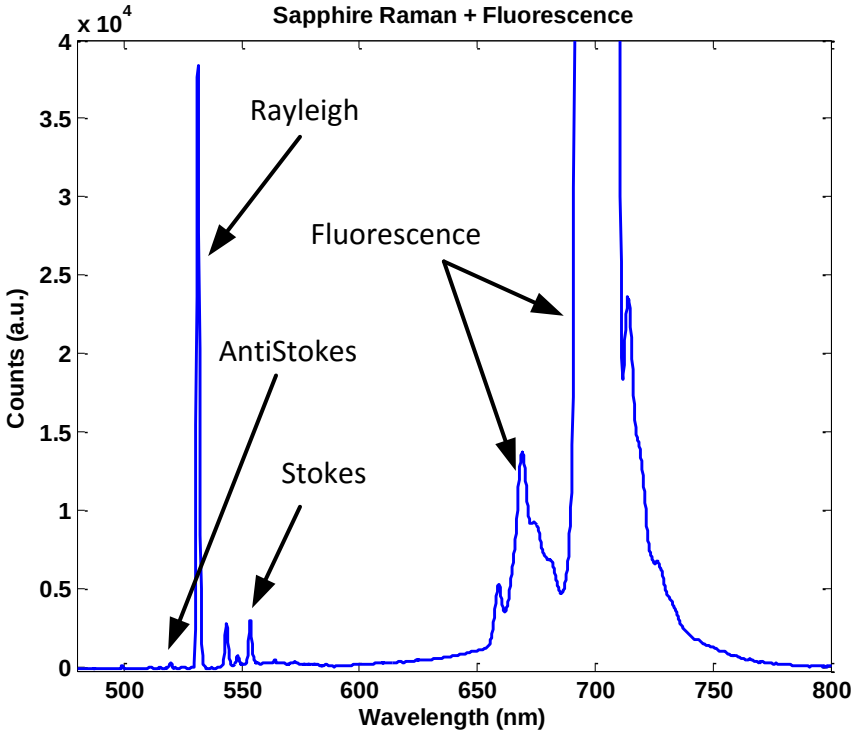

Figure 3-10. Sapphire fiber fluorescence signal at a room temperature.

3.5.2 Attenuation of sapphire fiber

For ultra-high temperature sensing, sapphire fiber is the only candidate because it has very broad spectral transmission range, and high melting point (2053 °C). Although a shorter wavelength has stronger Raman intensity, lower thermal background, and a lower crosstalk due to fluorescence, this preference may be countered by the increased attenuation of sapphire fiber and the decreased quantum efficiency of photodetectors. Silica-based photodetectors are commonly used for wavelengths lower than 1 um due to their high responsivity and lower noise in the spectral range of our interest. A shorter wavelength (<300 nm) light usually has a much lower quantum efficiency

which poses inherent experimental difficulties for UV spectroscopy. However, a laser with a wavelength between 550 to 694.3 nm is not good candidates due to the intensive fluorescence background. A typical responsivity of silica based photodetector is shown in Figure 3-11.

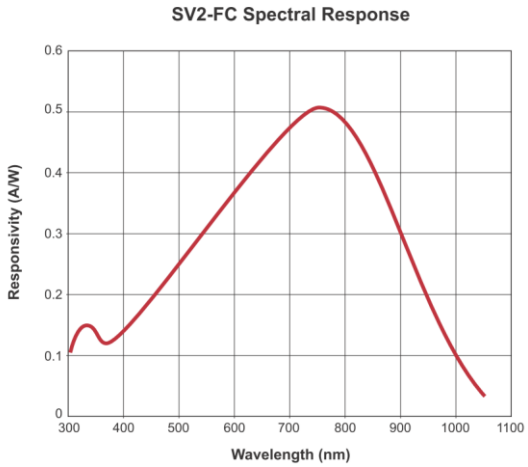

Figure 3-11. The responsivity of a silica photodetector (Thorlabs, SV2-FC).

From 300 nm to 550 nm, there are many lasers available at 355 nm and 532 nm which are usually the second harmonic and the third harmonic of the Nd-YAG laser. To acquire the knowledge required in choosing the best wavelength for the sensing system, the loss of the 75μm-diameter sapphire fiber was measured using three different setups. In all the setups, the sapphire fiber was first cleaned with acetone followed by alcohol, and then made into connectors. All experimental data were normalized to 1-meter fiber length. The first test was conducted with a high power broadband light source and an Optical Spectrum Analyzer (OSA), as shown in Figure 3-12(a). By calculating the transmission spectrum difference before and after adding the sapphire fiber (Figure 3-12 (b)), the attenuation of sapphire fiber at 532 nm was measured to be ~4.6 dB/m. The test was repeated with a Q-switched Nd: YAG laser at 532 nm (Continuum SLIII-10) and a photodetector (Thorlabs, SV2-FC), as shown Figure 3-13(left). By comparing the peak level difference, the attenuation of sapphire fiber at 532 nm was ~4.8dB/m which agrees with the first measurement results.

In the third test, a pulsed laser (Coherent, Flare355-500) and the same photodetector (Thorlabs, SV2-FC) were used to test the attenuation of the sapphire fiber at 355 nm, as shown in (Figure

3-14 (a)). The transmission peak level shows an attenuation of ~5.3 dB/m. It is noted that the calculated attenuation of sapphire fiber includes the loss at the joint between sapphire fiber and silica fiber and the loss induced by the sapphire fiber connect. The fabrication of sapphire fiber connect will be introduced in details in Section 4.1.1.

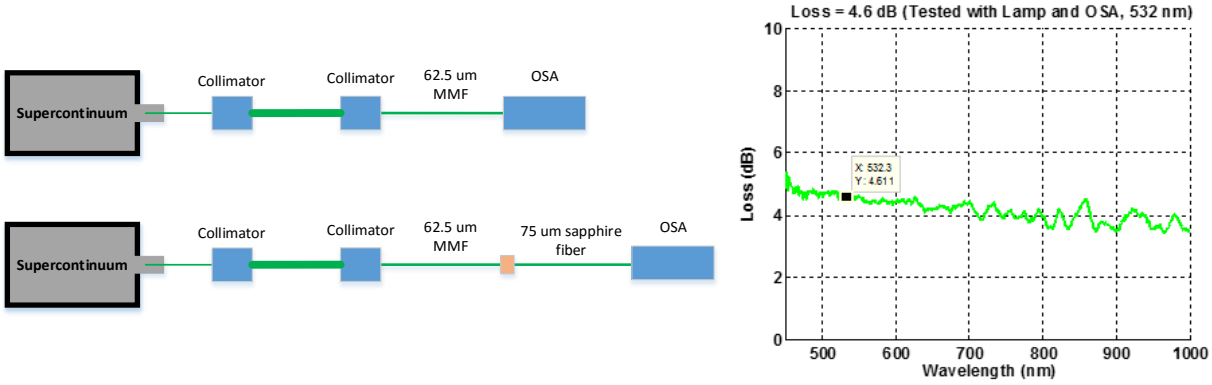

Figure 3-12. Sapphire fiber loss measurement with a supercontinuum light source and an OSA

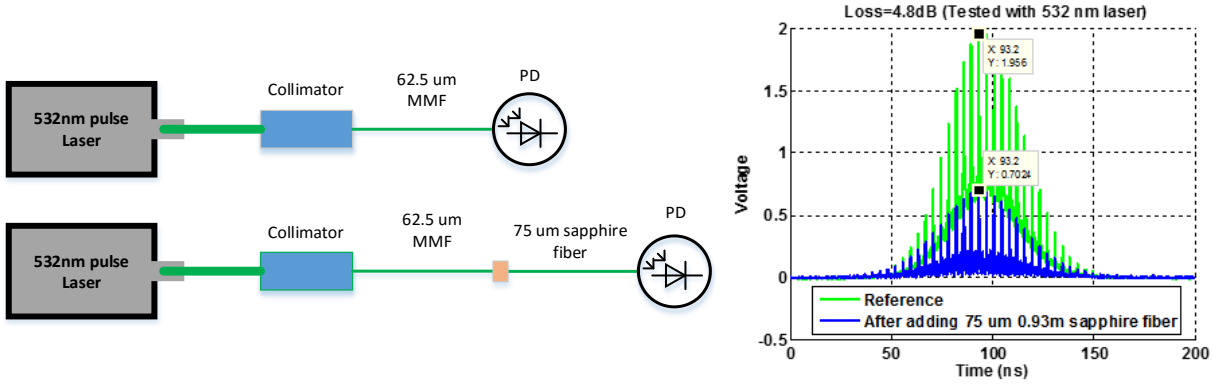

Figure 3-13. Sapphire fiber loss measurement with a Nd: YAG light source and a photodiode.

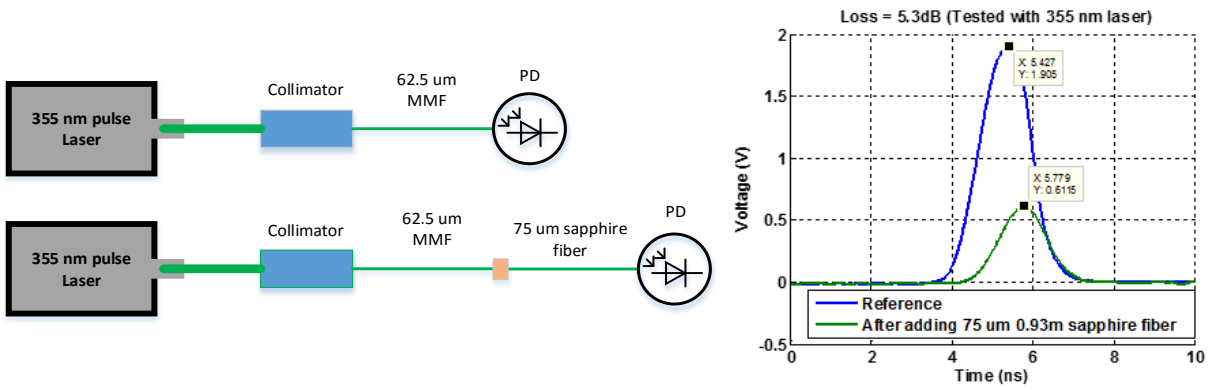

Figure 3-14. Sapphire fiber loss measurement with a 355nm pulsed laser and a photodiode.

As a summary, taking the intensity of thermal radiation, fluorescence, attenuation of the sapphire fiber, Raman gain and quantum efficiency into consideration, a laser wavelength of 532 nm is a good candidate for sapphire fiber-based Raman DTS system. Other candidate wavelengths are from 700 nm to 900 nm.

3.5.3 Numerical aperture of sapphire fiber

The numerical aperture (NA) of an optical fiber determines the maximum angle at which the fiber can accept or emit the light. A smaller NA can reduce the pulse broadening and improve the achievable spatial resolution which has been discussed in details in Section 3.2.1. Therefore, an accurate and reliable measurement of NA is important to the performance estimation of sapphire fiber-based Raman DTS system. The NA was measured with three common methods, including the beam profiler projection method, linear scan method, and angular scan method, as shown in Figure 3-15. The angular scan method has been approved as the standard measurement method and test procedure of Telecommunications Industry Association (TIA) for numerical aperture since 2003. A summary of the TIA standard apparatus is as follows:

1) Far field:
2) Light source: variation <10%.
3) Light source: wavelength band <100 nm HWHM.

4) Light source: wavelength at 850nm+-25 nm if not specified. The NA at another wavelength can be derived by multiplying a constant. For example, the constant is 0.95 for 540 nm and 0.96 for 633 nm.
5) Cladding mode stripper: fiber coating is sufficient, if there is no coating, cladding mode stripper is needed at both end of the specimen.
6) Optical detector: linear response with 5% over the range of intensity encountered
7) Optical detector: A pinhole aperture may be used to restrict the effective size of the detector in order to achieve increased resolution.
8) The specimen shall be a representative sample of fiber 2.0 m ± 0.2 m in length.
9) A resolution of ±0.5° is typically used.

The light source in the following experiment is a superluminescent diode (Superlum, Broadlighter S840) at 849.3 nm, which was a test wavelength suggested by the Telecommunications Industry Association. The light is firstly collimated into a parallel light and then coupled by an objective lens whose NA is 0.66. The large NA objective lens couples the laser light into the fiber with a full-fill angle so that all modes are also equally excited.

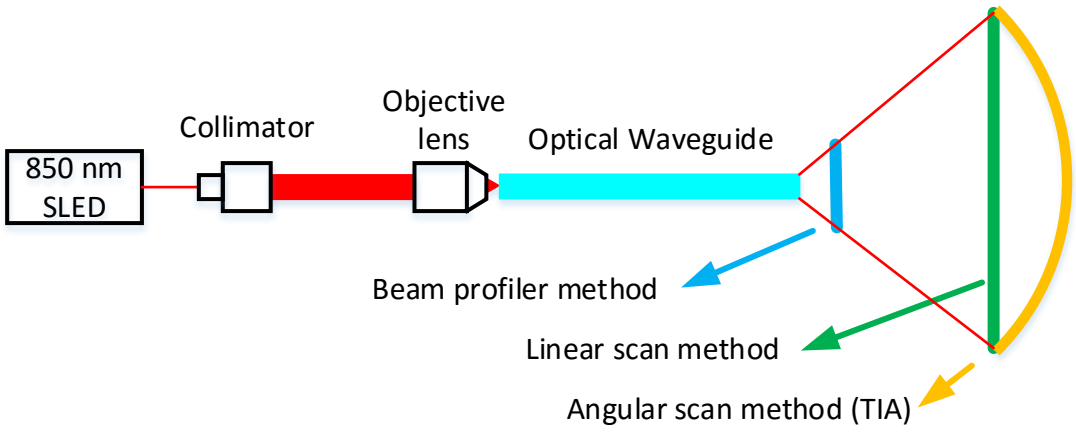

Figure 3-15. Methods of measuring numerical aperture of a waveguide.

In the beam profiler method, the beam profiler, used as the optical detector, measured the 2D distribution of the output light via two single measurements to calculate the NA. Conversely, the

linear scan method measures the output light intensity along a straight line with a photodetector (PD) and via an angular curve via the angular scan method.

The NA of single mode fiber (SMF) was measured with the beam profiler method and angular scan method, as shown in Figure 3-16. Both measurement methods yield the same *NA* result of 0.14 and were unperturbed upon fiber bending and disruption.

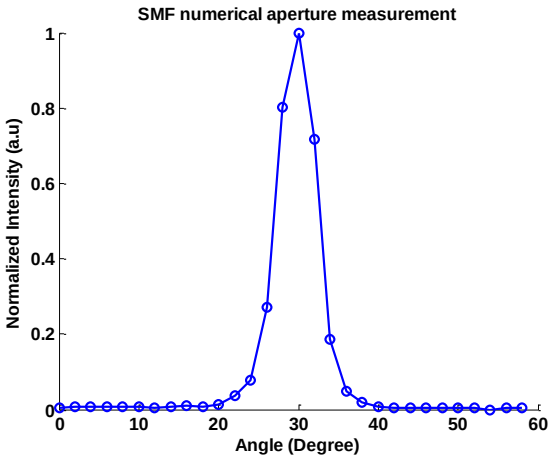

Figure 3-16. NA measurement result of single mode fiber using angular scan method

Conversely, the NA yielded from beam profiler results on multimode fiber are not consistent, as shown in Figure 3-17. The testing fiber is a 2-meters long, 50/125 μm step-index MMF. Group 1 (G1) to group 4 (G4) are measured at different bending conditions. The result varies from 0.16 to 0.215 due to two reasons. The first one is due to the intermodal coupling. A tiny bending difference to the fiber will dramatically change the far field pattern. As a result, the fiber under test (FUT) has to be isolated from vibration to remain the same coupling condition over the time of testing. Any change in output intensity pattern will lead to a different NA value. Furthermore, the distance from the sensing surface of the beam profiler to the fiber end face also affects the output light intensity pattern. Although the beam profiler method is simple and convenient, it is only suitable for low NA (<0.15) fiber, therefore, the other two methods are recommended for high NA (>0.15) fiber.

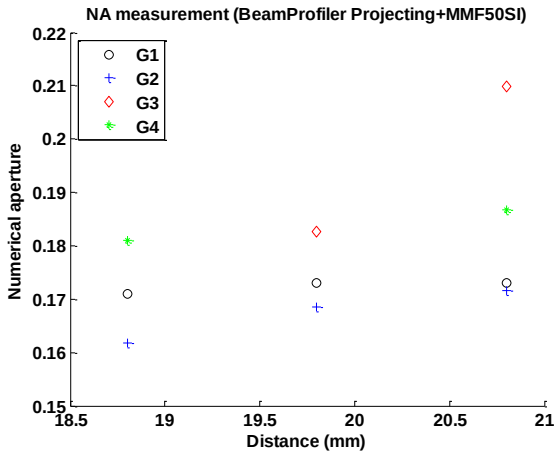

Figure 3-17. NA measurement results based on beam profiler projecting method in a step-index MMF

The light source and FUT used in the linear scan method were the same as the one used for beam profiler method. The photodetector (Thorlabs, PDA36A) was installed onto a 2D translation stage which allows for motion in two directions, parallel and perpendicular to the fiber end face. The scanning area is a rectangular shape (Figure 3-18 (a)) and the measured 2-D intensity map is shown in Figure 3-18 (b).

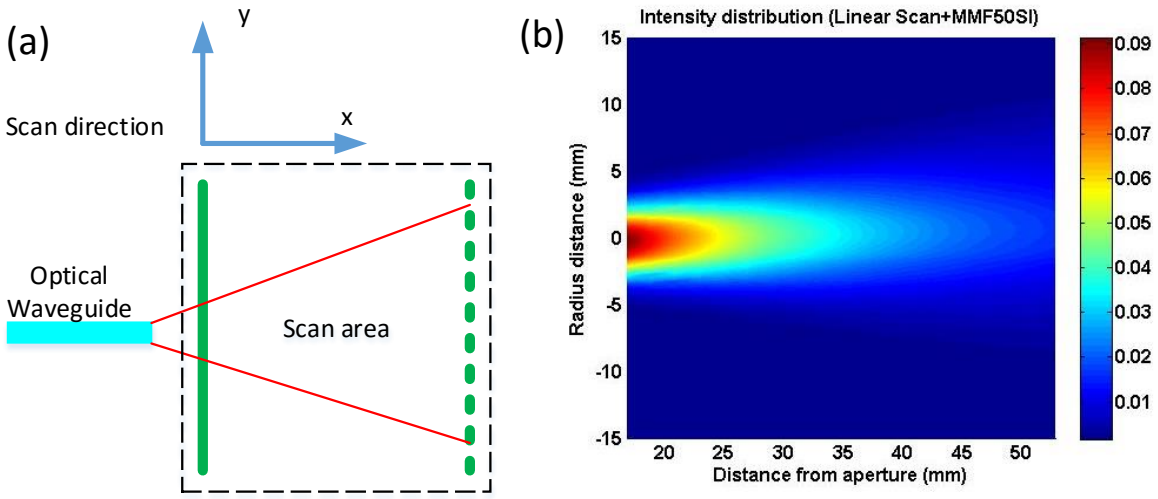

Figure 3-18. Illustration of NA measurement based on linear scan method

The NA of the fiber which is defined as the half of the 5% intensity angle can be calculated along the x-axis, based on the 2D intensity distribution along x-axis. The calculated NA from linear scan

method result is shown in Figure 3-19. The calculated NA reduces gradually the PD is moved away from the fiber end face and approaches to a constant value of 0.189.

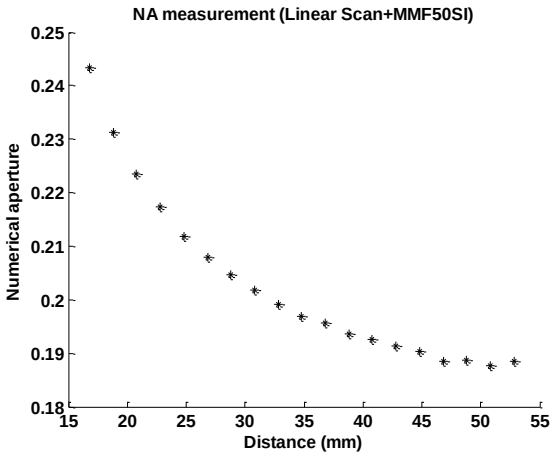

Figure 3-19. NA measurement result of linear scan method with a Step-index MMF

As shown in Figure 3-20(a), the angular scan method scans the output light intensity along an angular curve in the y-direction. By measuring the angular curve light intensity, the 2D map of the output light intensity of a 50/125μm step-index MMF is shown in Figure 3-20(b).

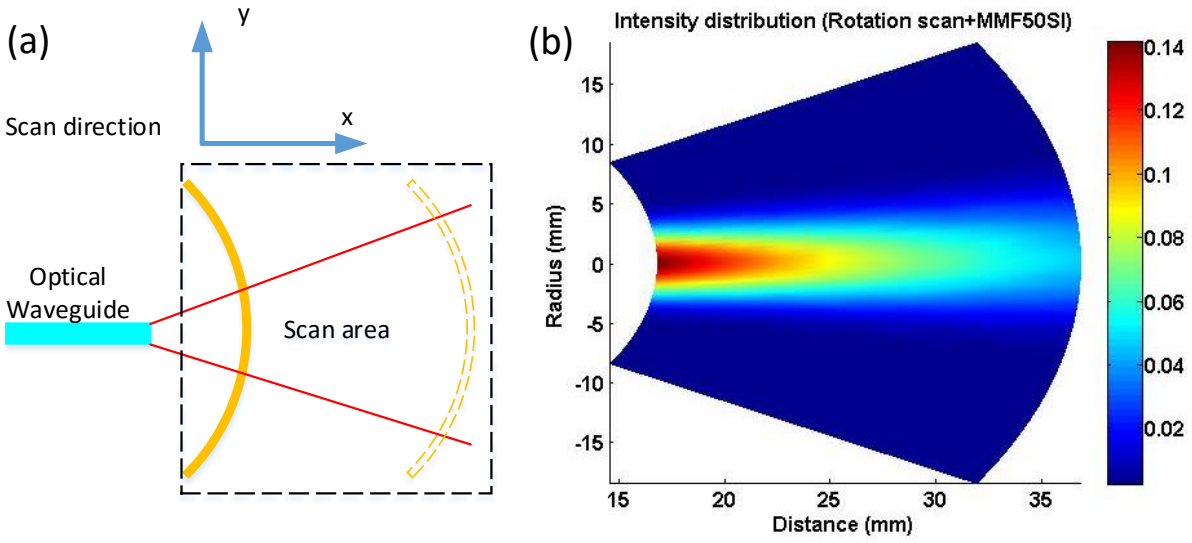

Figure 3-20. Illustration of NA measurement based on angular scan method

In an effort to test the stability of this method, the fiber was randomly disturbed with slightly different bending conditions and the measurement was conducted three times. As shown in Figure 3-21 the NA measurement result of a 50/125 μm step-index MMF is consistent and irrespective of the bending condition. The NA measurement result approaches a value of 0.203 and was larger than those obtained from linear scan method although the variation is less than 7%. It is noted that the linear scan method is more commonly used in practice because of the simple setup.

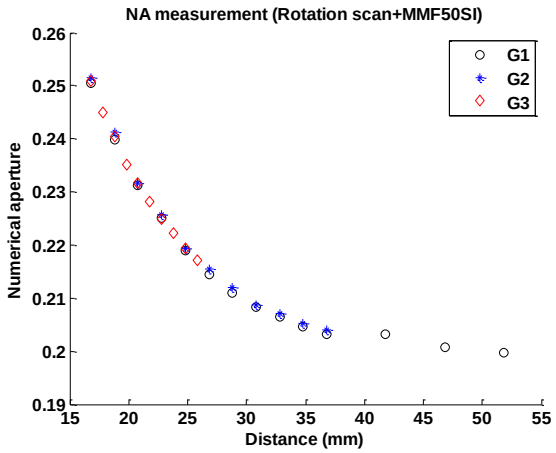

Figure 3-21. NA measurement results based on angular scan method

The NA of a 0.9 m long, OD 75 μm sapphire fiber was tested via the angular scan method. The output intensity in the far field is shown in
Figure 3-22. The calculated NA is 0.1547. So the NA at 532 nm is approximately 0.1470. Since the sapphire fiber was protected in a ceramic tube, the maximum NA may be reduced due to the surface scattering.

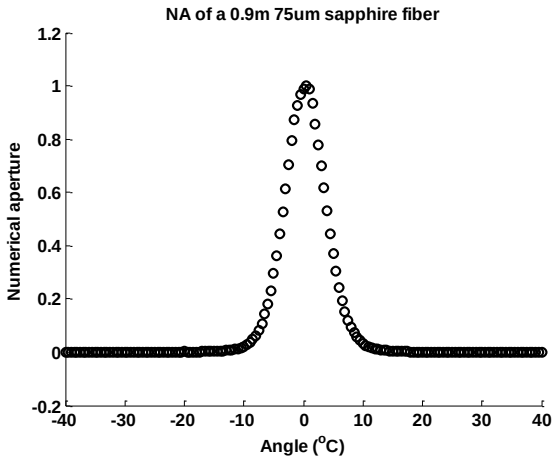

Figure 3-22. The NA measurement of sapphire fiber at 850 nm based on angular scan method

3.6 Optical coupling

The lens used to couple light into sapphire is critical because the backward Raman scattering light will be captured and collimated by the same lens. When coupling the pump light into the sapphire fiber, a long focus length is preferred to match the *NA* of sapphire fiber. When coupling the backward Raman scattering light into the photodetector, a short focus length is preferred so that the backward beam size will not exceed the aperture of the lens as shown in Figure 3-23.

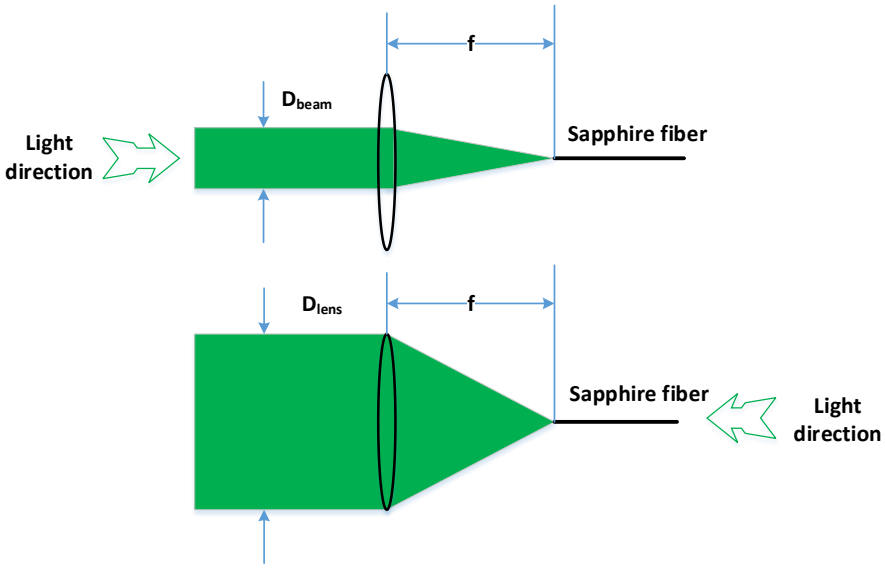

Figure 3-23. Analysis of *NA* requirement of coupling lens

Therefore, the relationship between the *NA* of the beam coupling in and out of the fiber should meet the following two requirements:

$$\mathrm{NA}_{in} = \sin(\arctan\frac{D_{beam}}{2f}) < \mathrm{NA}_{sapphire} \quad \textbf{(3-12)}$$

$$\mathrm{NA}_{out} = \sin(\arctan\frac{D_{lens}}{2f}) > \mathrm{NA}_{sapphire} \quad \textbf{(3-13)}$$

where NA_{in} and NA_{out} correspond to the NA of the beam coupling in and out of the fiber, $NA_{sapphire}$ is the equivalent NA of sapphire fiber, D_{beam} and D_{lens} are the diameters of the laser beam and the lens aperture, and f is the focal length of the lens.

From this two equations, we have

$$\frac{D_{beam}}{2\tan\left[\arcsin(\mathrm{NA}_{sapphire})\right]} \le f \le \frac{D_{lens}}{2\tan\left[\arcsin(\mathrm{NA}_{sapphire})\right]} \quad \textbf{(3-14)}$$

Using the parameters of our current system, the optimized focal length for coupling the light into the fiber should be within the range of 15.5mm-37.6mm. Subsequently, a 38mm lens was chosen to acquire best coupling efficiency for the current system.

4 SAPPHIRE FIBER-BASED RDTS SYSTEM

The design of the Raman DTS system has been discussed in detail in Chapter 3. This chapter presents the preparation and results of the Raman DTS system in sapphire fiber. This novel sapphire fiber-based Raman DTS system has been proven to a temperature of 1400ºC with a standard deviation of several degrees. This advance would potentially open up a wide range of industrial applications.

This chapter is organized as follows. Section 4.1 introduces the fabrication procedures of sapphire fiber pigtail and patch cord and some important experiences regarding identifying the damage of the sapphire fiber. Section 4.2 shows the observation of temperature dependence of the Raman spectrum in sapphire fiber. In particular, the Anti-Stokes signal in a sapphire fiber is reported for the first time. Subsequently, the feasibility of the sapphire fiber-based Raman DTS system is demonstrated in Section 4.3. Section 4.4 address issues and concerns.

4.1 Experience regarding sapphire fiber

4.1.1 Fabrication of sapphire fiber pigtail and patch cord

Sapphire fibers are well suited for harsh environments due to the high-temperature melting point (~2054ºC). They are immune to electromagnetic interference, oxidation, and most chemical attack. Very high quality and low loss sapphire fiber has been manufactured with the laser-heated pedestal-growth method[68]. Tremendous efforts have been focused on sapphire fiber cladding to optically isolate these fibers in industrial high-temperature environments, such as those made through the sol-gel method[69] and formation of nanometer scale cavities on the sapphire fiber surface with hydrogen ion implantation[70]. Unfortunately, so far, the success of these explorations is rather limited because the cladding brings significant attenuation. Sapphire fiber connections are another concern that needs to be addressed. No standard method has been developed to splice a sapphire fiber to a normal silica fiber due to their large difference coefficient of thermal expansion (CTE). Zhu[71] successful developed a method to connect a sapphire fiber with a multi-mode silica fiber. However, this method requires a lot of labor work and professional

training. Furthermore, this connection is permanent and any mistake will ruin the whole complicated process.

In this section, a simple method of making sapphire fiber pigtail and patch cord is presented. This effort makes it much easier to connect sapphire fiber with any other type of fibers. This connection is removable and exchangeable with minimum loss. The second part of this section shares a useful experience dealing with the damage of sapphire fiber.

Figure 4-1 shows the finished sapphire fiber pigtails. The diameter of sapphire fiber is 75 µm or 122 µm. The internal diameters of the ferrule are 80 µm and 128 µm (140µm), respectively. The ferrules can be angled physical contact (FC/APC) or flat face physical contact (FC/PC). These ferrules and empty connectors are commonly used for silica fiber. The bonding material is "Phenyl salicylate", as shown in Figure 4-2. Its melting point is 41.5ºC. When the fiber end face was damaged by the laser and require polishing or repairing, this pigtail can be easily dissembled by heating the ferrule.

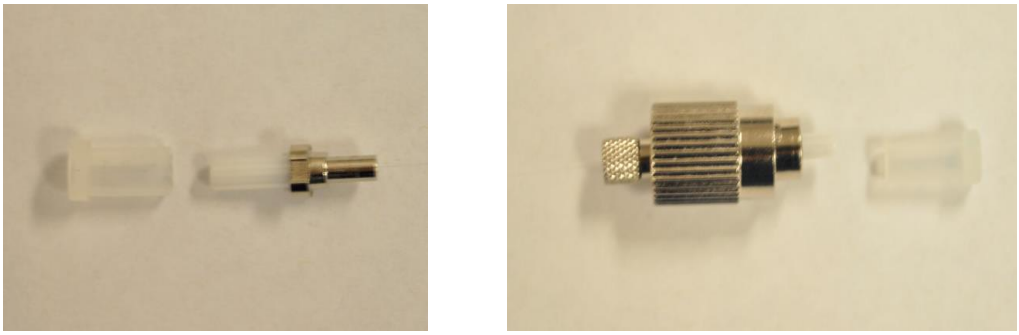

Figure 4-1. Sapphire fiber ferrule (left) and sapphire fiber FC/PC connector (right)

Figure 4-2. Bonding material for sapphire fiber pigtail

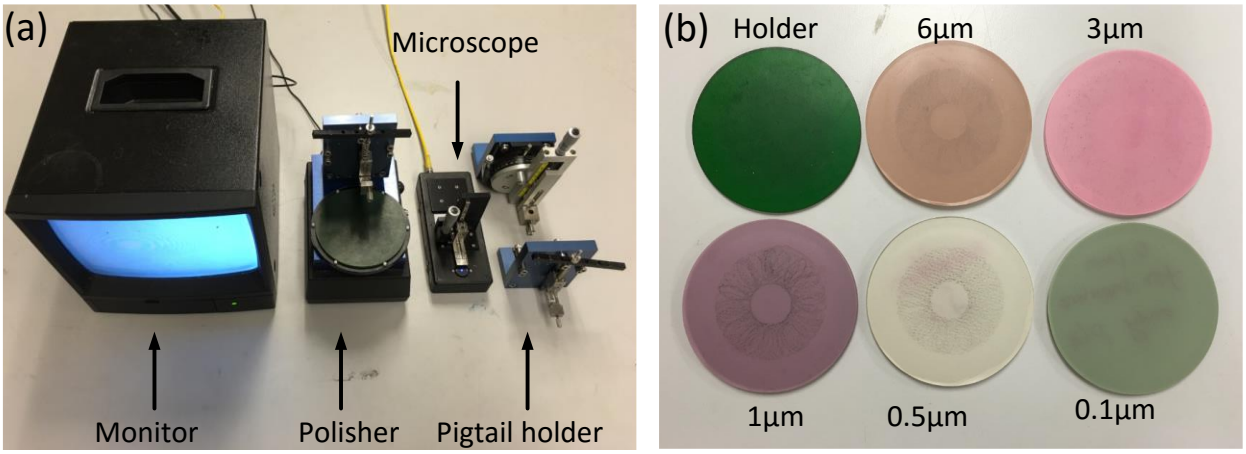

Figure 4-3. (a) Connector Polisher system; (b) Polish film

The procedure is as follows,

1) Clean the sapphire fiber with acetone;
2) Clean the sapphire fiber with alcohol;
3) Insert the sapphire fiber through the ferrule or empty connector and reach out about 0.5~2 mm sapphire fiber from the ferrule head;
4) Heat Phenyl salicylate in a ventilated environment until melting;
5) Drop tiny amount liquid phenyl salicylate on the sapphire fiber extending from the ferrule;

6) Add tiny grain of solid phenyl salicylate as nuclei of crystallization to the bonding position to speed up the crystallization process which usually takes about 30 seconds;
7) Polish the bonding material with 30 μm polish film until the sapphire fiber is reached;
8) Mount the ferrule or connector in the fiber pigtail polish machine (KrellTech, SpecPro™ Connector Polisher) as shown in Figure 4-3 (a);
9) Polish the ferrule or connector with the polish film of 6 μm, 3 μm, 1 μm, 0.5 μm and 0.1 μm step by step as shown in Figure 4-3 (b).
10) Clean and observe the fiber end face at each step before moving to the next step;
11) Finally clean the fiber end face with alcohol very carefully and keep the sapphire fiber pigtail in a safe place. A typical accomplished sapphire fiber pigtail is shown in Figure 4-4.

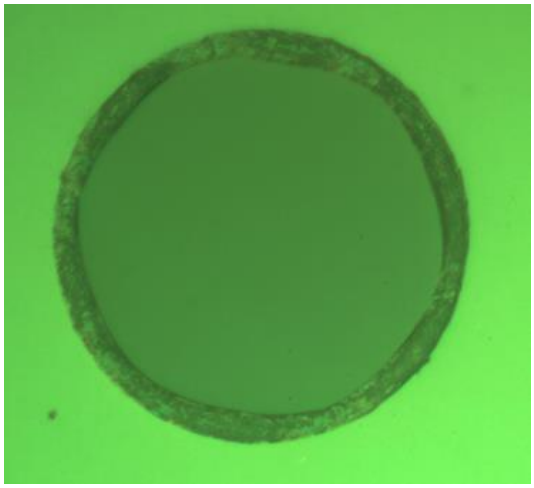

Figure 4-4. Typical sapphire fiber pigtail end face

If the end face of the sapphire fiber pigtail was damaged and the damage depth was not deep, the pigtail could be repaired by polishing with 0.5 μm and 0.1 μm film. If the damage depth was deep, the depth was usually less than 2 mm. The sapphire fiber pigtail then requires disassembly and the process must be redone.

4.1.2 Damage identification of sapphire fiber end face

When the laser power is sufficiently high, the chance of damage to the sapphire fiber end face is high. This may happen in the alignment process or due to the instability of the laser power. Contamination or dust attached to the fiber end face may cause damage as well. When the laser power is too high, the damage is obvious and can be observed with a "Fiber Inspection Scope" (Thorlabs, FS200-FC). A typical damaged sapphire surface and its cross section view are shown in Figure 4-5.

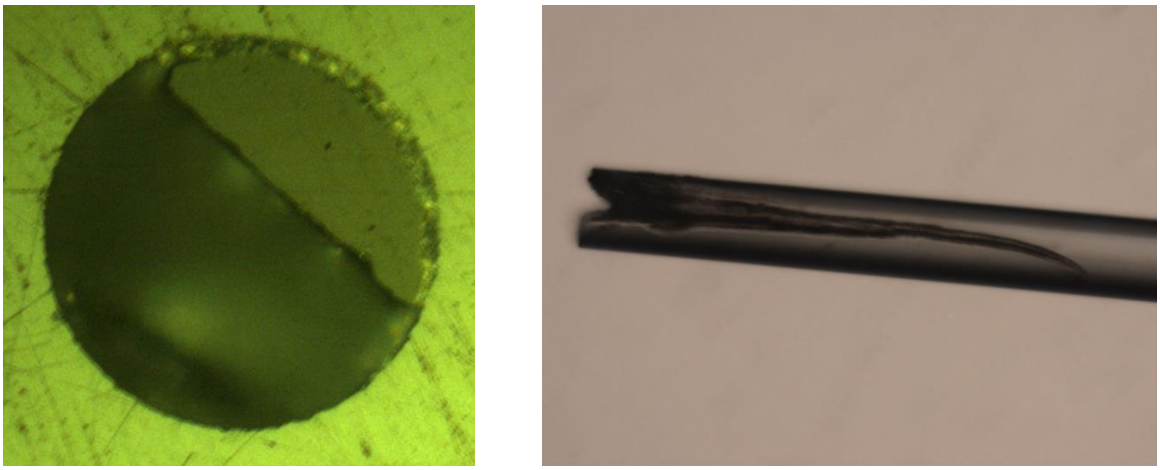

Figure 4-5. Damaged sapphire fiber surface

Figure 4-6 shows the attenuation comparison of a sapphire fiber before and after a damaged fiber end face is repaired. The measuring procedure is consistent as seen in Figure 3-12.

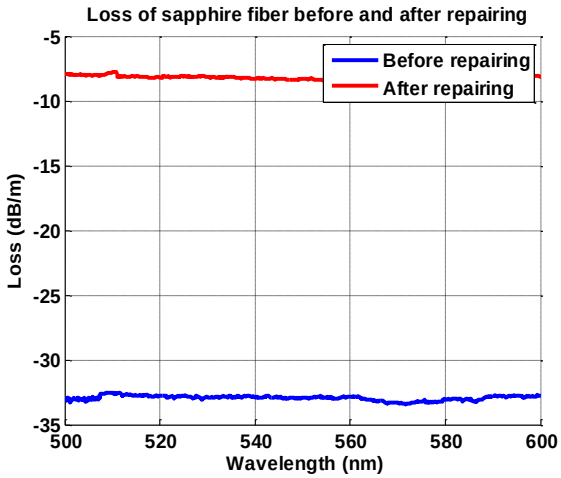

Figure 4-6. Attenuation comparison of sapphire fiber before and after repairing

However, in most cases, the fiber surface seems fine even under the observation of the “Fiber Inspection Scope”. The damage to the fiber surface happens more often with a picosecond laser. We can follow the process shown in Figure 3-12 to determine the attenuation. However, this method is time-consuming and it is also risky of fiber breakage. We found an easier way to identify the damage of the sapphire fiber: by emitting a small amount of light from one end of the sapphire fiber, we are able to observe a bright sapphire end face from the other end. If the fiber end is damaged, the end face is not uniform while a good fiber shows a bright and uniform hexagonal shape as shown in Figure 4-7.

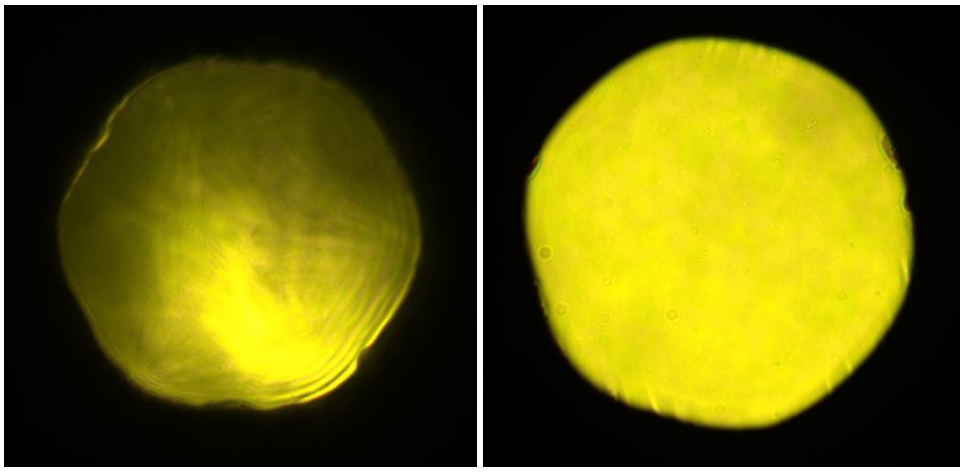

Figure 4-7. Observation of hidden damage of sapphire fiber (left); Observation of good sapphire fiber (right)

If the fiber suffers “invisible” damage shown in Figure 4-7, the transmission attenuation at long wavelengths does not change but at visible wavelengths, the attenuation increases significantly. This happens on sapphire fibers made by the LHPG method and Edge-defined film-fed growth (EDFG) method. In both cases, the sapphire fiber has to be cut by several millimeters to remove the damage part.

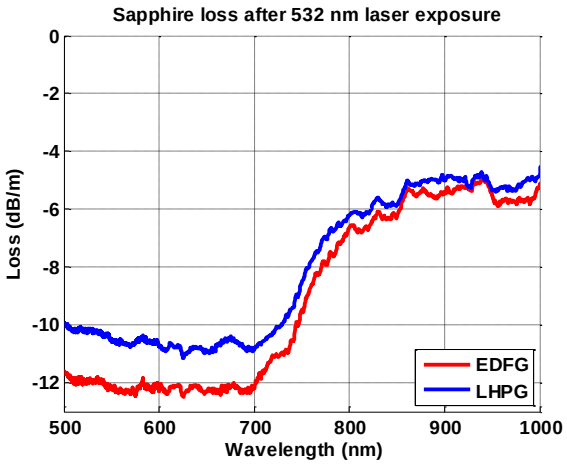

Figure 4-8. Transmission measurement of a damaged sapphire fiber spectrum

4.1.3 Sapphire fiber annealing

Annealing is a process of slow heating and slow cooling of a material in order to remove internal stress. The temperature depends on the material and its condition. This process can improve the long-term stability of Fiber-Bragg-Grating(FBG) in silica fiber, especially the one made by a femtosecond laser[72]. It can also reduce the loss of sapphire fiber[68]. Before the experiment, the sapphire fiber was kept constant at 1022ºC for 10 hours to remove any organic deposition and release the stresses frozen in the fiber. Figure 4-9 shows the temperature in the annealing process.

The transmission power indicates the relative attenuation of the fiber. Since the bandwidth of the PD 2 (shown in Figure 4-24) was less than 10 MHz, the transmitted laser pulse signal was broadened. In Figure 4-9, it shows that the transmission power increased by 30% which means that the fiber loss was reduced by 30% after canceling the laser intensity fluctuation.

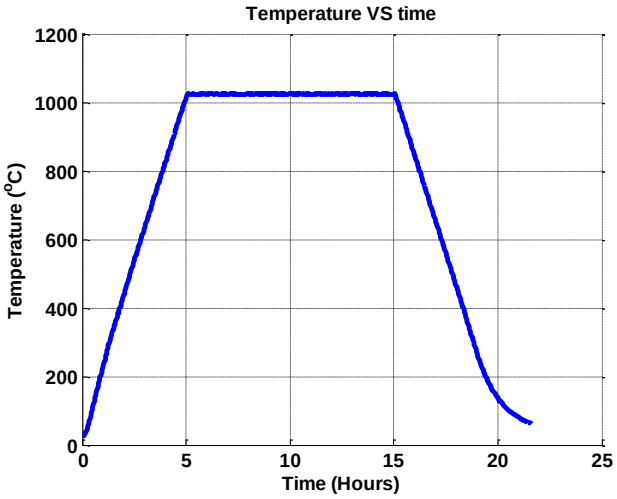

Figure 4-9. Single crystal sapphire fiber annealing process

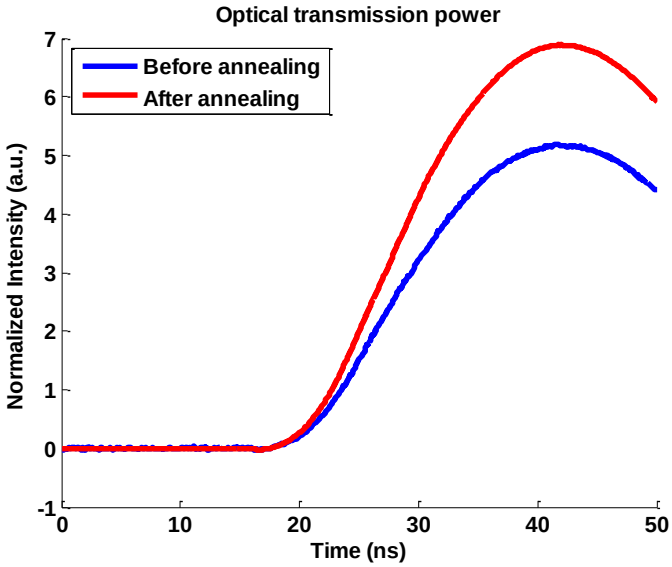

Figure 4-10. Optical transmission power comparison before and after annealing

4.2 Temperature dependence of sapphire fiber Raman scattering

4.2.1 Test setup

As stated in the previous section, few have reported the observation of Raman Anti-Stokes in sapphire fiber. So our first step is to excite Anti-Stokes signal in sapphire fiber and learn its characteristics. The experimental setup is shown in Figure 4-11. A Nd:YAG laser (Continuum, SLIII-10) at 532 nm was used to excite the Raman scattering with a pulse repetition rate of 10 Hz. Each pulse's energy was about 500 µJ. The pulse width (FWHM) was about 24 ns. The laser pulse in the time domain is shown in Figure 4-12.

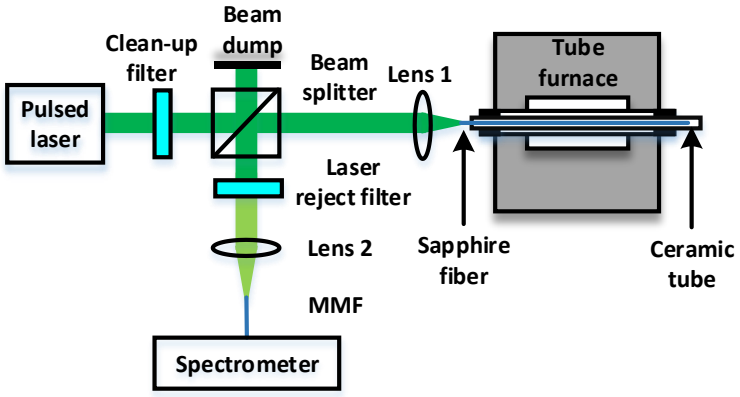

Figure 4-11. Schematic of the experimental setup for Raman scattering detection

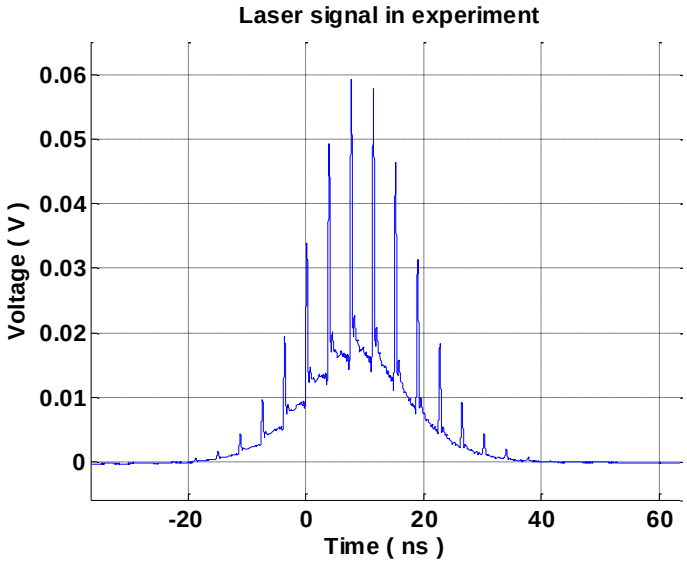

Figure 4-12. Laser pulse of the Nd:YAG laser (Continuum, SLIII-10) at 532 nm

Since the Raman signal is very weak, any noisy background propagating with the laser may mask the real Raman signal. A narrow band pass filter (Edmund, #68-843) was used to remove the laser noise background. Figure 4-13 shows the sapphire fiber Raman spectrum with and without the filter. After passing a 50:50 beam splitter, the laser light was then coupled into a 0.72 m long, 75 μm-diameter sapphire fiber using a concave lens with focal length of 38 mm. The sapphire fiber was made by the laser heated pedestal growth method[68] from Micromaterials Inc. The sapphire fiber was protected in an open-ended ceramic tube (with inner diameter 1.6 mm and outer diameter 6.75 mm). A K-type thermocouple was protected in another ceramic tube to monitor the temperature distribution. These two ceramic tubes had the same size and length and were located close to each other so that the thermocouple reading could better reflect the temperature along the sapphire fiber. The backward Raman scattering light was separated by the same beam splitter and passed through a notch filter at a center wavelength of 532 nm. This notch filter served as the laser/Rayleigh reject filter. It blocked all reflections from the first sapphire fiber end face as well. The backward scattering light was last coupled into a 105μm-diameter core multi-mode fiber by a concave lens with focal length of 50 mm. The detector was a spectrometer (Ocean Optics, USB4000) whose working wavelength range was from 350 nm to 1050 nm.

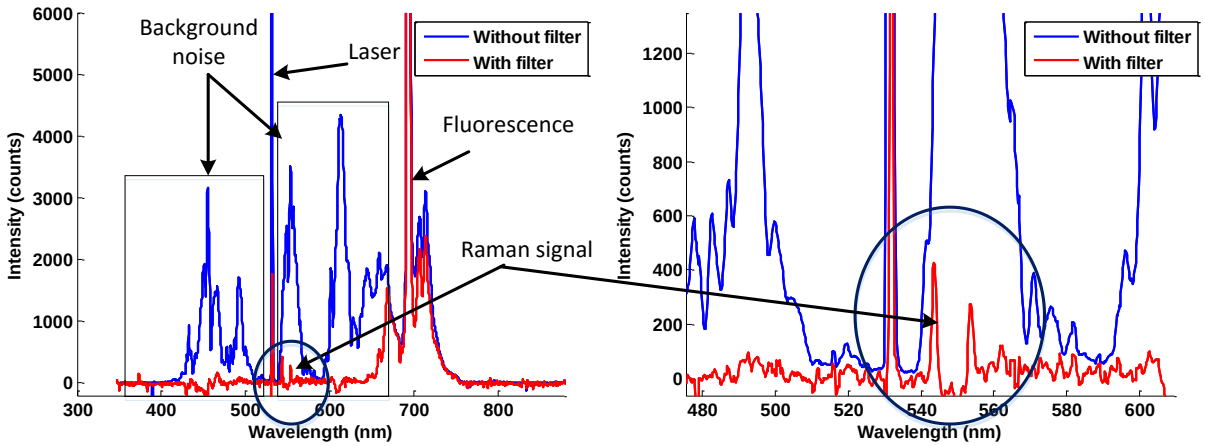

Figure 4-13. The Raman spectrum of sapphire fiber with and without the laser clean-up filter

The temperature distribution measured by the K-type thermocouple is shown in Figure 4-14. The temperature profile shows a maximum temperature point in the furnace center and cooling gradually toward the ends of the tube furnace. The heating rate of the furnace was 10 ºC/min,

and the temperature was kept constant during the measurements within ±1 ºC. The temperature steps were set as 300ºC, 500ºC, 700ºC, 900ºC, and 1100ºC. Each measurement was taken after the temperature was maintained for at least 30 minutes. The maximum temperatures measured by a thermocouple at these steps were 300ºC, 497ºC, 680ºC, 858ºC, and 1033ºC. The differences between the set temperatures and external measurement results were normal due to the customized scaling.

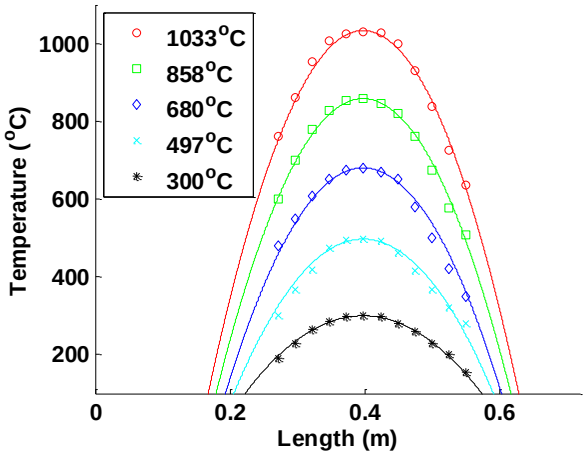

Figure 4-14. Temperature distribution along the sapphire fiber.

Sapphire crystal Raman peaks are represented by 7 modes [15, 63] at 379, 418, 431, 450, 578, 645 and 750 cm^{-1}, in particular, 418, 578 and 750 cm^{-1} are the main peaks[73]. In sapphire fiber, optical modes at 418, 431, 450, 578 and 750 cm^{-1} are expected when the pump light is propagating perpendicular to the C-plane[15]. We distinguished 418, 578 and 750 cm^{-1} Stokes components in sapphire fiber. The experimental result is shown in Figure 4-15. Thirty measurements, each with an integration time of 10 seconds, were averaged in each plot. Each data point in the spectrum was smoothened by adding two blue-shift points and two red-shift points to remove the unwanted noise. Strong fluorescence in the sapphire fiber was observed at 694.3 nm with a wide wing extending to the Raman Stokes wavelength. The fluorescence became strongest at 300ºC. The blackbody radiation intensity was mixed with fluorescence and Raman signals. Figure 4-16 shows the zoomed-in view of the sapphire fiber Raman signal with the thermal background and fluorescence background. The positions of Raman Stokes and Anti-Stokes signals are symmetric in the wavenumber domain which is consistent with the theory.

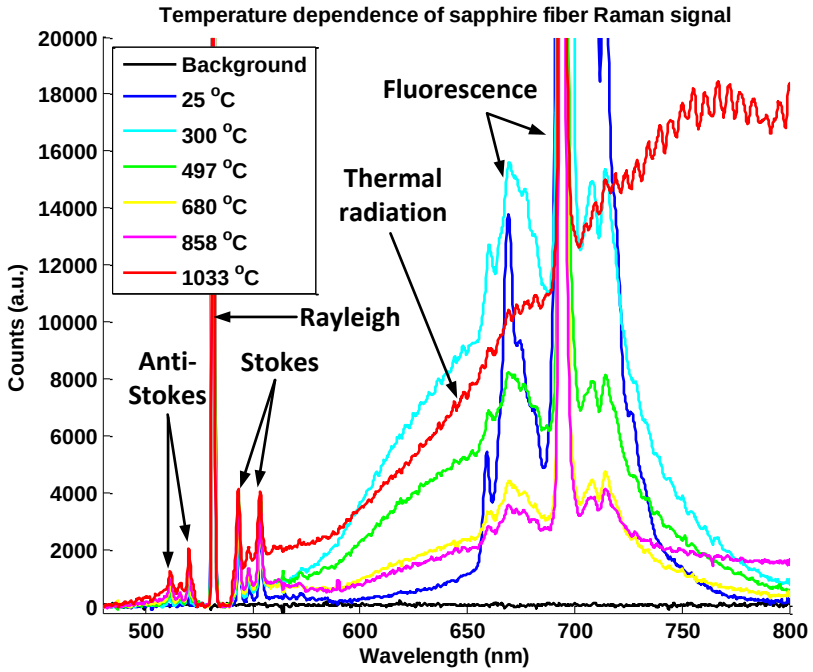

Figure 4-15. Sapphire fiber Raman spectrum and fluorescence at different temperatures

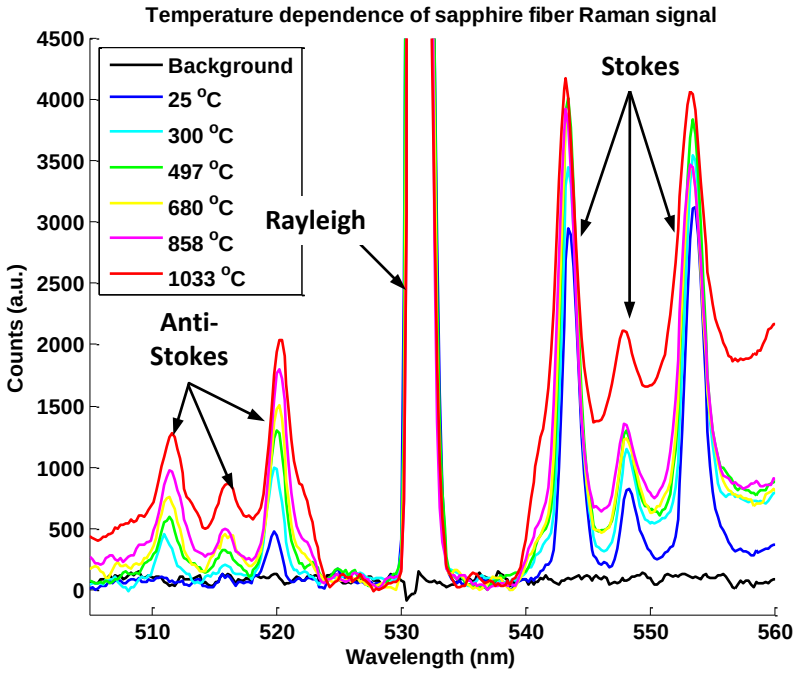

Figure 4-16. Raman spectrum of sapphire fiber at elevated temperature

4.2.2 Signal processing and analysis

In an effort to remove the thermal radiation background, a dark spectrum was immediately measured before recording the Raman spectrum by blocking the light path into the spectrometer. This background is shown in Figure 4-17. It shows that the thermal radiation background became intensive only at temperatures higher than 1000ºC. The periodic ripples at 1033ºC were due to the interference generated from the two surfaces of the laser rejection filter. The valley between 520 nm and 540 nm was due to the laser rejection filter centered at 532 nm. The simulation result of the thermal radiation background is compared with the experimental results which are shown in Figure 4-18.

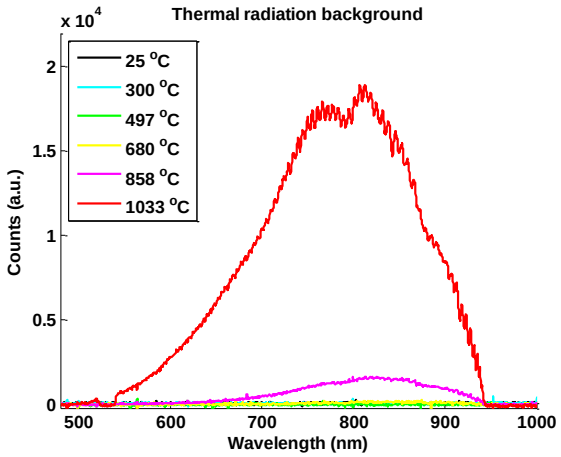

Figure 4-17. Thermal radiation background at elevated temperatures

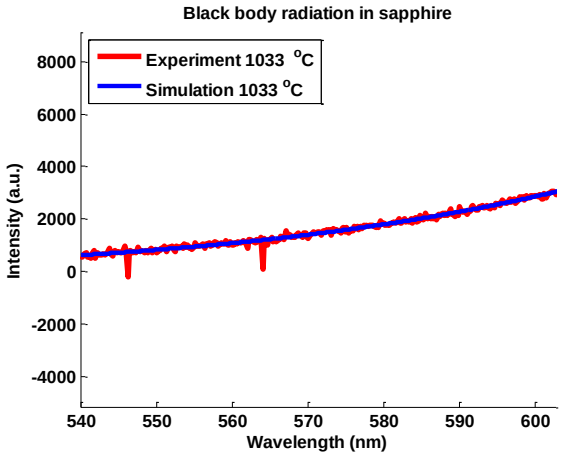

Figure 4-18. Comparison between thermal radiation measurement and theoretical simulation

Figure 4-19 shows the final results of Raman spectrum by subtracting the thermal background from the total spectrum. It indicates that the fluorescence light rarely affects Raman spectrum at room temperature. At elevated temperatures, the fluorescence always coexists with the Raman spectrum.

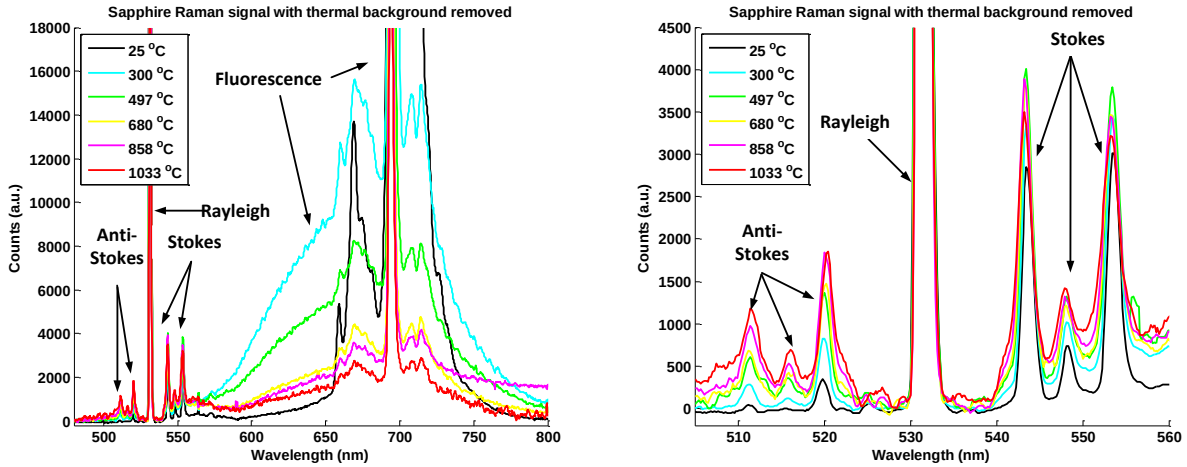

Figure 4-19. Raman spectrum after subtracting thermal radiation background

The detailed signal processing was originally published by the author[38]. In an effort to better predict peak intensity, frequency position and full width at half maximum, the original peak was represented by a Lorentz fitting peak.

Taking the fiber loss and laser power depletion into consideration, the Raman peak intensities are proportional to the integration of differential cross section along the fiber as

$$P_{AS,S} \propto \int_0^L \left. \frac{d\sigma_{AS,S}}{d\Omega} \right|_x \exp\left[-2\int_0^x \alpha(\mathrm{x})\,\mathrm{dx} \right] dx \qquad \textbf{(4-1)}$$

where L is the sapphire fiber's length, and α is the attenuation of the fiber at position x, $\frac{d\sigma_{AS,S}}{d\Omega}$ denote the differential cross section of Raman Anti-Stokes or Stokes, $P_{AS,S}$ denotes the receiving power of Anti-Stokes or Stokes in arbitrary units.

Figure 4-20 shows the temperature dependence of sapphire Raman intensity from room temperature to 1033ºC. The peak intensities were normalized at their values at 300ºC. The solid curves are the theoretical predictions. The points with error bar are the experimental results. It indicates that the Anti-Stokes signals are more sensitive to temperature than Stokes which is consistent with the theory predicted by Equations (2-3) and (2-4). Since the Stokes signal has the stronger intensity and higher signal to noise ratio, the standard deviation is smaller than that of Anti-Stokes signals.

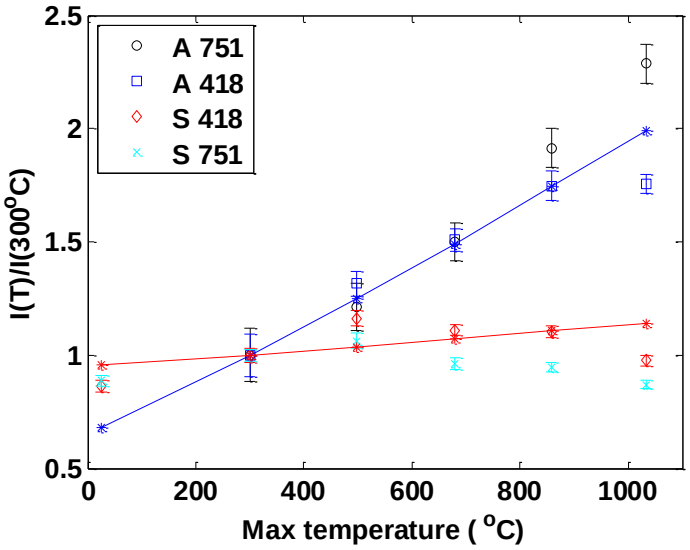

Figure 4-20. Temperature dependence of sapphire Raman intensity

The mismatch between the theoretical prediction and experimental result most likely comes from the interference of fluorescence background centered at 694.3 nm with a broad side lob extending into the Stokes peak and Anti-Stokes region, reaching its maximum at 300 ºC. The fluorescence peak and its broad side lobe gradually decreased at a higher temperature and almost diminished above 1000 ºC. The Anti-Stokes peaks are less affected by the fluorescence background than Stokes peaks since Anti-Stokes are further away from the fluorescence center. Alois Schauer[74] reported the temperature dependence of Raman Stokes frequencies in sapphire and concluded that thermal expansion of the lattice was the reason for this dependence. In Figure 4-21, for the first time, we reported the temperature dependence of the Raman frequency shift of both Anti-Stokes and Stokes peaks. The frequency shifts were normalized to their value at room

temperature. The shift of the Stokes and Anti-Stokes peaks are symmetric in wavenumber domain which can be derived from the phase matching condition of Raman scattering or Equations (2-1) and (2-2). Both Stokes and Anti-Stokes peaks tend to shift toward excitation wavelength at a higher temperature. The frequency shifts are very small. For example, the peak position of Stokes signal at 751 cm^{-1} is less than 0.5 ns when the excitation wavelength is at 532 nm.

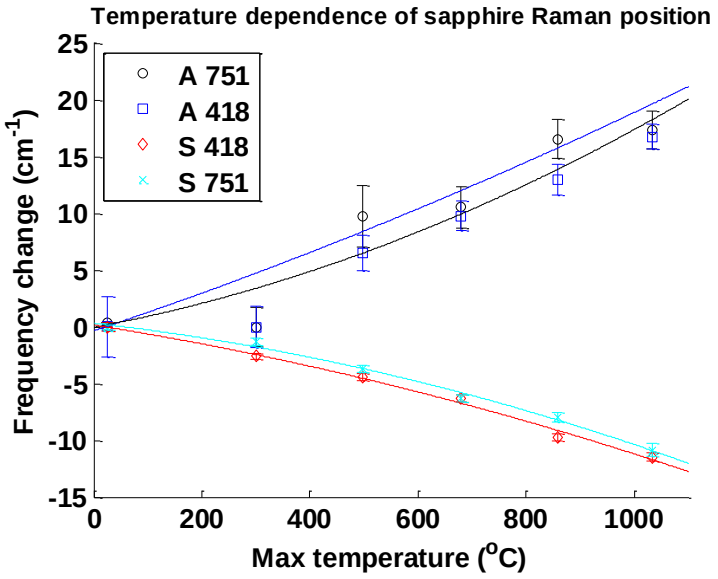

Figure 4-21. Temperature dependence of sapphire Raman frequency

The temperature dependence of Raman peak width in sapphire fiber for both Anti-Stokes and Stokes signals is also observed for the first time as shown in Figure 4-22. Since some peaks are too weak to determine the accurate width, only strong peaks (Stokes 751 cm^{-1}, Stokes 418 cm^{-1}, Anti-Stokes 751 cm^{-1}) are plotted in the figure. Different Raman peaks undergo different rates. The larger Raman shifts broaden faster than the smaller ones. Klemens[75] and M. Ashkin[21] explained this Raman linewidth expansion by the perturbation theory. Reasons for this broadening should take the whole fiber into consideration. Since only part of the sapphire fiber was heated, one side of the Peak remains unshifted while the other side of the peak shifted due to the elevated temperature. This phenomenon can be potentially used for temperature sensing due to some advantages, in particular, this method is independent of fiber loss, contamination and laser intensity fluctuation.

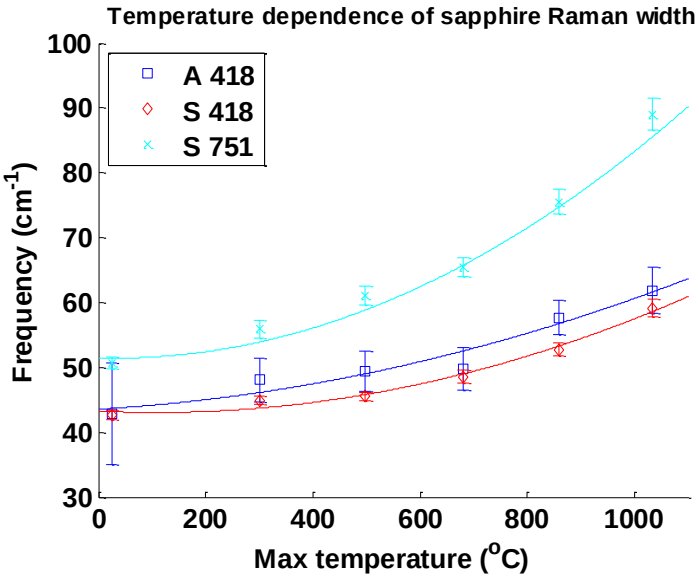

Figure 4-22. Temperature dependent of Sapphire Raman width

Monitoring the Raman frequency shift and peak broadening are two efficient methods for the temperature sensing. Monitoring the Raman intensity in the time domain is appropriate for distributed temperature sensing. Providing the self-calibration characteristic of Raman Anti-Stokes and Stokes ratio, the Raman intensity method is more meaningful.

In this section, for the first time to our knowledge, we experimentally measured the temperature dependence of sapphire Raman line intensity, frequency shift, and linewidth up to 1033 ºC. These experiment results demonstrated that the Anti-Stokes signals are more sensitive to temperature compared to Stokes signals. These experiments also found out the frequency shifts which provided a guidance on selecting the right optical filters. The thermal radiation intensity was at the same level as Stokes signal. These experiments laid a solid foundation for the sapphire fiber-based Raman DTS design and implementation.

4.2.3 Raman intensity comparison between sapphire fiber and silica fiber

The Raman gain of light waveguide depends on material, crystal orientation, and dopant concentration[76]. The Raman gain of single mode fiber is well known. However, the Raman gain of sapphire fiber was never measured before, because the measurement of sapphire fiber

Raman intensity varies with excitation condition, wavelength, fiber diameter, and fiber quality. But we can still estimate the Raman gain of sapphire fiber by comparing the Raman peak intensity with normal silica fiber at the same excitation condition and wavelength for a given sapphire fiber. After the laser power and fiber length, the Raman intensities of a 75 μm core sapphire fiber are normalized, a 50 μm core step-index MMF and a 50 μm core graded-index MMF are compared in Figure 4-23. For clarity, the sapphire fiber signal intensity was multiplied by 10. Assuming the Stokes signal intensity is proportional to the corresponding area, the Stokes signal of graded-index MMF is about 300 times stronger than sapphire fiber and that of step-index MMF is about 30 times stronger than sapphire fiber.

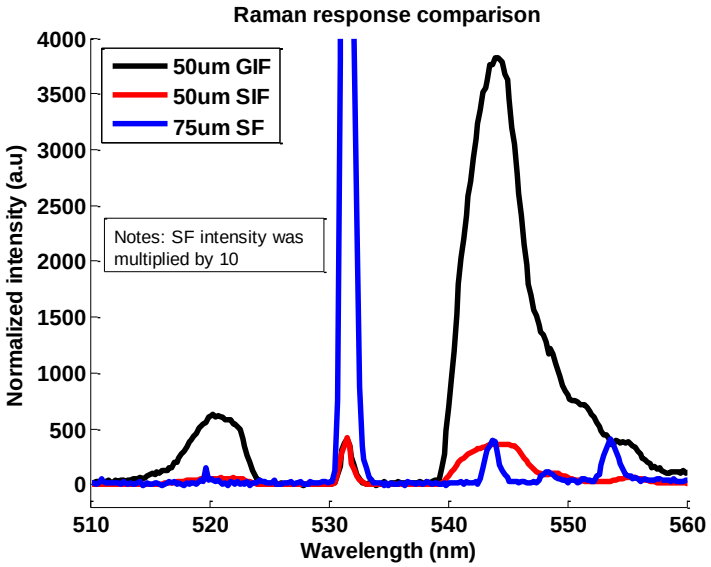

Figure 4-23. Comparison of Raman response among step-index silica fiber, graded-index silica fiber, and sapphire fiber

4.3 Raman DTS system experiments and analysis

4.3.1 System configurations

In this section, the Raman DTS system was tested up to 1400ºC with different lengths of sapphire fiber. The spatial resolution was tested at a maximum temperature of 1400ºC. The simplified Raman DTS system is illustrated in Figure 4-24. The spectrometer was removed from the system

to reduce the system footprint. Two different lasers were used in this experiment. The first one was a diode-pumped solid state laser at 532 nm with 5 ps pulse width (Passat, Compiler) with a peak power of 700 kW. The second was a Passively Q-switched Microchip Laser (Concepts Research Corporation, SPL-532-X-X) at 532 nm. The maximum pulse energy was 5 μJ and the pulse duration time was ~700 ps (from the data sheet). The calculated peak power was ~7 kW which is still far below the SRS threshold of silica fiber (refer to Section 3.3). The sapphire fiber was cleaned with acetone and alcohol and protected in a 36 cm-long, open-ended ceramic tube with an internal diameter of 1.6 mm and an external diameter of 6.75mm. The ceramic tube was inserted into a tube furnace (MTI corporation, GSL1500X) with ambient air as the testing environment. Since the time-resolved Raman signals are independent of the refractive index of the cladding, this system was expected to work in any gas environment. The laser beam firstly passes the "laser cleaning filter" which was usually a very narrow band pass filter. Secondly, the laser beam was separated by the 50:50 beam splitter into two paths, with the upward laser beam monitored by the first photodetector (PD 1) (Thorlabs, SV2-FC) and with another beam focused into the sapphire fiber under test (FUT). The corresponding transmission power was monitored by the second photodetector (Thorlabs, PDA36A). The backward Raman scattering power was split by the dichroic beam splitter (Semrock, FF535-SDi01-25x36) into the Stokes signal and Anti-Stokes which were monitored by two identical Avalanche photodetectors (Thorlabs, APD210). All photodetectors were analyzed by a high-speed oscilloscope (Lecroy, WavePro7 Zi-A).

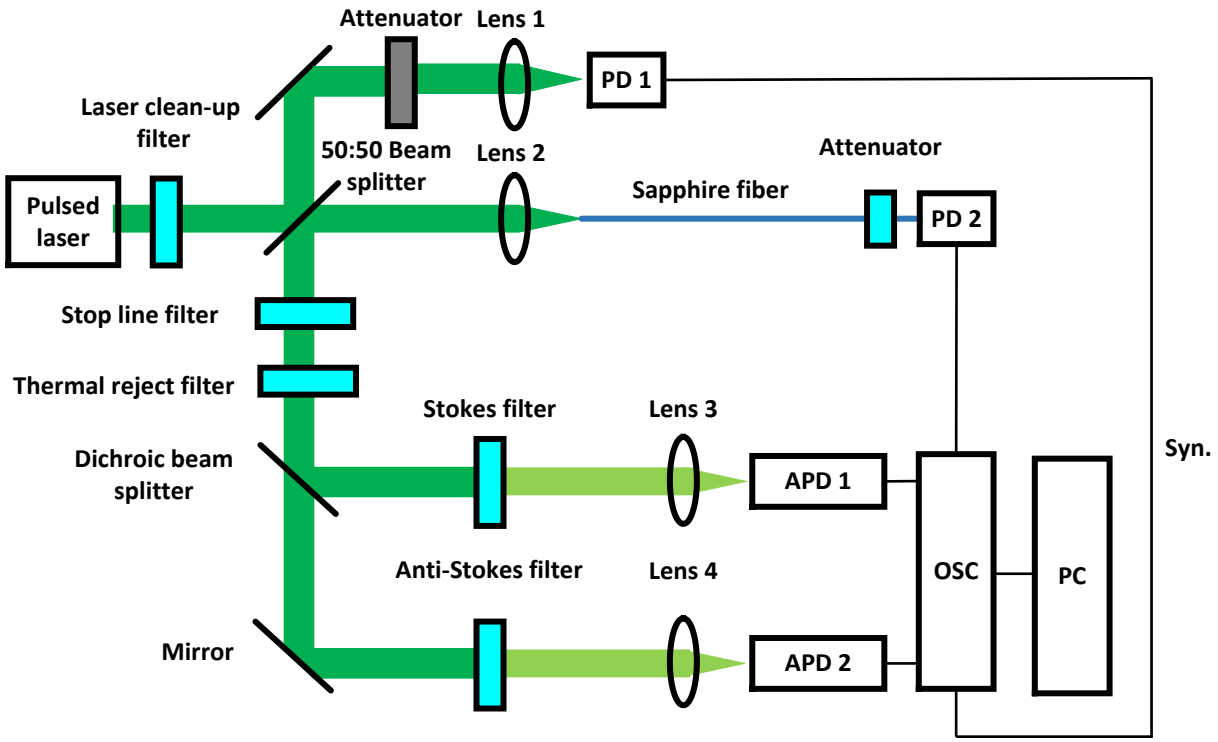

Figure 4-24. Raman DTS system

A detailed summary of all key filters and beam splitters are shown in Table 4-1, including the introduction and information of their type, model number, company, center wavelength and link.

Table 4-1. Summary of filters and beam splitters in sapphire fiber-based RDTS system

Filters	Type	Model Number	Company	Center wavelength
Laser clean-up filter	Band pass	#68-843	Edmund	532 nm
Laser reject filter	Notch filter	NF01-532U-25	Semrock	532 nm
Thermal reject filter	Low pass	FF01-770/SP-25	Semrock	700 nm
Dichroic beam splitter	Dichroic mirror	FF535-SDi01-25x36	Semrock	535 nm
Stokes filter	Band pass	#86-655	Edmund	550 nm
Anti-Stokes filter	Band pass	#87-748	Edmund	510 nm

Stokes filter*	Band pass	LL01-543-12.5	Semrock	543 nm
Anti-Stokes filter*	Band pass	FF01-520/5-25	Semrock	520 nm

* Denotes the components specifically used configurations with picosecond laser.

Another summary in Table 4-2 shows the key information of high-speed PD, APD and oscilloscope (OSC) in this section.

Table 4-2. Summary of the PD, APD, and OSC in sapphire fiber-based RDTS system

Name	Band width	Model Number	Company
PD 1	2 GHz	SV2-FC	Thorlabs
PD 2	< 10 MHz	PDA36A	Thorlabs
APD 1	1 GHz	APD209	Thorlabs
APD 2	1 GHz	APD210	Thorlabs
OSC	< 2.5 GHz	WavePro 725Zi-A	Lecroy

The temperature profile along the ceramic tube was very similar to that shown in Figure 4-14. A K-type thermal couple, whose maximum temperature is limited to 1200ºC, was used to monitor the heating center temperature.

4.3.2 Experimental results with a picosecond laser

This section presents the exploration of RDTS in sapphire fiber with a powerful picosecond laser. To achieve high spatial resolution, the pulse width of the pump light had to be shorter than 1 ns. As a preliminary demonstration, a 532 nm diode-pumped solid state laser with ~5 ps pulse width (Passat Compiler) was used as the light source in the following experiment. The maximum pulse energy was 120 µJ which is far beyond the damage threshold of sapphire fiber. It was attenuated down to ~ 3.75 µJ before entering the beam splitter to prevent damage to the fiber end face. The corresponding peak power was about 700 kW. This high peak power is very close to the damage threshold of sapphire fiber. The sapphire fiber end faces had to be carefully cleaned and dried before proceeding to the experiment.

A 96.5 cm long, 75 µm-diameter sapphire fiber was used as the sensor, with about a 60 cm-long section heated in the tube furnace from room temperature up to 1411 ºC. The heating center is located about 60 cm from the coupling end face. The temperature was kept constant at set temperatures of 100, 400, 600, 800, 1000, 1200, and 1400 ºC. In this test, only one APD was functional. Thus, this experiment was repeated twice. The first one only recorded Anti-Stokes intensity and the second round only recorded Stokes intensity. A B-type thermocouple was used to monitor the center position temperature, as shown in Figure 4-25.

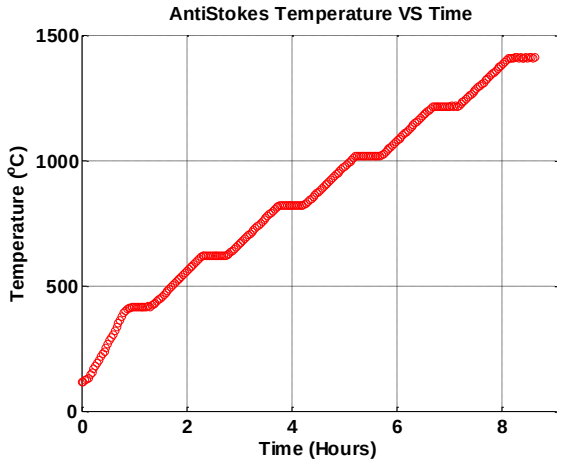

Figure 4-25. Temperature profiler for Raman DTS system with picosecond laser

The time-resolved Raman Stokes and anti-Stokes scattering signals are illustrated in Figure 4-26 and Figure 4-27. The standard deviation of the peak intensities of the Raman Anti-Stokes signals and Stokes signals were 7 ºC and 19 ºC, respectively. The intensity variation was due to the instability of the photodetector and the laser intensity. Figure 4-27 also shows a spatial resolution of ~ 12.4 cm, which was derived from the 10%-90% response distance to a temperature step [14]. It is noted that the heating profile along the sapphire fiber is not a perfect step between the heated section and non-heated section. The heated section maintained a parabolic temperature profile, as shown in Figure 4-14. Due to such a heating profile, the spatial resolution was derived from the beginning section of the fiber. Since the spatial resolution of the current RDTS system is determined by the bandwidth of the oscilloscope, the performance could be further improved by using a high-speed OSC.

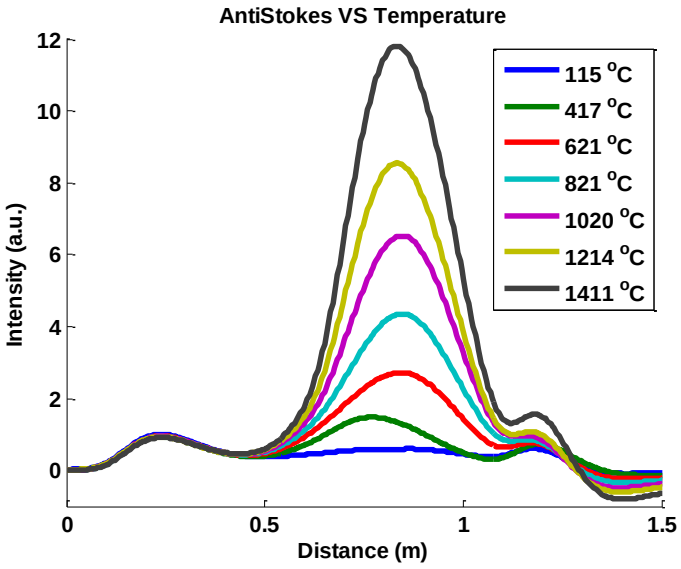

Figure 4-26. Distributed Raman Anti-Stokes signal versus temperature using a picosecond laser

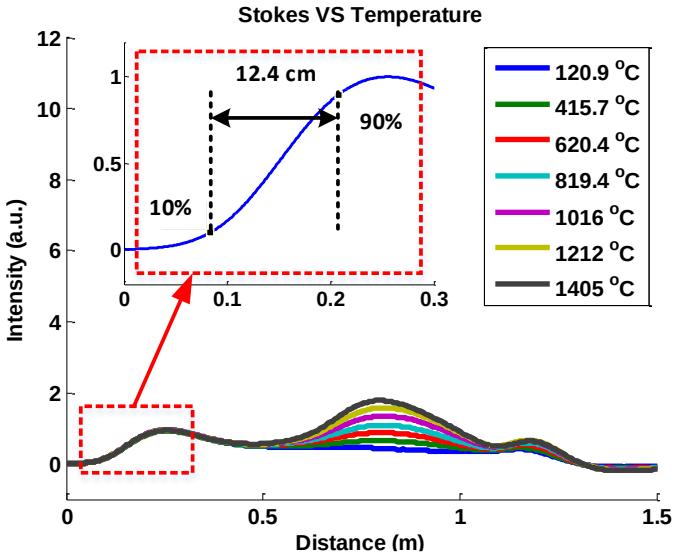

Figure 4-27. Distributed Raman Stokes signal versus temperature using a picosecond laser

By plotting the signal intensities at the heated center, the change of the Stokes and anti-Stokes components versus temperature is illustrated in Figure 4-28. It clearly shows that the Stokes intensity of sapphire fiber's response to temperature was almost linear while the Anti-Stokes intensity increased much quicker at higher temperatures. The increasing trail of Anti-Stokes was

a little different from the curve predicted in Figure 2-5 because the filter of Anti-Stokes in this experiment covered three Raman peaks while the curve in Figure 2-5 only predicts the performance at particular wavelengths. The error bars in Figure 4-28 are within expectation and they are due to the laser light intensity fluctuation and the noise in the detectors. These errors can be greatly reduced when Anti-Stokes and Stokes are detected simultaneously because the final temperature can be determined by the ratio of them. In the next section, the Raman Stokes and Anti-Stokes were measured at the same time, and the standard deviation was proven to be much smaller.

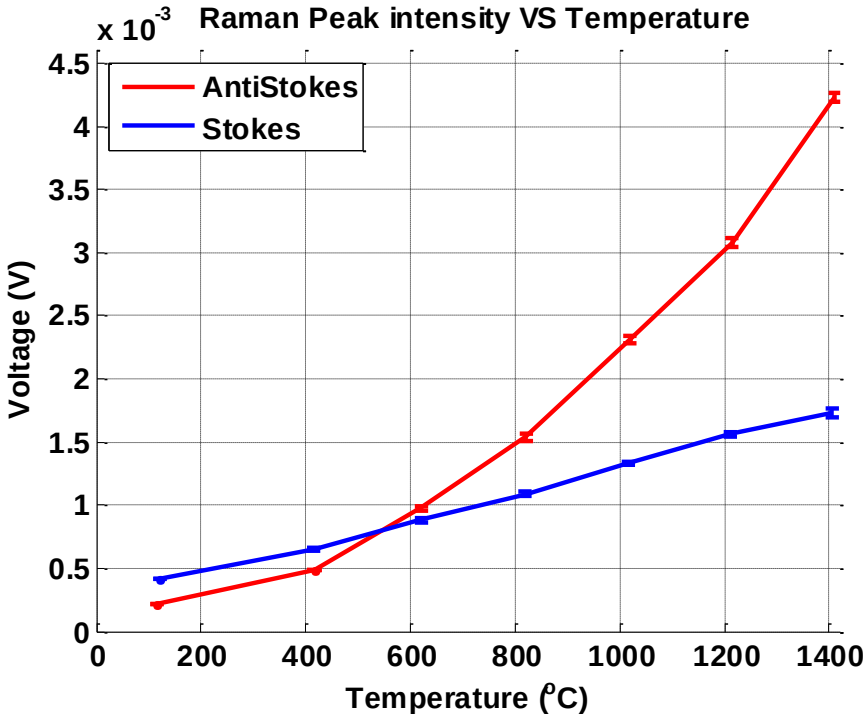

Figure 4-28. The intensities of the Raman Stokes and anti-Stokes scattering lights at the heating center.

The ratio calculated from the data we obtained in this test is shown in Figure 4-29. It was derived from the Raman ratio at the heating center. Because the anti-Stokes and Stokes were measured separately, slight differences in temperature can be found in Figure 4-26 and Figure 4-27, leading to a variation of the Raman ratio. The impact of this variation can be further suppressed by performing the Anti-Stokes and Stokes measurements simultaneously.

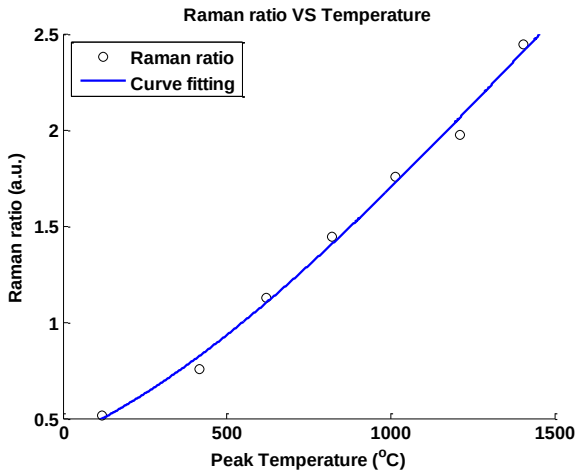

Figure 4-29. Raman ratio verse peak temperature

To demonstrate the spatial-resolving capability of the system, another test was conducted with the heating center moved by 9 cm. As the heating center is shifted along the fiber, the peak on the anti-Stokes curve indicating the heated section shifted notably, as shown in Figure 4-30.

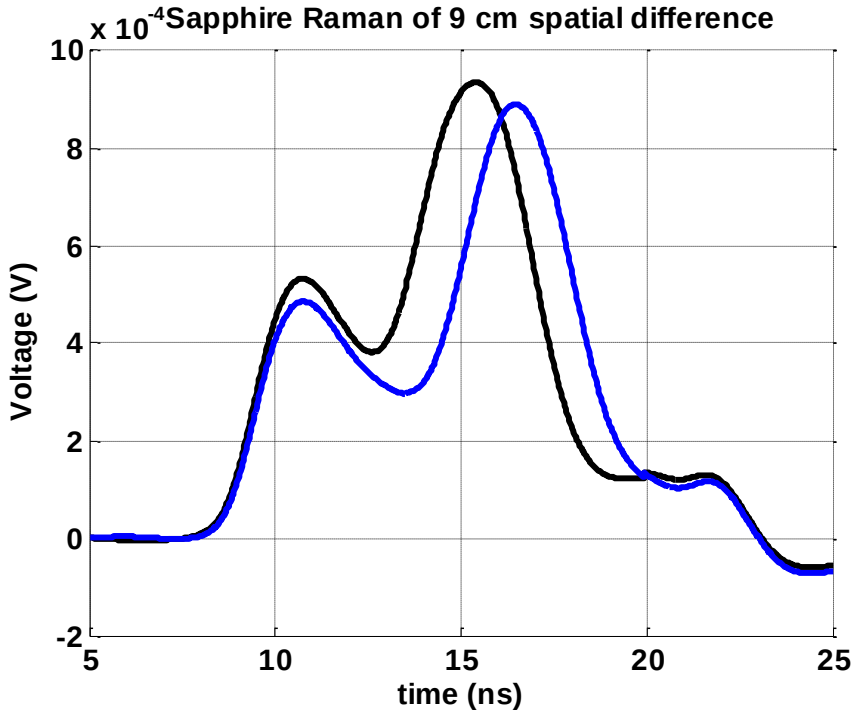

Figure 4-30. Response of Raman Anti-Stokes at different positions

4.3.3 Experimental results with a sub-nanosecond laser

In this section, the laser was replaced by a Passively Q-switched Microchip Lasers at 532 nm. The maximum pulse energy was ~5 µJ and pulse duration was ~700ps. This laser was miniature and more cost effective than the picosecond laser used in Section 4.3.2. Another advantage of this laser was that the calculated peak power (~7kW) was well below the damage threshold. The sapphire Raman signal, Stokes band pass filter, and Anti-Stokes band pass filters were replaced by the new ones. The spectra of the optical Stokes and Anti-Stokes filters used in section 4.3.2 (Dash line), new optical filters used in this section (solid line) and the sapphire fiber Raman signal at 300ºC (red line) are shown in Figure 4-31. It shows that the Stokes filter only covered one major peak (418 cm^{-1}) while the Anti-Stokes filter covered two major peaks (418, 431 cm^{-1}). The band pass window of the new filters allowed all sapphire Raman peaks to pass. Based on the weak Raman intensity and the thermal radiation background measured in section 4.2, the new filter would not saturate the APD.

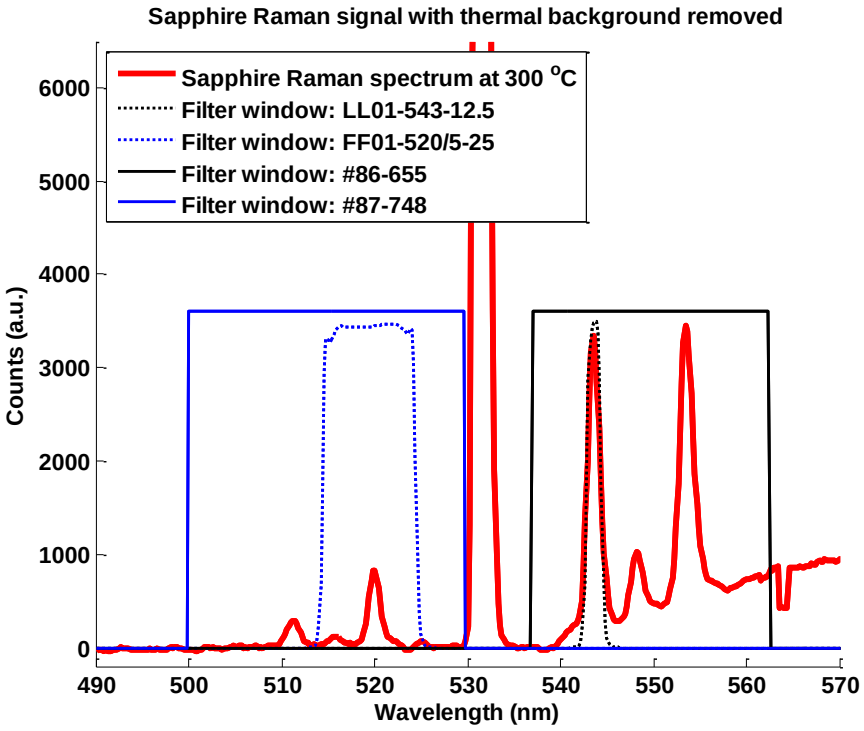

Figure 4-31. Stokes and Anti-Stokes filters and sapphire Raman signal at 300ºC

The experimental setup is schematically shown in Figure 4-24. The sapphire fiber was heated from room temperature up to 1200ºC with a 100ºC incremental step. The temperature was kept constant at each step for 2 hours. The Raman signal, the transmission signal, and the laser trigger signal were averaged and recorded every 3 minutes. The laser repetition rate was 10Hz. The time-resolved Raman Stoke signal and Anti-Stokes signal as a function of temperature are shown in Figure 4-33 and Figure 4-34, respectively. Each measurement was averaged for 180 seconds with 10 traces per seconds. All signals were normalized to cancel the laser power fluctuation as follows.

a) Removing DC components
b) Divide by their reference point which is usually the signal at fiber coupling end.

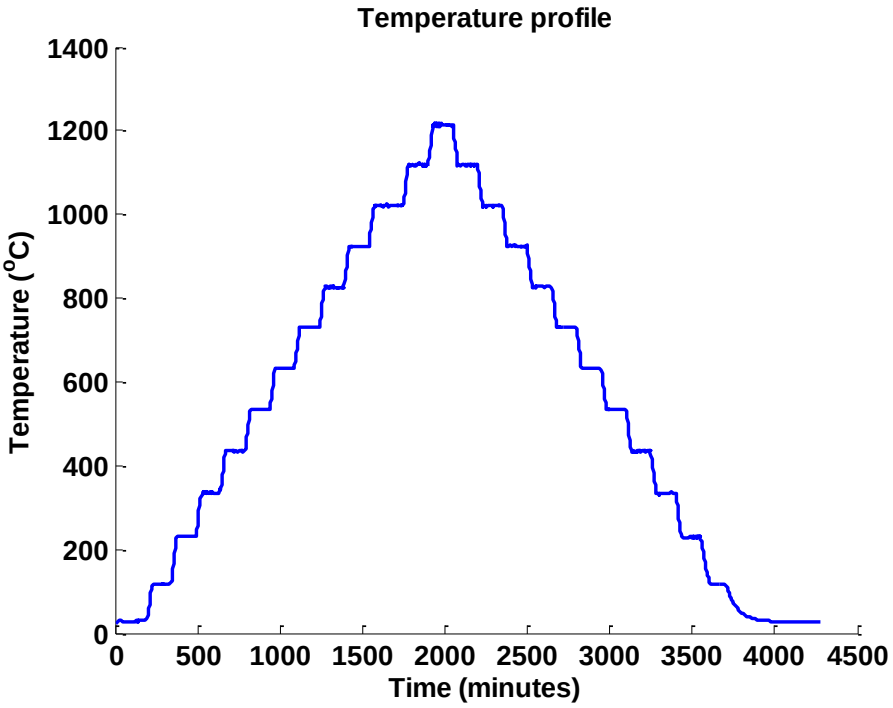

Figure 4-32. Temperature profiler for Raman DTS system with sub-nanosecond laser

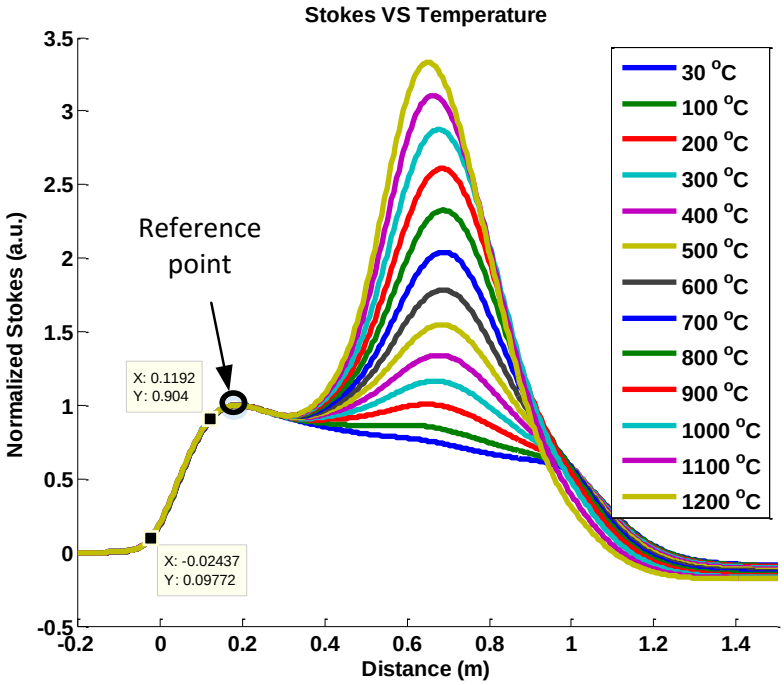

Figure 4-33. Normalized Raman Stokes DTS signal in a 1-meter sapphire fiber

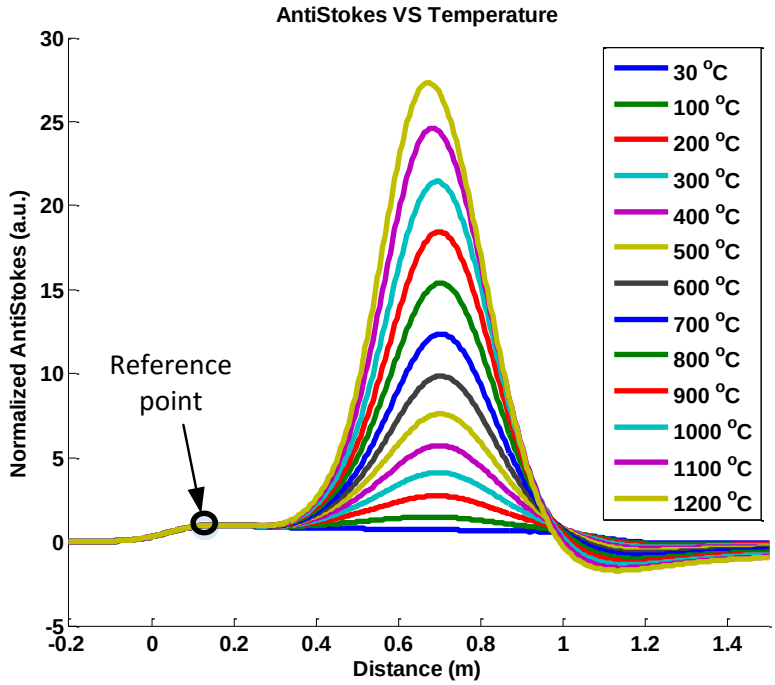

Figure 4-34. Normalized Raman Anti-Stokes DTS signal in a 1-meter sapphire fiber

The corresponding spatial resolution derived from Figure 4-34 is 14 cm. The Raman signal at heated positions varied with temperature while they remained constant at non-heated positions. The mismatch at the fiber end section was due to the dead-time effect of the APD, which is common and can be eliminated with proper calibration[41]. Although signal degradation due to surface scattering, contamination, and impurity absorption losses is of concern for applications with an unclad sapphire fiber, the signal can still be well resolved using the ratio of Anti-Stokes signal over Stokes signal. Since the Stokes signal undergoes similar waveguide attenuation as the Anti-Stokes signal, the Stokes signal was widely used as a candidate to cancel out the negative effect from optical coupling instability, laser power fluctuation and random attenuation induced by contamination. This self-calibration capability ensures long-term stability and won the trust in many industry applications since the first day of the Raman OTDR technique.

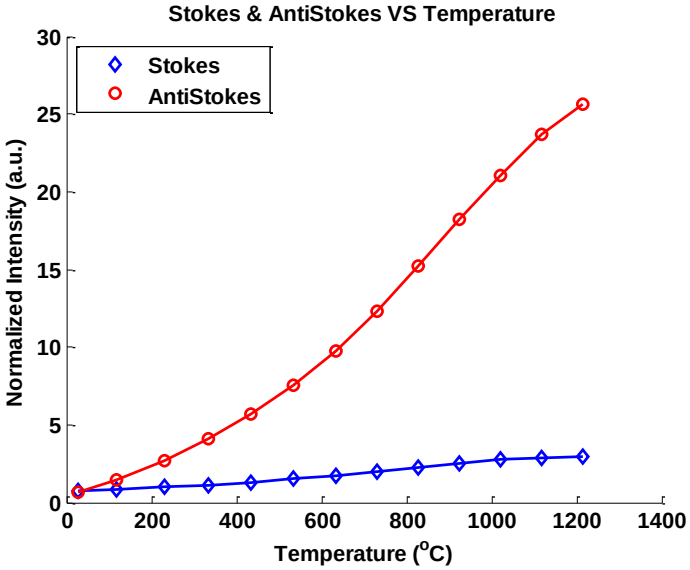

Figure 4-35. Normalized intensity of Raman signals at the heating center

Figure 4-35 shows the normalized Raman signal amplitude of the data point at the heating center as a function of temperature in the temperature-rising period. The experimental results show that Raman Anti-Stokes signal is more sensitive than Raman Stokes signal which agrees with the theoretical predictions. The demodulated signals at temperature rising period are almost the same as the temperature falling period in the sapphire fiber RDTS.

Signal Processing

The signal processing was discussed in detail in Chapter 2. However, in sapphire fiber-based Raman DTS system, the strict signal processing is very complex mainly due to the multi-peak spectrum. A very simple signal processing method is based on the curve fitting. Since all DTS systems require a one-time calibration before use, this calibration only needs to be performed once as well. The curve fitting equation is usually 3rd or 5th order equation. In this experiment, the curve fitting equation is given by

$$T(^{\circ}\mathrm{C}) = -1729 \cdot \mathrm{R}^3 + 13785 \cdot R^2 + 3215.6 \cdot R - 49.881 \qquad \textbf{(4-2)}$$

where R is the Raman ratio and T is the demodulated temperature.

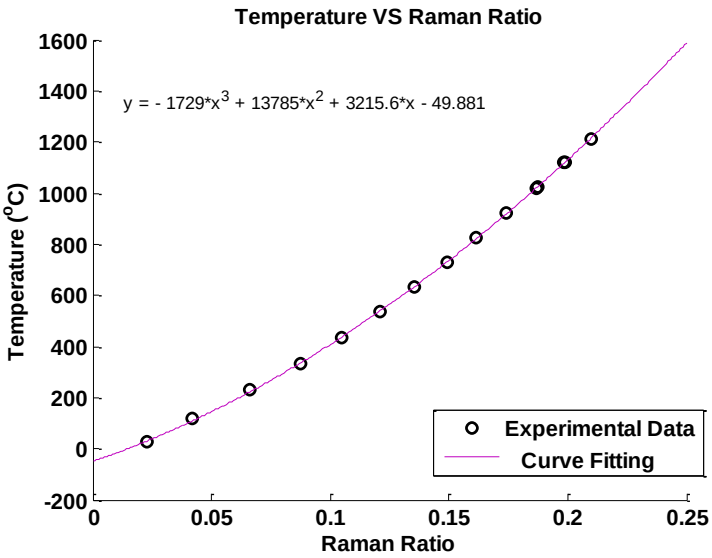

Figure 4-36. Curve fitting of Temperature demodulation as a function of Raman ratio

The temperature rise and fall processes followed the same fitting curve, which is shown in Figure 4-37. There was some mismatch between the temperature rising and the temperature falling processes, which is very likely due to the temperature variation of the furnace and the instability of the APD.

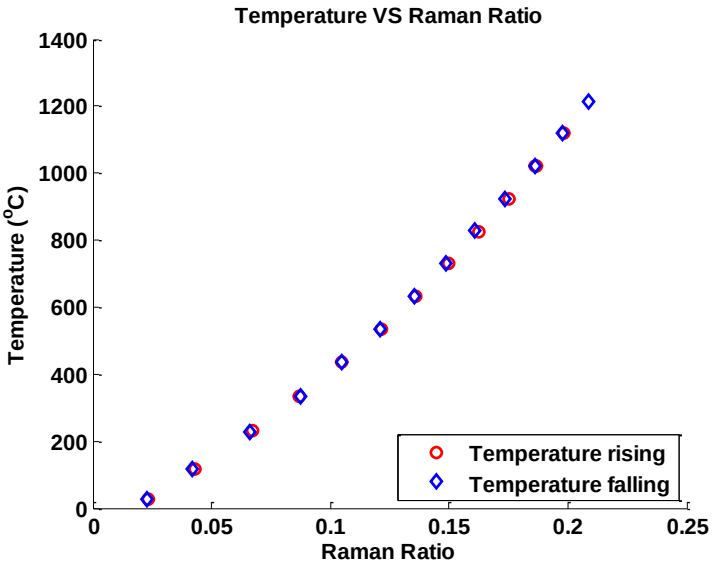

Figure 4-37. Demodulated temperature measurement at heating center in a 1-meter sapphire fiber

Standard deviation

At each temperature step, there were over 20 measurements. The average time of each measurement was 3 minutes with 1800 traces in total. A temperature standard deviation is calculated based on the formula:

$$S = \sqrt{\frac{1}{N-1}\sum_{i=1}^{N}\left|A_i - \mu\right|^2} \qquad \textbf{(4-3)}$$

where N is the number of observations, A_i represents the random variables, μ is the mean value of all random variables defined by $\mu = \frac{1}{N}\sum_{i=1}^{N} A_i$.

The standard deviations at the temperature rising period and temperature falling period are shown in Figure 4-38. The blue error bar and numbers correspond to the standard deviation of temperature rising period. The red ones correspond to the standard deviation of temperature falling period. The average standard deviation at the heating center was 3.7ºC. The temperature standard deviation

was about 3.0ºC in non-heating sections mainly due to less attenuation. The standard deviations of thermocouple readings are plotted in Figure 4-39. It shows that the standard deviation of the sapphire RDTS system and furnace temperature at 1200ºC were 4.5ºC and 2.3 ºC, respectively. The standard deviation of the sapphire RDTS system remains constant at all temperatures while the standard deviation of thermocouple measurement increases at higher temperatures.

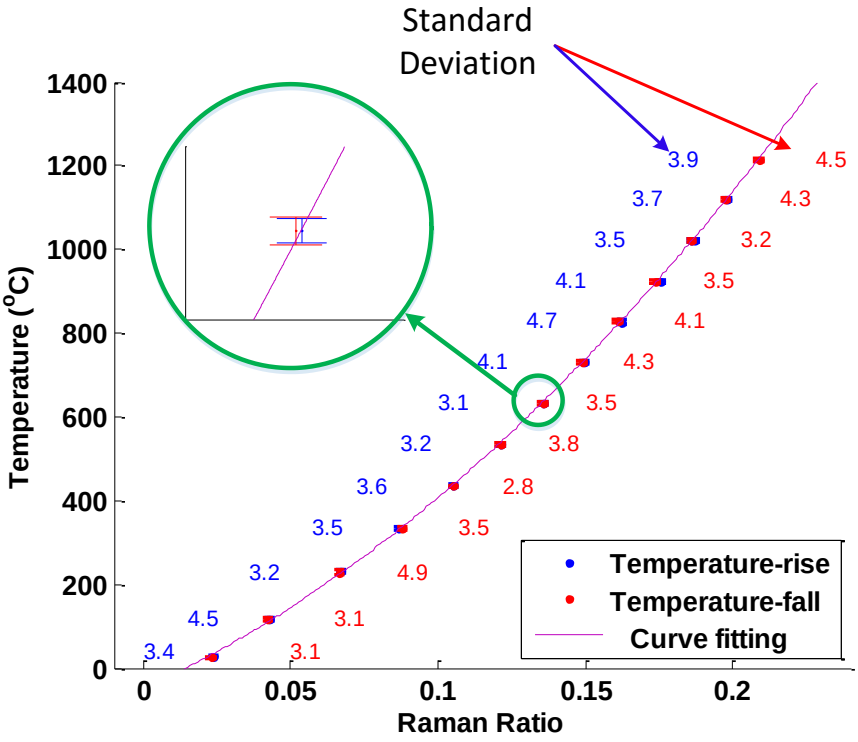

Figure 4-38. Standard deviation of the demodulated temperature at heating center

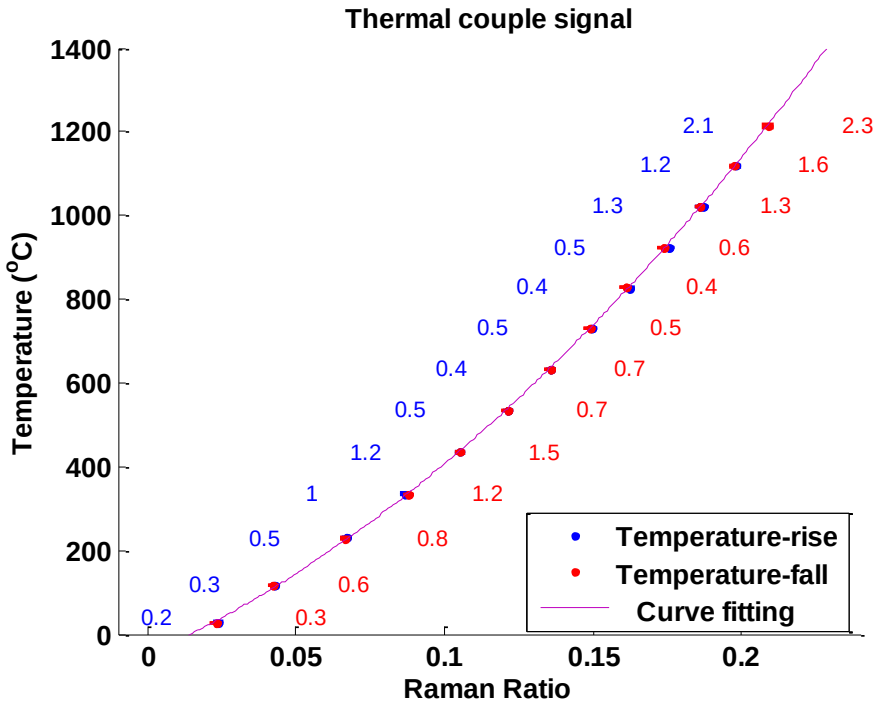

Figure 4-39. Standard deviation of the measurement results of RDTS system

DTS system versus thermocouple

The demodulated temperature result shown in Figure 4-40 is an accurate representation of the temperature information along the FUT in a fully distributed manner.

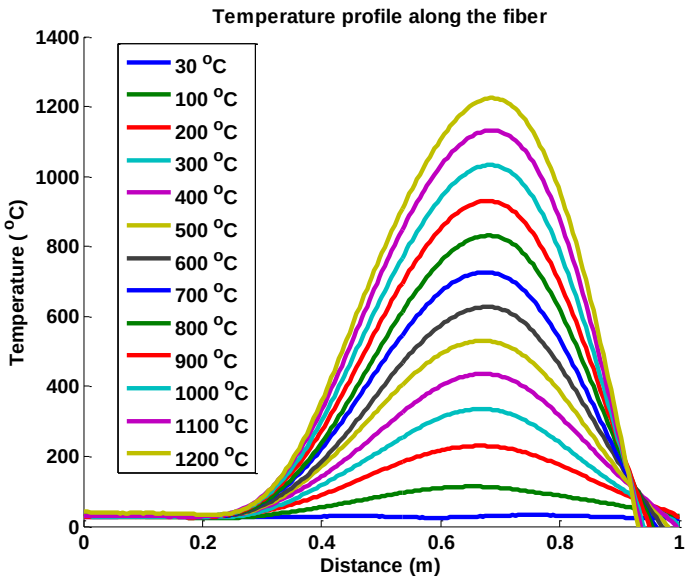

Figure 4-40. Distributed temperature measurement result based RDTS

In an effort to demonstrate the distributed temperature sensing capability, a 1.62 m long sapphire fiber was heated at different locations with each 1 cm interval at 500 ºC constant temperature. The Anti-Stokes signal response was shown in Figure 4-41. The non-heating section remains the same while the heated section moves at exactly the same displacement.

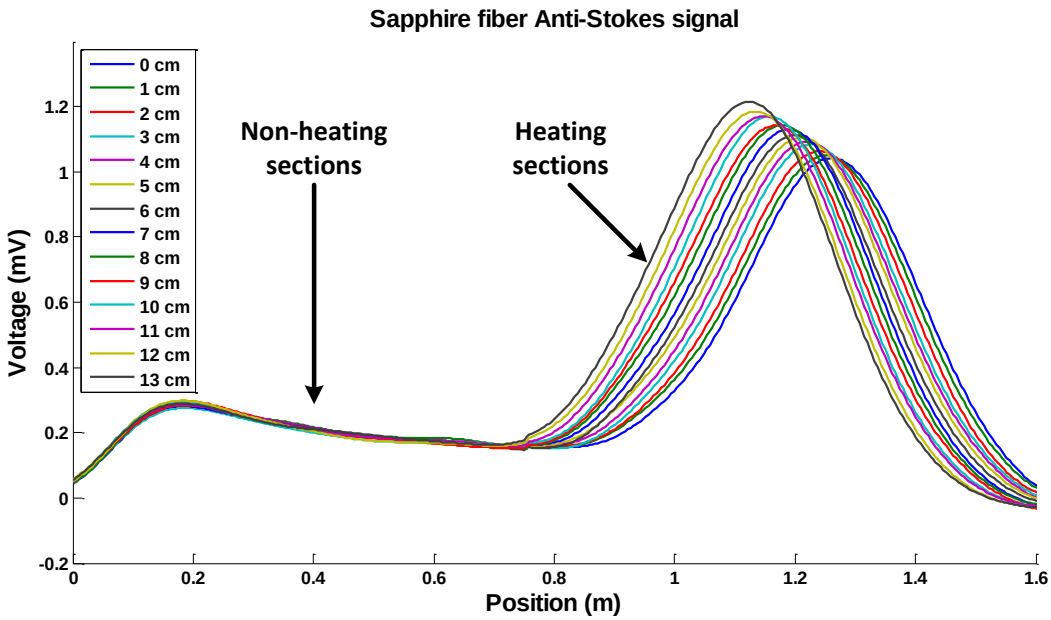

Figure 4-41. Sapphire fiber Anti-Stokes response to different heating positions at each 1 cm intervals

The single point demodulated temperature results at the heating center were also compared with the thermocouple reading results, as shown in Figure 4-42. The sapphire fiber-based DTS shows larger standard deviation than the thermocouple but its stability is better. The standard deviation can be improved by increasing the laser repetition rate.

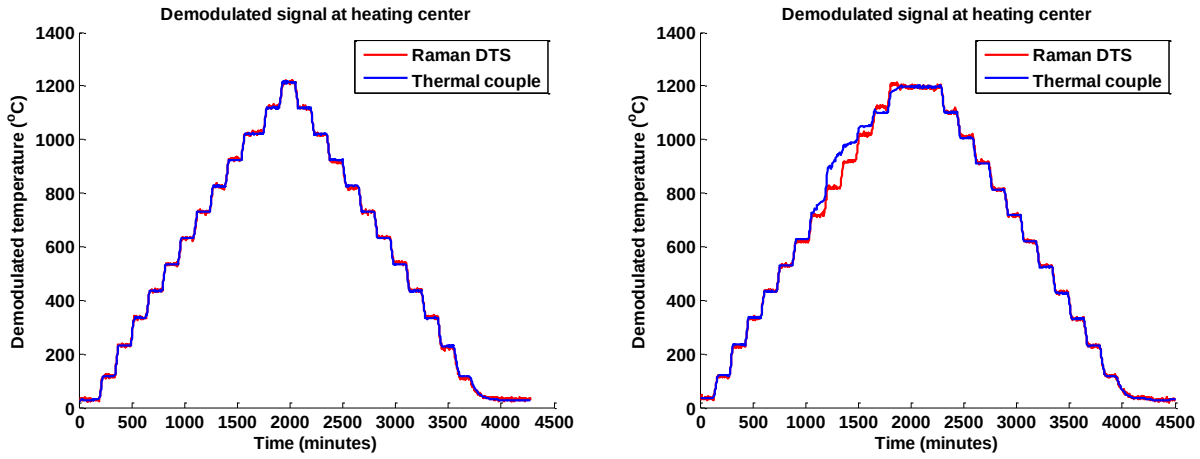

Figure 4-42. Result comparison between sapphire Raman DTS and thermal couple reading in two identical experiments

The standard deviation of the demodulated temperature along the fiber is plotted in Figure 4-43. It shows that the standard deviation does not change from room temperature to 1200ºC along the fiber except at the end section of the fiber. The increased error at the end section of the fiber is due to the dead-time effect of the APD.

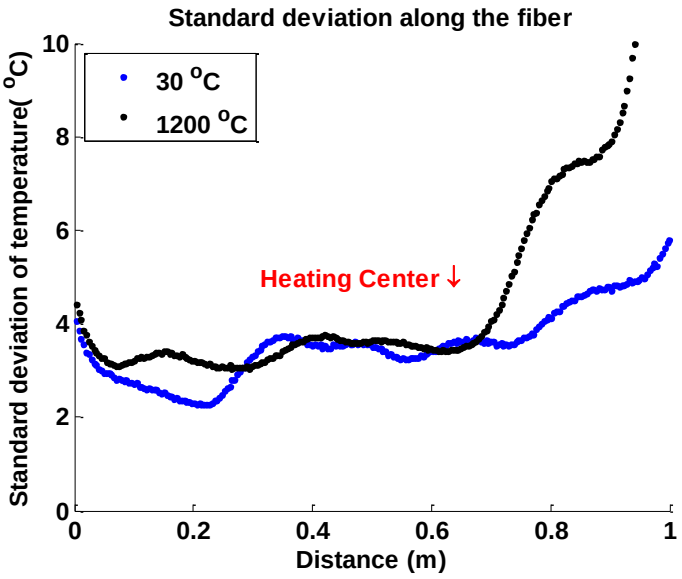

Figure 4-43. Standard deviation of along the fiber

DTS system with 2 m and 3 m sapphire fibers

To extend the sensing length via a sequential approach, the Raman DTS system was demonstrated in a 122μm-diameter, 2-meter-long sapphire fiber. The experimental schematic was consistent with that shown in Figure 4-24. The heating center was located ~1.6 m from the coupling end face, and was heated from 200ºC to 1200ºC at intervals of 200ºC. The time-resolved Raman Stokes signals and Anti-Stokes signals are shown in Figure 4-44.

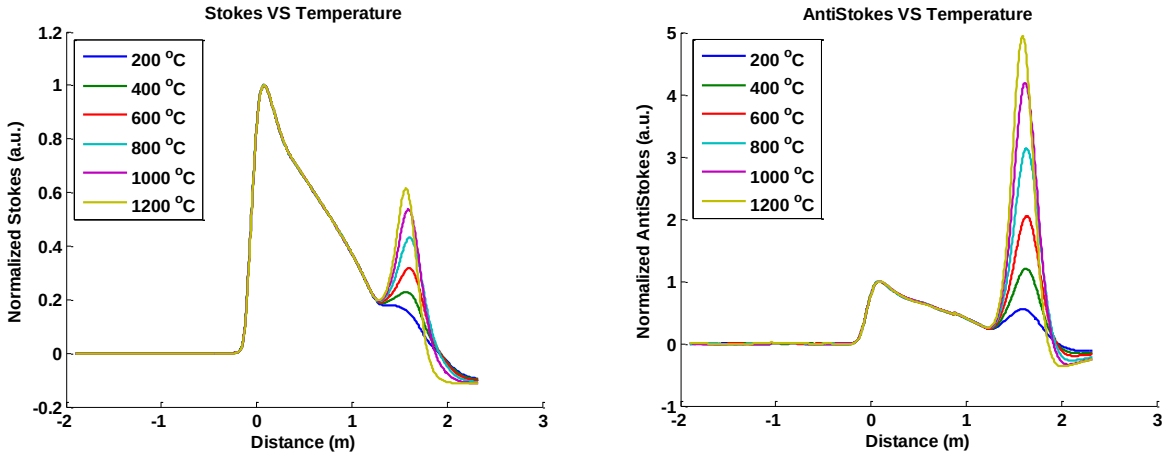

Figure 4-44. Raman DTS measurement in a 2-meter-long sapphire fiber

The demodulated temperature at the heating center over the temperature rising and temperature falling periods is shown in Figure 4-45. The observed slight variation between temperature rising period and temperature falling period may be caused by the instability of the APD.

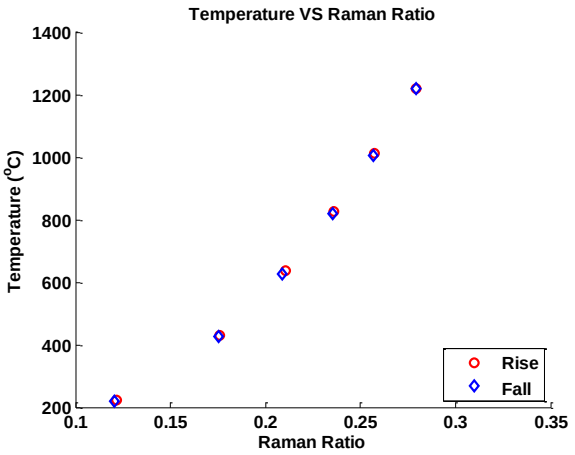

Figure 4-45. Demodulated temperature measurement at heating center in a 2-meter sapphire fiber

The Raman DTS system was also tested in a 3-meter-long sapphire fiber via the same approach, but the heating center was close to the end of the fiber. Since commercially available sapphire fiber (122μm diameter) is limited to a length of 2-meters, a 1-meter-long sapphire fiber (125μm diameter) was connected to a 2-meter-long sapphire fiber (122μm diameter). All fiber ends were made into 140μm APC pigtails. Consistent with prior configurations, the system was identical to those shown in Figure 4-24. The repetition rate was 10 Hz and the average time was 30 minutes. The time-resolved Raman Stokes and Anti-Stokes signal are shown in Figure 4-46. A joint reflection was observed, which was due to the Raman signal and other signals at the joint point. A significant loss at the joint point was due to the mismatch of the fiber diameter and the offset at 122μm/125μm sapphire fiber in 140μm pigtails.

The signal demodulation of the 3-meter-long sapphire fiber system required additional calibration because the corresponding voltage dropped below zero. The Raman intensities as a function of temperature are displayed in Figure 4-47.

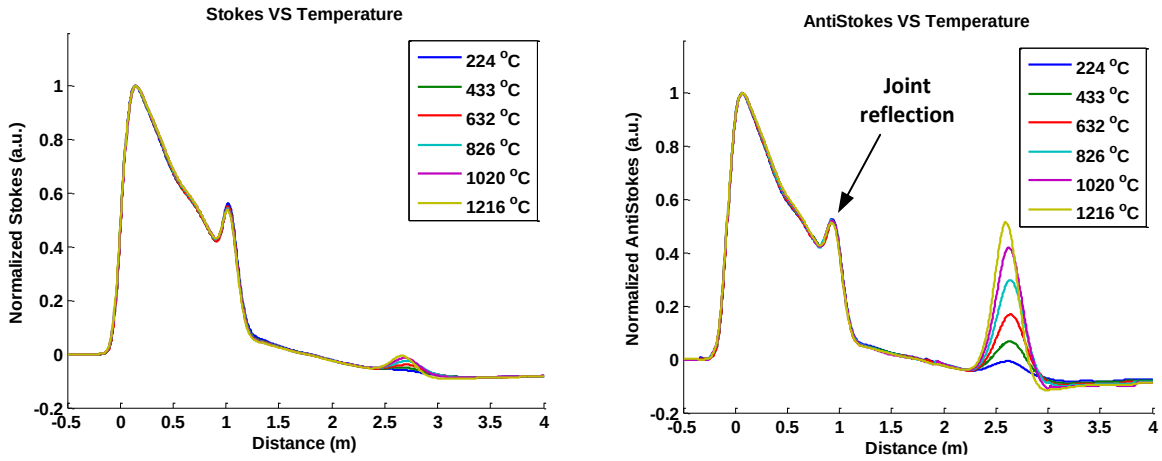

Figure 4-46. Raman DTS measurement in a 3-meter sapphire fiber

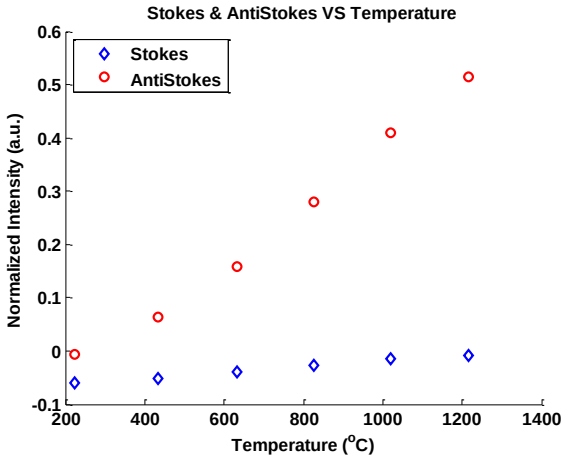

Figure 4-47. The normalized Raman signals vary at different temperatures in a 3 m sapphire fiber

Spatial resolution in a 3 m sapphire fiber

To evaluate the spatial resolution of the sapphire fiber-based Raman DTS system, the sapphire fiber was heated up to 1400ºC with the heating position at the same location, very close to the end of the 3-meter-long fiber. The Raman Anti-Stokes signal is shown in Figure 4-48. The corresponding spatial resolution was 16.4 cm which was derived from the 10%-90% response distance to a temperature step. It is anticipated that the spatial resolution was better than 16.4 cm because a perfect temperature step could not be obtained from this tube furnace.

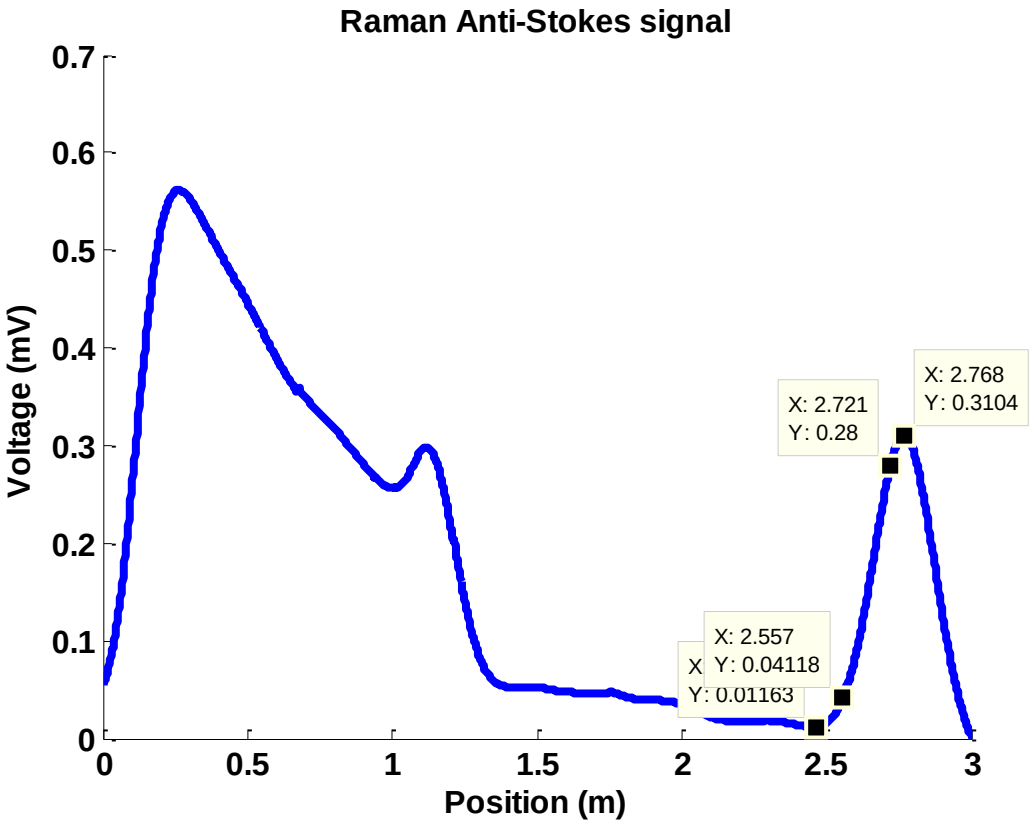

Figure 4-48. Spatial resolution measurement of in a 3-meters sapphire fiber

5 SUMMARY AND FUTURE WORK

The observation of the Raman Anti-Stokes signal in sapphire fiber was reported for the first time. We measured the temperature dependence of sapphire Raman line intensity, frequency shift, and linewidth up to 1033 ºC. The temperature dependence of fluorescence light due to impurities in the sapphire fiber was also observed. These experiments demonstrated that the Anti-Stokes components in sapphire fiber are more sensitive to temperature compared with Stokes components and the intensity becomes comparable to the Stokes components at a higher temperature.

Based on these results, a sapphire fiber-based distributed temperature sensing system was designed and implemented. Our preliminary results show excellent and consistent temperature resolution from room temperature up to 1400 ºC. The temperature standard deviation is 3.0ºC (0.2% full scale) in a one-meter sapphire fiber. The spatial resolution is less than 16.4 cm in a three meters sensing range. To our best knowledge, this is the first demonstration of a sapphire fiber based distributed temperature sensing of any kind. This technology may find a wide range of industrial applications.

There are several improvement possibilities and interesting directions to further push the limit of this DTS technique. Some of them are listed below.

1) The repetition rate of the laser can easily increase to several thousand kHz to enable a fast response and dynamic DTS system.
2) This DTS system will not be limited to Raman-based technique but potentially can be expanded to a Rayleigh-based technique.
3) The system used in this research was a free-spaced system at 532 nm which can potentially develop into an all-fiber-based system at longer wavelengths. To avoid the sapphire fiber fluorescence at 694.3 nm and strong blackbody radiation at IR range, the suggested wavelength is between 700~900 nm. By shifting the laser wavelength, it is possible to develop an all fiber-based Raman DTS with sapphire fiber. This system will be miniature, robust and will have long term stability.
4) Due to the upper limit of the tube furnace (1400 ºC), the maximum temperature sensing limit is not fully exploited yet. Although the sapphire fiber attenuation increases at higher

temperature, we have demonstrated that the standard deviation does not change at a higher temperature. Thus, this method could potentially be used at a much higher temperature such as 1600 ºC and beyond.

5) Replacing the current pulsed laser with low-cost diode laser is a promising direction.
6) The spatial resolution of this system can be further improved using reduced-mode sapphire fiber.

Based on this Ph.D. study, the following publications and provisional patents has been generated and part of them are listed:

1. **B. Liu**, Z. H. Yu, C. Hill, Y. J. Cheng, D. Homa, A. Wang, G. Pickrell, "Sapphire fiber-based Distributed High Temperature Sensing System" Optics Letters, Vol. 41, 4405-4408, (2016).
2. **B. Liu**, Z. H. Yu, Z. P. Tian, D. Homa, C. Hill, A. Wang, G. Pickrell, "Temperature dependence of sapphire fiber Raman scattering," Optics Letters, vol. 40, pp. 2041-2044, (2015).
3. Y. Cheng, C. Hill, **B. Liu**, Z. Yu, H. Xuan, D. Homa, A. Wang, and G. Pickrell, "Design and analysis of large-core single-mode windmill single crystal sapphire optical fiber," Optical Engineering 55, 066101 (2016).
4. C. Hill, D. Homa, Y. Cheng, **B. Liu**, Z. Yu, A. Wang, G. Pickrell, " Activation Energies and Rates Associated with the Wet-Acid Etching of a-Plane Single-Crystal Sapphire ", Submitting, (2016)
5. Y. Cheng, C. Hill, **B. Liu**, Z. Yu, H, Xuan, D. Homa, A. Wang and G. Pickrell, "Modal reduction in single crystal sapphire optical fiber", Optical Engineering, 54(10), (2015).
6. C. Hill, D. Homa, **B. Liu**, Z. Yu, A. Wang, G. Pickrell, “Submicron diameter single crystal sapphire optical fiber,” Materials Letters, 138,71-74, (2015).
7. **B. Liu**, Z. H. Yu, D. Homa, A. Wang, G. Pickrell, “Distributed high temperature sensing with sapphire optical fiber”, Provisional patent No. 62264659, (2015)

Some other work was published during the Ph.D. study:

8. **B. Liu**, D. Wang, A. Wang, “Liquid-Surface-Level Sensing Based on Transverse Pulse Train Technique”, IEEE Sensors, Vol. 16, No 8, pp.2317-2321(2016).
9. T. Z. Peng, Z. H. Yu, **B. Liu**, A. Wang, "Sourceless sapphire optical fiber Fabry-Perot interferometer for high temperature measurement", Optics Letters, Vol. 41, No. 2, pp. 195-198 (2016).
10. J. Yi, C. Jao, I. L. N. Kandas, **B. Liu**, Y. Xu, and H. D. Robinson, "Irreversible adsorption of gold nanospheres on fiber optical tapers and microspheres," Appl. Phys. Lett., 100 (15), Art. No. 153107, (2012).
11. **B. Liu**, Y. Wang, A. Wang, “Fluid/Gas Interface Sensing Based on Traverse Wave and Pulse Train Technique”, Provisional patent application No. 62/047346, (2014).
12. B. Dong, A. Behera, **B. Liu**, S. Zhang, J. Gong, A. Wang, “Fiber Optic Gas Monitoring System”, Full patent No. WO2015038217 A1, (2014).

REFERENCES

1. C. Moore, A. Barnard, P. Fietzek, M. R. Lewis, H. M. Sosik, S. White, and O. Zielinski, "Optical tools for ocean monitoring and research," Ocean Science **5**, 661-684 (2009).
2. "Voyager 1" (Wikipedia, 2016), retrieved 11 Aug., 2016, https://en.wikipedia.org/wiki/Voyager_1.
3. eia, "U.S. Energy Information Administration" (2015), retrieved http://www.eia.gov/.
4. W. B. Dress; and G. N. Miller, "An ultrasonic level and temperature sensor for power reactor applications," U.S. Nuclear Regulatory Commission **3445600340405**(1984).
5. "Fukushima Daiichi nuclear disaster" (wikipedia, 2015), retrieved 11 Aug., 2015, https://en.wikipedia.org/wiki/Fukushima_Daiichi_nuclear_disaster.
6. C. Ma and A. Wang, "Signal processing of white-light interferometric low-finesse fiber-optic Fabry-Perot sensors," Appl Opt **52**, 127-138 (2013).
7. Y. Wang, J. Gong, D. Y. Wang, B. Dong, W. Bi, and A. Wang, "A Quasi-Distributed Sensing Network With Time-Division-Multiplexed Fiber Bragg Gratings," IEEE Photonics Technology Letters **23**, 70-72 (2011).
8. D. K. S. Gifford, Brian J. , M. S. Wolfe, and M. E. Froggatt, "Distributed Fiber-Optic Temperature Sensing using Rayleigh Backscatter," Proc. ECOC (2005).
9. Q. Cui, S. Pamukcu, A. Lin, W. Xiao, D. Herr, J. Toulouse, and M. Pervizpour, "Distributed Temperature Sensing System Based on Rayleigh Scattering BOTDA," IEEE Sensors Journal **11**, 399-403 (2011).
10. Y. K. Dong, H. Y. Zhang, L. Chen, and X. Y. Bao, "2 cm spatial-resolution and 2 km range Brillouin optical fiber sensor using a transient differential pulse pair," Applied Optics **51**, 1229-1235 (2012).
11. X. Bao and L. Chen, "Recent progress in distributed fiber optic sensors," Sensors (Basel) **12**, 8601-8639 (2012).
12. G. Bolognini, J. Park, P. Kim, D. Lee, F. D. Pasquale, and N. Park, "Performance Enhancement of Raman-based Distributed Temperature Sensors using Simplex Codes," Optical Society of America (2005).
13. M. G. Tanner, S. D. Dyer, B. Baek, R. H. Hadfield, and S. Woo Nam, "High-resolution single-mode fiber-optic distributed Raman sensor for absolute temperature measurement using superconducting nanowire single-photon detectors," Applied Physics Letters **99**, 201110 (2011).

14. M. A. Soto, T. Nannipieri, A. Signorini, A. Lazzeri, F. Baronti, R. Roncella, G. Bolognini, and F. Di Pasquale, "Raman-based distributed temperature sensor with 1 m spatial resolution over 26 km SMF using low-repetition-rate cyclic pulse coding," Optics Letters **36**, 2557-2559 (2011).
15. G. H. Watson, W. B. Daniels, and C. S. Wang, "Measurements of Raman Intensities and Pressure-Dependence of Phonon Frequencies in Sapphire," Journal of Applied Physics **52**, 956-958 (1981).
16. K. S. Chiang, "Stimulated Raman scattering in a multimode optical fiber: evolution of modes in Stokes waves," Optics letters **17**, 352-354 (1992).
17. N. B. Terry, T. G. Alley, and T. H. Russell, "An explanation of SRS beam cleanup in graded-index fibers and the absence of SRS beam cleanup in step-index fibers," Optics Express **15**, 17509-17519 (2007).
18. A. Polley and S. E. Ralph, "Raman amplification in multimode fiber," IEEE Photonics Technology Letters **19**(2007).
19. J. P. Dakin, J. D, Pratt, G. W. Bibby, and J. N. Ross, "Temperature distribution measurement using Raman ratio thermometry," Fiber optic and laser sensors III **566**, 249-256 (1985).
20. S. D. D. Michael G. Tanner, Burm Baek, Robert H. Hadfield, Sae Woo Nam, "High-resolution single-mode fiber-optic distributed Raman sensor for absolute temperature measurement using superconducting nanowire single-photon detector," Applied Physics Letters **99**(2011).
21. M. Ashkin, J. H. P. Jr., and D. W. Feldman, "Temperature dependence of the Raman lines of α-Al_2O_3," Solid state communications **6**, 4 (1968).
22. D. Y. Wang, Y. M. Wang, J. M. Gong, and A. B. Wang, "Fully distributed fiber-optic temperature sensing using acoustically-induced rocking grating," Optics Letters **36**, 3392-3394 (2011).
23. Y. Wang, "Fiber-Optic Sensors for Fully-Distributed Physical, Chemical and Biological Measurement," (Citeseer, 2012).
24. "Lord Rayleigh - Biographical" (Nobel Media AB 2014. Web.), retrieved 12 Aug 2016., http://www.nobelprize.org/nobel_prizes/physics/laureates/1904/strutt-bio.html.
25. A. K. Sang, M. E. Froggatt, D. K. Gifford, S. T. Kreger, and B. D. Dickerson, "One Centimeter Spatial Resolution Temperature Measurements in a Nuclear Reactor Using Rayleigh Scatter in Optical Fiber," IEEE Sensors Journal **8**, 1375-1380 (2008).
26. "Leonid Mandelstam" (Wikipedia), retrieved 11 Aug., 2016, https://en.wikipedia.org/wiki/Leonid_Mandelstam.
27. "Brillouin Scattering" (Wikipedia), retrieved 11 Aug., 2016, https://en.wikipedia.org/wiki/Brillouin_scattering.

28. E. L. Feinberg, "The forefather (about Leonid Isaakovich Mandelstam)," Physics-Uspekhi **45**, 81-100 (2002).
29. X. Bao and L. Chen, "Recent progress in optical fiber sensors based on Brillouin scattering at university of Ottawa," Photonic Sensors **1**, 102-117 (2011).
30. D. Inaudi and B. Glisic, "Long-Range Pipeline Monitoring by Distributed Fiber Optic Sensing," Journal of Pressure Vessel Technology **132**, 011701 (2010).
31. S. Bhagavantam, "Chandrasekhara Venkata Raman. 1888-1970," Biographical Memoirs of Fellows of the Royal Society **17**, 564-592 (1971).
32. D. K. Lonsdale and H. J. Bhabha, "Kariamanikkam Srinivasa Krishnan. 1898-1961," Biographical Memoirs of Fellows of the Royal Society **13**, 244-255 (1967).
33. G. P. Agrawal, *Nonlinear Fiber Optics* (Academic Press, USA, 2013).
34. H. S. Pradhan and P. K. Sahu, "Spontaneous Brillouin scattering based distributed fiber optic temperature sensor design and simulation using phase modulation and optimization technique," 300-304 (2012).
35. V. Lambin Iezzi, S. Loranger, A. Harhira, R. Kashyap, M. Saad, A. Gomes, and S. Rehman, "Stimulated Brillouin scattering in multi-mode fiber for sensing applications," 1-4 (2011).
36. G. Pickrell, E. Udd, H. H. Du, S. T. Kreger, J. W. Klein, N. A. A. Rahim, and J. J. Bos, "Distributed Rayleigh scatter dynamic strain sensing above the scan rate with optical frequency domain reflectometry," **9480**, 948006 (2015).
37. D. Garcus, T. Gogolla, K. Krebber, and F. Schliep, "Brillouin optical-fiber frequency-domain analysis for distributed temperature and strain measurements," Journal of Lightwave Technology **15**, 654-662 (1997).
38. B. Liu, Z. H. Yu, Z. P. Tian, D. Homa, C. Hill, A. Wang, and G. Pickrell, "Temperature dependence of sapphire fiber Raman scattering," Optics Letters **40**, 2041-2044 (2015).
39. J. P. Dakin, "Temperature measuring arrangement," US Patent GB2140554A (1983).
40. J. P. Dakin, D. J. Pratt, G. W. Bibby, and J. N. Ross, "Distributed optical fibre Raman temperature sensor using a semiconductor light source and detector," Electronics Letters **21**, 569 (1985).
41. M. Hobel, J. Ricka, M. Wuthrich, and T. Binkert, "High-resolution distributed temperature sensing with the multiphoton-timing technique," Applied optics **34**, 2955-2967 (1995).
42. D. Wardle, "Raman scattering in optical fibres," (ResearchSpace@ Auckland, 1999).

43. J. Park, G. Bolognini, D. Lee, P. Kim, P. Cho, F. Di Pasquale, and N. Park, "Raman-based distributed temperature sensor with simplex coding and link optimization," Ieee Photonics Technology Letters **18**, 1879-1881 (2006).

44. M. A. Soto, P. K. Sahu, S. Faralli, G. Bolognini, F. D. Pasquale, B. Nebendahl, and C. Rueck, "Distributed temperature sensor system based on Raman scattering using correlation-codes," ELECTRONICS LETTERS **43**(2007).

45. G. Bolognini, J. Park, M. A. Soto, N. Park, and F. Di Pasquale, "Analysis of distributed temperature sensing based on Raman scattering using OTDR coding and discrete Raman amplification," Measurement Science and Technology **18**, 3211-3218 (2007).

46. Wikipedia, "Raman Spectroscopy" (2016), retrieved https://en.wikipedia.org/wiki/Raman_spectroscopy.

47. W. J. Bock, D. K. Gifford, M. E. Froggatt, S. T. Kreger, J. Albert, and X. Bao, "High precision, high sensitivity distributed displacement and temperature measurements using OFDR-based phase tracking," **7753**, 77533I-77533I-77534 (2011).

48. K. Chen, X. Zhou, W. Peng, and Q. Yu, "Optical frequency domain reflectometry based single-mode fiber-optic distributed temperature sensor using synchronous polarization scrambling technique," Optical Engineering **54**, 037104 (2015).

49. C. A. Galindez-Jamioy and J. M. López-Higuera, "Brillouin Distributed Fiber Sensors: An Overview and Applications," Journal of Sensors **2012**, 1-17 (2012).

50. K. Chen, X. Zhou, W. Peng, and Q. Yu, "OFDR based distributed temperature sensor using the three-channel simultaneous radio-frequency lock-in technique," Photonic Sensors **5**, 217-223 (2015).

51. U. Glombitza and E. Brinkmeyer, "Coherent frequency-domain reflectometry for characterization of single-mode integrated-optical waveguides," Journal of Lightwave Technology **11**, 1377-1384 (1993).

52. G. E. Jabbour, E. Karamehmedovic, U. Glombitza, and J. T. Rantala, "Fiber optic distributed temperature sensor using incoherent optical frequency domain reflectometry," Proceedings of SPIE **5363**, 107-115 (2004).

53. H. Ghafoori-Shiraz and T. Okoshi, "Fault location in optical fibers using optical frequency domain reflectometry," Journal of Lightwave Technology **4**, 316-322 (1986).

54. B. E. Saleh, M. C. Teich, and B. E. Saleh, *Fundamentals of photonics* (Wiley New York, 1991), Vol. 22.

55. Y. Cheng, C. Hill, B. Liu, Z. Yu, H. Xuan, D. Homa, A. Wang, and G. Pickrell, "Modal reduction in single crystal sapphire optical fiber," Optical Engineering **54**, 107103 (2015).
56. Y. Cheng, C. Hill, B. Liu, Z. Yu, H. Xuan, D. Homa, A. Wang, and G. Pickrell, "Design and analysis of large-core single-mode windmill single crystal sapphire optical fiber," Optical Engineering **55**, 066101 (2016).
57. C. Hill, D. Homa, B. Liu, Z. Yu, A. Wang, and G. Pickrell, "Submicron diameter single crystal sapphire optical fiber," Materials Letters **138**, 71-73 (2015).
58. R. G. Smith, "Optical Power Handling Capacity of Low Loss Optical Fibers as Determined by Stimulated Raman and Brillouin Scattering," Applied Optics **11**, 2489-2494 (1972).
59. R. W. Boyd, "Nonlinear Optics," 474 (2007).
60. R. H. Stolen, C. Lee, and R. K. Jain, "Development of the stimulated Raman spectrum in single-mode silica fibers," Journal of the Optical Society of America B **1**, 652 (1984).
61. M. Planck, *The theory of heat radiation* (P. Blakiston's Son & Co, 1914).
62. M. Yashima, M. Kakihana, R. Shimidzu, H. Fujimori, and M. Yoshimura, "Ultraviolet 363.8-nm Raman spectroscopic system for in situ measurements at high temperatures," Applied Spectroscopy **51**, 1224-1228 (1997).
63. E. Zouboulis, D. Renusch, and M. Grimsditch, "Advantages of ultraviolet Raman scattering for high temperature investigations," Applied Physics Letters **72**, 1-3 (1998).
64. H. Fujimori, M. Kakihana, K. Ioku, S. Goto, and M. Yoshimura, "Advantage of anti-Stokes Raman scattering for high-temperature measurements," Applied Physics Letters **79**, 937-939 (2001).
65. R. S. Krishnan, "The scattering of light in diamond and its Raman spectrum," Proceedings of the Indian Academy of Sciences, Section A **26**, 399-418 (1947).
66. Q. Ma and D. R. Clarke, "Optical Fluorescence from Chromium Ions in Sapphire - a Probe of the Image Stress," Acta Metall Mater **41**, 1811-1816 (1993).
67. C. Zuo, "Part II. Luminescence in the Raman spectra of aluminum oxide," Doctoral dissertation (West Virginia University, Morgantown, W. Va, 2002).
68. R. K. Nubling and J. A. Harrington, "Optical properties of single-crystal sapphire fibers," Appl Opt **36**, 5934-5940 (1997).
69. A. Wang, Y. Shen, L. Tong, and S. Chen, "Performance stability of the sapphire fiber and cladding under high temperature," **3852**, 134-142 (1999).

70. W. Spratt, M. Huang, T. Murray, and H. Xia, "Optical mode confinement and selection in single-crystal sapphire fibers by formation of nanometer scale cavities with hydrogen ion implantation," Journal of Applied Physics **114**, 203501 (2013).
71. Y. Zhu, "Miniature Fiber-Optic Sensors for High-Temperature Harsh Environments," Ph.D. (Virginia Tech, 2007).
72. Y. Li, C. R. Liao, D. N. Wang, T. Sun, and K. T. V. Grattan, "Study of spectral and annealing properties of fiber Bragg gratings written in H_2-free and H_2- loaded fibers by use of femtosecond laser pulses," Optics Express **16**, 21239 (2008).
73. C. Raml, X. He, M. Han, D. R. Alexander, and Y. Lu, "Raman spectroscopy based on a single-crystal sapphire fiber," Opt Lett **36**, 1287-1289 (2011).
74. A. Schauer, "Thermal expansion, grueneisen parameter, and temperature dependence of lattice vibration frequencies of aluminum oxide," Canadian Journal of Physics **63**, 523-531 (1964).
75. P. G. Klemens, "Anharmonic Decay of Optical Phonons," Physical Review **148**, 845-848 (1966).
76. F. L. Galeener, J. C. M. Jr., R. H. Geils, and W. J. Mosby, "The relative Raman cross sections of vitreous SiO2, GeO2, B2O3, and P2O5," Applied Physics Letters **32**, 34-36 (1978).